A Study of the Thermodynamics and Kinetics of Li_xFePO_4 as a Cathode Material for Li Batteries

Thesis by

Hongjin Tan

In Partial Fulfillment of the Requirements

for the Degree of

Doctor of Philosophy

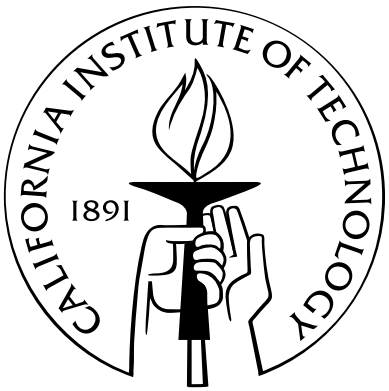

California Institute of Technology

Pasadena, California

2012

(Defended November 4, 2011)

To my parents, for their love and support through all these years ...

Acknowledgements

I would like to acknowledge a number of people for their support throughout my Ph.D. studies. First of all, I would like to thank my advisor, Dr. Brent Fultz, who constantly advised, motivated, and enlightened me during my time at Caltech. His enthusiasm for seeking the truth in science and his creative and critical thinking will have a lifelong influence on me.

I learned a lot from the research scientists in our group, Dr. Channing Ahn and Dr. Jiao Lin, during my work at Caltech. They are knowledgeable and helpful, and guided me through important steps in my research. I am grateful for my practical electrochemistry education from the postdoctoral fellows Dr. Qingfang Shi, Dr. Cedric Weiss, Dr. Isabelle Darolles, and Dr. Delphine Borivent in the electrochemical lab. I want to thank Dr. Chi Ma and Carol Garland for their assistance with the electron microscope work, and Mike Vondrus for the machinery work.

I enjoyed working together with the previous and current graduate students in Dr. Fultz' group: Dr. Joanna Dodd Cardema, Dr. Olivier Delaire, Dr. Max Kresch, Dr. Matt Lucas, Dr. Mike Winterrose, Dr. Justin Purewal, Chen Li, Jorge Munoz, Lisa Mauger, David Abrecht, Nick Stadie, Hillary Smith, Tian Lan, and Sally Tracy, and the undergraduate student Laura Kim. They not only gave me a lot of help in my research, but also brought me many good times during my graduate studies. I also enjoyed spending my spare time with my friends and roommates: Ryan Briggs, Allen Wong, Erlend Weydahl, Kunwoo Kim, Shuo Han, Yuan Zhong, Yizhou Liu, Molei Tao, Chengshan Zhou, Ting Hong, Maolin Ci, and many more. I would give special thanks to Iris Yijia Luo. They all left me with many good memories during my five years in Pasadena.

My research projects could not have been completed without the many collaborators I have worked with. I would like to give my gratitude to Dr. Khalil Amine and Dr. Ilias Belharouak from Argonne National Lab, Dr. Simon Jones and Dr. Joe McMenamin from Contour Energy System, Dr. Steven Kaye and Dr. Mark Bailey from Wildcat Discovery Technology, Dr. Ratnakumar Bugga and Dr. Abhijit Shevade from Jet Propulsion Lab, and Dr. Scott Jorgensen from General Motors. Many times I learned a lot from insightful conversations with them.

I would like to acknowledge General Motors for their financial support for my Ph.D. research.

Finally, I would like to thank my family — my grandfather and grandmother, my uncles and aunts, my cousins, and especially my parents — for their love and support through all these years of

my education. My thesis would not have been possible without their encouragement and support.

Abstract

Olivine-type $LiFePO_4$ has been recognized as one of the most promising cathode materials for rechargeable Li batteries. Its advantages include high capacity, high stability, nontoxicity, and low cost. Our methods for synthesizing nanocrystalline Li_xFePO_4 with the olivine structure are described. Solid-state reactions and precipitation reactions were both successful, and ball milling was especially effective at reducing crystallite sizes. Diffractometry and microscopy were used to characterize these materials, and results of impurity phases, excess Fe^{3+}, and internal stresses are reported for the different types of synthesis.

Applications of lithium-ion batteries, including automotive applications, require fast kinetics and high conductivity of ions and electrons. Unfortunately, Li_xFePO_4 has the electronic structure of an insulator, an entirely unsatisfactory situation if it is to be used as a battery electrode. Electrical conductivity in Li_xFePO_4 occurs by the motion of small polarons, which are valence electrons at Fe atoms plus their distorted local environments. Electrical conductivity of Li_xFePO_4 is interpreted in terms of small polaron hopping. There are other factors of importance in these measurements, such as impurities or defects that block the one-dimensional conduction channels of the olivine structure of Li_xFePO_4.

We studied the polaron hopping directly, which allows us to understand the intrinsic electrical conductivity, and how it depends on microstructure and composition of Li_xFePO_4. The experimental technique was Mössbauer spectrometry, which has been used for many years as a means for determining the fractions of Fe^{2+} and Fe^{3+} in a material. Usually the spectral signatures of Fe^{2+} and Fe^{3+} are distinct. When valence electrons hop between Fe^{2+} and Fe^{3+} at a frequency of 10^8 Hz or higher, however, the valence changes during the timescale of the Mössbauer measurement and the spectrum is blurred. By measuring Mössbauer spectra at elevated temperatures, we can determine the fractions of Fe atoms participating in polaron hopping, and determine the activation energy of the process. From this we estimate intrinsic electrical conductivities of 10^{-7}S/cm at room temperature for nanocrystalline $Li_{0.5}FePO_4$, for example. We find a comparable conductivity for Li_xFePO_4 prepared as a solid solution, but the conductivity of conventional Li_xFePO_4 is much lower.

There has been much discussion about how surface area might thermodynamically stabilize the solid solution phase of nanocrystalline Li_xFePO_4. In a series of X-ray diffraction measurements, some

at elevated temperatures, we found the solid solution phase of Li_xFePO_4 to be especially robust at room temperature when the material was prepared in nanocrystalline form. Moreover, the consistent phase transition temperature around 200°C was observed, as evidence for the unchanged equilibrium phase diagram by crystallite size. This is consistent with our evaluation on the boundaries of the two-phase mixture of triphylite and heterosite during Li insertion and extraction. Profiles of entropy and enthalpy changes were evaluated by open-circuit voltage measurements. The boundaries were found at x=0.05 and 0.95 in the Li_xFePO_4 with crystal size of 70 nm, similar to the reported values on bulk-Li_xFePO_4. These are important in practice, because electrochemical lithiation and delithiation at room temperature should remain as a two-phase transformation, even if a solid solution of lithium is present in the initial electrode material.

Contents

List of Figures

List of Tables

Chapter 1

Materials for Rechargeable Lithium Batteries

1.1 Overview

A large amount of fossil fuel is consumed every day to generate electricity and power combustion engines, causing global concern about energy efficiency, greenhouse gas emission, and depletion of natural resources. Consequently, substantial effort has been made to develop renewable energy technology such as solar panels, fuel cells, and electrically powered vehicles. These all require methods for electrical energy storage. Batteries, as devices for storing energy chemically, possess advantages of high portability, high conversion efficiency, long life, and zero exhaust release. They are ideal power sources for portable devices, automobiles, and backup power supplies. Therefore, developing battery technology, particularly rechargeable batteries, has become a key issue for science and industry.

Among the many types of rechargeable batteries, Li-ion batteries have high volumetric and the highest gravimetric energy density, due to its smallest atomic weight of 6.94 g/mol among all metallic elements (despite smallest density of 0.53 g/cm^3). They can meet many requirements for products such as electric vehicles and portable electronic devices. Notably, Li^+/Li has a very negative standard reduction potential of -3.05 V versus a standard hydrogen electrode (SHE).

A Li-ion battery consists of several electrochemical cells connected in parallel and/or in series to provide a designated capacity or voltage [6]. Each electrochemical cell has two electrodes, the cathode and anode, separated by an electrolyte that is electrically insulating but conductive for Li^+ ions. During discharging, when a Li-ion battery works as a galvanic cell, Li^+ ions flow internally from the negative electrode (anode) to the positive electrode (cathode), while electrons move externally from the negative electrode to the positive electrode. During charging, or when it works as an electrolytic cell, Li^+ ions flow internally from the positive electrode to the negative electrode, while electrons move externally from the positive electrode to the negative electrode to maintain charge

neutrality.

1.2 Cell thermodynamics

1.2.1 Thermodynamic parameters in cells

Assuming the cell is in thermodynamic equilibrium, including zero charge exchange, the open-circuit voltage (OCV) $V\,(i = 0)$ can be measured. It does not depend on the direction of reaction [7]. According to the first and second laws of thermodynamics, the system has energy

$$\Delta E = \Delta Q + W = T\Delta S - P\Delta V + W_e \ , \tag{1.1}$$

where T, S, P, V are temperature, entropy, pressure, and volume of the system, respectively, and W_e is the electrical work that the cell can provide. Equation 1.1 yields

$$W_e = \Delta E - T\Delta S + P\Delta V = \Delta G \ . \tag{1.2}$$

The Gibbs free energy ΔG represents the maximum amount of work, and can be extracted from an open-circuit measurement of potential V,

$$\Delta G = W_{max} = -nFV \ , \tag{1.3}$$

where $n = 1$ for $\mathrm{Li}^+/\mathrm{Li}$ pair, and F is the Faraday constant of a mole of charge. $F = eN_A = 96485\,C$ (or $26.8\,\mathrm{Ah}$), where N_A is the Avogadro constant. From Eq. 1.3, the chemical potential change μ can be obtained

$$\mu = \frac{\partial G}{\partial n}|_T = -eV \ . \tag{1.4}$$

Assuming $dP = 0$, and replacing molar fraction by composition $x = n/N_A$, it gives

$$dG = -FVdx - SdT \ . \tag{1.5}$$

With Maxwell relations, this yields

$$\frac{\partial S}{\partial x}|_T = F\frac{\partial V}{\partial T}|_x, \tag{1.6}$$

and

$$\frac{\partial H}{\partial x}|_T = -FV + T\frac{\partial S}{\partial x}|_T = -FV + TF\frac{\partial V}{\partial T}|_x. \tag{1.7}$$

Equations 1.6 and 1.7 relate basic thermodynamic functions to electrochemical parameters. For example, a change of the entropy difference between the two electrodes with Li^+ concentration is

proportional to the change of how the open-circuit voltage depends on temperature at a fixed state of charge.

1.2.2 Gibbs phase rule in cells

The Gibbs phase rule of thermodynamics can be applied to battery cells, provided the system is under thermodynamic equilibrium. The number of degrees of freedom f is given by

$$f = c - p + 2 \,, \tag{1.8}$$

where c is the number of components and p is the number of coexisting phases. Most often, the lithium intercalation in the electrode is a two-component system ($c = 2$), the Li^+ ions and the host structure. Therefore, if giving a single phase ($p = 1$), besides temperature (T) and pressure (P), there is only one more degree of freedom ($f = 3$). Thus the chemical potential μ (or OCV) has to be a function of T, P, and composition x. In the case of a two-phase mixture, there is no more independent degree of freedom besides T and P ($f = 2$), so all thermodynamic functions such as μ, S, or H should remain constant with composition x under a fixed T and P.

1.3 Cell kinetics

1.3.1 Arrhenius relation

It was Arrhenius who first found that general reaction kinetics have exponential dependence on $1/T$, and proposed the form

$$k = k_0 \exp(-Q_A/k_B T) \,, \tag{1.9}$$

where Q_A is usually called the activation energy, or standard internal energy of activation. It only has a difference of ΔPV compared to the standard enthalpy of activation, ΔH (i.e., they become the same when ΔPV is ignored). k_0 is the attempt frequency factor. This prefactor can also be included in the product $k_0' \exp \Delta S/k_B$, which involves the standard entropy of activation, ΔS. Thus the Arrhenius equation (Eq. 1.9) can be recast as

$$k = k_0' \exp(-\Delta G/k_B T) \,, \tag{1.10}$$

where ΔG is the standard Gibbs free energy of activation [8]. Equation 1.10 is an equivalent statement of Eq. 1.9, an empirical interpretation of reaction kinetics.

1.3.2 Nernst equation and Tafel equation on electrodes

For an electrode reaction, equilibrium is described by the Nernst equation,

$$E = E_0 + \frac{RT}{nF} \ln \frac{C_o}{C_r} \,, \tag{1.11}$$

where C_o and C_r are bulk concentrations of the cathodic and anodic components in the electrode. This equation says that if all steps have facile kinetics and are chemically reversible, the electrode potential and the surface concentrations of the initial reactant and final product are in local Nernstian balance at all times, regardless of the current flow [8]. Many systems satisfy these conditions.

The dependence of current on potential is often complicated. As for overpotential, one empirical relation is known as Tafel equation:

$$\eta = a + b \log i \,, \tag{1.12}$$

where η is the overpotential, difference between the actual potential and thermodynamically determined reduction potential.

1.3.3 Marcus theory of electron transfer

The field of electron transfer has been developed quickly since the 1940s. Compared to many other chemical reactions, the electron transfer process happens fast, without breaking and forming chemical bonds. The earliest experimental observations were explained by the Franck-Condon principle, which is used widely to interpret excitation spectra of vibronic quantum states. According to this principle, the nuclear coordinates must fluctuate into a suitable configuration from the reactant to the product. Marcus proposed that the potential energy curves for the reactant and the product intersect, and with the electronic coupling, charge transfer happens in a radiationless, or isoenergetic way.

Let q be the reaction coordinate. The free energies of the reactant R and product P depend quadratically on the reaction coordinate:

$$G_R(q) = (k/2)(q - q_R)^2 \,, \tag{1.13}$$

$$G_P(q) = (k/2)(q - q_P)^2 + \Delta G \,, \tag{1.14}$$

where q_R and q_P are the coordinates for the reactant and product in equilibrium, and k is a proportionality constant (e.g., a force constant for changing the bond length). ΔG is the free energy difference between R and P under their equilibrium conditions.

According to the Franck-Condon principle, charge transfer only occurs at the intersection of free energy curves of R and P, where the nuclear coordinate becomes q^*. The free energies at the

transition state are

$$G_R(q^*) = (k/2)(q^* - q_R)^2 \ , \tag{1.15}$$

$$G_P(q^*) = (k/2)(q^* - q_P)^2 + \Delta G \ . \tag{1.16}$$

Since $G_R(q^*) = G_P(q^*)$, q^* can be solved

$$q^* = (q_R + q_P)/2 + \Delta G/k(q_P - q_R) \ , \tag{1.17}$$

the free energy of activation for the reaction from R to P relative to $G_R(q_R)$ is given by

$$\Delta G_r^* = G_R(q^*) = \frac{\lambda}{4}(1 + \frac{\Delta G}{\lambda})^2 \ , \tag{1.18}$$

where $\lambda = (k/2)(q_P - q_R)^2$ is the critical parameter called the reorganization energy, representing the energy needed to transfer the nuclear configurations in the reactant to those of the product state.

1.3.4 Fick's laws

Mass transfer to an electrode is governed by the Nernst-Planck equation, in addition to Fick's first law of diffusion,

$$J_i(x) = -D_i\frac{\partial C_i(x)}{\partial x} - \frac{z_i F}{RT}D_i C_i\frac{\partial \phi(x)}{\partial x} + C_i v(x) \ , \tag{1.19}$$

where $J_i(x)$ and $C_i(x)$ are the flux ($\mathrm{mol{\cdot}s^{-1}{\cdot}cm^{-2}}$) and concentration of species i at distance x from the surface, D_i is the diffusion coefficient ($\mathrm{cm^2/s}$), $\partial C_i(x)/\partial x$ is the concentration gradient at x, and $\partial\phi(x)/\partial x$ is the potential gradient. The three terms represent contributions to the flux from diffusion, migration, and convection, respectively [9]. The Einstein relation is derived from Fick's first law, when only diffusion is considered,

$$D = \frac{uRT}{zF} \ , \tag{1.20}$$

where u is the ionic mobility, z is the number of charges per unit, and F is the Faraday constant. The Einstein relation connects the diffusion coefficient D and ionic mobility u. Since molar conductivity $\sigma = z \cdot u \cdot F$, from Eq. 1.20, we have

$$\sigma = \frac{Dz^2F^2}{RT} \ , \tag{1.21}$$

as the general expression for conductivity. In the case of a strong electrolyte, the conductivity σ is the sum of contributions of cations and anions,

$$\sigma = \mu_+\sigma_+ + \mu_-\sigma_- \ , \tag{1.22}$$

where μ_+ and μ_- are the number of cations and anions.

For time-dependent diffusion processes, Fick's second law gives

$$\frac{\partial C_i(x)}{\partial t} = D_i \frac{\partial^2 C_i(x)}{\partial x^2} \ . \tag{1.23}$$

1.4 Electrode materials for rechargeable Li batteries

For a secondary battery, not only the redox reactions on both cathode and anode need to be reversible, but also the lithiation and delithiation occurring in the two electrode materials have to be practically reversible. Selecting materials for the two electrodes is largely based on the reversibility concern, as well as thermodynamic stability and electronic/ionic kinetics.

1.4.1 Anode

The earliest rechargeable Li batteries used lithium metal as the anode [10]. However, a passivating layer was found to grow after repeated working cycles of charge and discharge, and the metal surface became uneven. This dendrite problem makes a battery age quickly and even explode if the dendrite makes a short circuit between the electrodes. Li-Al alloys improved safety, but still could not prevent the quick capacity fade [11].

To date, carbon-based materials are the most common negative electrodes used in Li-ion batteries. Graphite was found to be able to host Li in a stable phase with a stoichiometry of LiC_6 [12]. The graphite anode was commercialized by Sony in 1991 [13]. The graphite anode has a theoretical capacity of 372 mAh/g, and only 0.1 V difference from a Li^+/Li electrode. Replacing lithium metal with graphite not only solves the dendrite problem but also lowers the cost. Recently, in order to improve the lithium diffusion coefficient in carbon, graphene nanospheres and graphene oxide nanosheets were designed with a higher surface-to-volume ratio [14, 15]. The exotic electronic mobility and mechanical properties of graphene are expected to help with the battery performance, but have not been verified yet.

To push the limit of energy density and capacity in carbon-base materials, other anode candidates are also being studied, including metals, alloys, and oxides. For example, the spinel $Li_4Ti_5O_{12}$ is being investigated for high-power applications. Since its charging potential is 1.55 V higher than Li^+/Li, it has no risk of lithium deposition and is safe for fast cycling with a high current. Besides the candidates for lithium insertion, there are also conversion-type materials that involve more complicated chemical reactions than Li intercalation into the host structure, including the silicon nanowires [16, 17], silicon and germanium nanocrystallites [18, 19], SnO_2 on carbon nanosheets [20, 21], and TiO_2 on graphene substrate [22]. All show good rate capability as anodes for lithium storage, perhaps because of the short diffusion distances needed for Li insertion into nanostructures.

1.4.2 Cathode

1.4.2.1 Hexagonal TiS_2

As the earliest cathode for lithium ion cells, TiS_2 has a layered hexagonal structure with open octahedral sites for reversible Li insertion. It was first proposed by Exxon in 1972 [10]. This material forms a single phase with lithium concentration over the entire range of Li_xTiS_2 for $0 \leq x \leq 1$ [23].

1.4.2.2 Olivine $LiMPO_4$

Since then, three major categories of insertion-type cathodes have been developed. The latest category is the lithium polyanionic salt. Among them, lithium metal phosphate, $LiMPO_4$ (M = Fe, Mn, Co, Ni), with the olivine-type structure, is the best known. The open-circuit voltages are 3.5 V for $LiFePO_4$, 4.1 V for $LiMnPO_4$, 4.8 V for $LiCoPO_4$, and 5.1 V for $LiNiPO_4$. Even though other transition metal phosphates have higher potentials than $LiFePO_4$, none showed superior electrochemical reversibility compared to $LiFePO_4$. Detailed information on $LiFePO_4$ and the olivine structure are given in the following chapters.

Other classes of polyanion-based cathode candidates include $LiMPO_4F$ [24, 25, 26] and Li_2MSiO_4 (M=Fe, V, or Co) [27]. The lithium iron fluorophosphate ($LiFePO_4F$) has the same triclinic crystal structure as tavorite $LiFePO_4OH$, in which every two Fe-centered octahedra (FeO_4F_2) share a F atom, and every Fe-centered octahedron shares four O atoms with four PO_4 tetrahedra around it. Li, in this structure, diffuses in three dimensions instead of in a one-dimensional channel, as in $LiFePO_4$. $LiFePO_4F$ can be synthesized from milling FeF_3 and Li_3PO_4, or by an "ionotherma" reaction of mixing the same precursors in ionic liquids at controlled temperature [28]. $LiFePO_4F$ showed an electrochemical transition to Li_2FePO_4F, giving a capacity close to the theoretical 152 mAh/g. The crystal strain created by lithium intercalation is found to be smaller than $LiFePO_4$.

The Li_2FeSiO_4 was reported to be reversible, with a capacity of 140 mAh/g and about 3.0 V discharge voltage [29]. Unlike the olivine phosphates, Li_2FeSiO_4 crystals consist of FeO_4 and SiO_4 tetrahedra. The measured electrical conductivity is however 1000 times smaller than that of $LiFePO_4$ [30].

1.4.2.3 Hexagonal $LiMO_2$

The category of cathode materials that has received the most extensive study is the lithium metal oxides, $LiMO_2$ (M = Co, Mn, Ni, Al). Following the discovery of $LiCoO_2$ in 1980 [31], its successful commercialization brought tremendous attention to this class of material. Similar to TiS_2, Li_xCoO_2 has the hexagonal layered structure (O3) for $0.75 \geq x \geq 0.5$, where Li can be hosted between CoO_2 octahedra planes. At $x \approx 0.75$, a change of electrical conductivity was observed, and vacancies are believed to disorder. Below $x \approx 0.55$, the structure changes irreversibly to a monoclinic phase

[32, 33, 34]. If all Li can be extracted, Li_xCoO_2 has a theoretical capacity of 274 mAh/g. However, only about half of the capacity is reversible in a practical sense.

$LiNiO_2$ is difficult to synthesize with controlled stoichiometry, and usually ends up with $Li_{1-y}Ni_{1+y}O_2$ [35]. Moreover, Ni^{3+} is unstable with oxygen, causing occupation of excessive Ni ions on Li sites and a high oxygen partial pressure. These give $LiNiO_2$ the disadvantages of low lithium kinetics and poor safety.

$LiMnO_2$ is more environmentally friendly and economical than $LiCoO_2$. But unlike CoO_2, the hexagonal crystal structure of MnO_2 is impossible to form by conventional solid-state reaction, and the orthorhombic structure is found to be more thermodynamically stable [36]. $LiMnO_2$ is often obtained from exchanging Li ions with stable $NaMnO_2$. The metastable $Li_{0.5}MnO_2$ often evolves into a more stable spinel structure [37].

Binary and ternary systems with mixed transition metals showed appealing rate capability and stability. Typical examples include $LiCo_{1/3}Ni_{1/3}Mn_{1/3}O_2$ [38] and $LiNi_{0.5}Mn_{0.5}O_2$ [39]. Reversible capacities of these mixed-metal compounds were reported to be 200 mAh/g over a potential range of 2.5 to 4.5 V vs. Li^+/Li. Much less capacity fade was observed compared to $LiCoO_2$ [40].

Recently, various coating processes were used for improving electrochemical performance of the lithium metal oxides. This includes coatings of $AlPO_4$, SiO_2, and Al_2O_3 nanoparticles on the $LiMO_2$ to increase cycle life and reduce capacity fade [41, 42, 43]. The reason for such improvement is unclear however. They may decrease the crystal microstrain of $LiMO_2$, or suppress the exothermic reaction between the electrolyte and the electrode. The coating of Li_2MnO_3 was found to successfully stabilize $LiMO_2$ cathodes, as the layered $xLi_xMnO_3+(1-x)LiMO_2$ forms to help achieve a high capacity ($>$ 200 mAh/g) and high working voltage (3.0V – 4.5V) [44].

1.4.2.4 Spinel $LiMn_2O_4$

An alternative to $LiMnO_2$ is the spinel $LiMn_2O_4$ originally proposed in 1983 [45]. When the Li ions move out, it becomes MnO_2 when charged as the cathode. The Mn^{4+}/Mn^{3+} ions with a potential of 4.1 V vs. Li^+/Li provide high stability and power capability. The correlation between its cubic lattice parameter and lithium concentration was investigated [46]. The biggest problem of these spinel cathodes is their capacity fade during cycling, especially at elevated temperatures with the electrolyte of $LiPF_6$. Dissolution of Mn into the electrolyte is generally considered the main cause. Recently, electrolyte additives, fluorine substitution, and oxide coating were found to largely reduce Mn dissolution [47].

1.4.2.5 Li-S and Li-O_2

For electric vehicle applications, Li-S and Li-air batteries have received much attention. Unlike the major three categories of cathode materials that store charge by Li^+ insertion (or extraction) in

the host structure, at the Li-S electrode the sulfur continues being reduced by increasing lithium stoichiometry in the form of "polysulfide" Li_2S_n molecules (n from 8 to 1) [48, 49]. The Li-S electrode can reach a capacity as high as 1675 mAh/g, although this is at only 2.1 V vs. Li^+/Li. Unfortunately, this electrode has very poor electrical conductivity both in the form of sulfur and Li_2S_n. There is also a large hysteresis between charge and discharge, and the capacity fades rapidly. Moreover, the electrode material lithium polysulfide was found dissolved in the electrolyte. Carbon coating was reported to help greatly with those deficiencies [50]. Recently, sulfur was coated onto graphene nanosheets, and found to improve cell cycle life and capacity [51].

Similar to the Li-S electrode, a Li-air electrode uses O_2 to oxidize Li, forming Li_2O_2 on the cathode and giving 3.0 V relative to Li^+/Li [52]. Reversibility of O_2 reduction was realized by using a nonaqueous electrolyte [53], but similar to the O_2 cathode in fuel cells, a good catalyst is required for oxidizing Li_2O_2, and this catalyst remains a challenge. Moreover, the system suffers a voltage polarization of 1.5 V in its cycling curve.

1.4.2.6 Rhombohedral FeF_3

FeF_3, which crystalizes into the ReO_3 rhombohedral structure, is the fluoride cathode that has attracted the most attention by far [54]. An early study showed an initial discharge capacity of 140 mAh/g followed by about 80 mAh/g upon cycling [55]. The discharge voltage was at 3.0 V, 0.4 V lower than the reduction potential of $FeF_3/LiFeF_2$. Later work showed that carbon coating by ball-milling FeF_3 with graphite or carbon nanotubes gave an an increased capacity of 600 mAh/g [56, 57]. This indicates further reduction beyond $Fe^{3+} \rightarrow Fe^{2+}$ at FeF_3. The reaction mechanism was then investigated by NMR and XRD studies, which found a change from ReO_3 structure to the rutile structure during discharge, but many details remained ambiguous [58].

Several other iron compounds were studied over the years, such as $KFeS_2$, FeS_2, $FePS_3$, FeOCl, but none showed good reversibility.

Chapter 2

Mössbauer Spectrometry

2.1 General theory of the Mössbauer effect

2.1.1 Resonant scattering

In 1958, Rudolf Mössbauer first observed nuclear resonant scattering in solid Iridium-191 during his doctoral research. He correctly proposed this as recoilless photon emission and absorption by nucleus when atoms are bound in a solid crystal lattice. He won the Nobel prize in physics three years later for the discovery of this "Mössbauer effect".

The half-life time of the 14.4 keV level of ^{57}Fe is 97.7 ns. This gives its absorption spectrum a linewidth of 4.67×10^{-9} eV from the uncertainty principle relation:

$$\Delta E = h/\Delta t \ , \tag{2.1}$$

where $h = \hbar/2\pi$ is the Planck constant and Δt represents the lifetime of excited nuclear state.

The nuclear recoil energy can be estimated simply from classical mechanics. Emitting a photon with energy E_p, an atom decays from its excited state E_{ex} to ground state E_g, and the laws of momentum and energy conservation give:

$$Mv_f + \frac{E_p}{c} = Mv_i \ , \tag{2.2}$$

and

$$E_g + \frac{1}{2}Mv_f^2 + E_p = E_{ex} + \frac{1}{2}Mv_i^2 \ , \tag{2.3}$$

where M is the atomic mass, and v_i and v_f are initial and final velocities of the atom in motion. From Eq. 2.2, the recoil energy E_r can be obtained:

$$E_r = \frac{1}{2}M(v_f - v_i)^2 = \frac{E_p^2}{2Mc^2} \ , \tag{2.4}$$

which is 0.002 eV for ^{57}Fe. From Eq. 2.3, we have:

$$E_{ex} - E_g - E_p = \frac{1}{2}M(v_f^2 - v_i^2) = \frac{1}{2}M(v_f - v_i)(v_f - v_i + 2v_i) = \frac{E_p^2}{2Mc^2} - \frac{v_i}{c}E_p \ . \tag{2.5}$$

To realize resonant emission (and absorption, with similar expressions to emission), the energy difference between the nuclear excited state and the ground state should be accurate to be within $\sim 10^{-8}$ eV (from Eq. 2.1) the same as the photon energy. The left-hand side of Eq. 2.5 should go to zero within the quantum uncertainty of 10^{-8} eV. One would try to compensate the recoil energy with a Doppler energy shift, $\frac{v_i}{c}E_p$. For ^{57}Fe with excitation energy of 14.4 KeV and recoil energy of 0.002 eV, v_i needs to be 41.7 m/s. This may not be too difficult to achieve, but the large energy uncertainty caused by Doppler broadening could also deteriorate nuclear resonance, since its natural linewidth only has a magnitude of 10^{-8} eV. Rudolf Mössbauer was the first to realize that the first term of Eq. 2.5 on the right-hand side could go to zero when M is infinitely large (i.e., the nucleus is bound in a crystal).

Lattice vibrations are essential for understanding recoilless γ-ray scattering. In 1907, Einstein first explained the decrease of the specific heat in solid crystals by assuming the crystal consists of atomic harmonic oscillators with vibrating frequency ω_E. Debye improved the theory by introducing a continuum of oscillator frequencies with a distribution function $c(\omega)$. The lineshape in Mössbauer spectrometry and the recoilless fraction can be deduced from an oscillator model, as described in the next section. This vibrational excitations in solids are "phonon". Technically, a resonant scattering that involves phonon creation or annihilation is inelastic, and is not the Mössbauer effect. However, synchrotron radiation is able to tune the incident photon energy below and above the nuclear resonance by 100 meV, a typical range of phonon energies. This technique can thus measure the partial phonon density of states (DOS) of the Mössbauer nucleus in the lattice [59, 60, 61].

2.1.2 Mössbauer spectrum

In a laboratory Mössbauer spectrometer, photons are emitted from a radioactive source. The incident photon energy is modulated linearly by a mechanical Doppler shift, with constant acceleration or deceleration in both directions:

$$E_v = \frac{v}{c}E_\gamma \ . \tag{2.6}$$

Thus a Mössbauer spectrum is constructed by consecutively recording transmitted signals (attenuating photons that are resonantly absorbed) as the photon energy is modulated. The spectrum is usually scaled and plotted by velocities corresponding to the Doppler shift energies. The lineshape in a Mössbauer spectrum can often be described as a Lorentzian or relativistic Breit-Wigner

distribution:

$$I_E = I_0 + \frac{A}{(E - E_0)^2 + B} \ . \tag{2.7}$$

This lineshape is similar to the solution of motion for a classical damped harmonic oscillator. It can also be easily understood in the example of a decaying radiating electromagnetic wave with a lifetime τ and a vector potential $\overrightarrow{A}_E$

$$\overrightarrow{A}_t = \overrightarrow{A}_0 \exp(-t/\tau) \exp(-iE_0 t/h) \ . \tag{2.8}$$

Its Fourier transform yields

$$\overrightarrow{A}_E = \frac{\overrightarrow{A}_0}{\sqrt{2\pi}} \int dt \exp(-t/\tau) \exp(-iE_0 t/h) \exp(iEt/h) = \frac{\overrightarrow{A}_0}{\sqrt{2\pi}} \frac{1}{\Gamma - i(E - E_0)} \ . \tag{2.9}$$

Therefore, the intensity distribution is given by

$$I_E = \frac{I_0}{2\pi} \frac{1}{(E - E_0)^2 + \Gamma^2} \ . \tag{2.10}$$

This becomes Eq. 2.7 and explains the parameters in Eq. 2.7 above. The recoilless fraction of the scattering is important, and is known as the Lamb-Mössbauer factor

$$f = < \exp(-i \overrightarrow{k} \cdot \overrightarrow{x}) > = \exp(-k^2 x^2) \ , \tag{2.11}$$

where $\overrightarrow{k}$ is the wave vector of the photon, and $\overrightarrow{x}$ is the vector of atomic displacement. The average of $\overrightarrow{k} \cdot \overrightarrow{x}$ should be taken over the nuclear lifetime. Equation 2.11 is similar to the Debye-Waller factor in X-ray and neutron scattering. At $\sim 0\,\mathrm{K}$ when there is no thermal vibration of lattice, f goes close to 1. At finite temperatures, f decreases with increasing temperature.

2.1.3 Hyperfine interactions

The positively charged nucleus and the negatively charged electrons are bound strongly by the Coulomb force. Besides that, there are more complicated "subtle" interactions between the nucleus and electrons, often referred to as "hyperfine" interactions, an analogy of the fine structure observed among electrons. The three important hyperfine parameters in the regime of Mössbauer spectrometry, isomer shift, electric quadrupole splitting, and magnetic dipole splitting, are reviewed here.

2.1.3.1 Isomer shift

Isomer shift E_{IS} is a correction of electron density at the nucleus. Energy levels are slightly shifted when a point-charged nucleus is considered as a "finite-sized" sphere. Coulomb potential of the nucleus thus is changed from $V(r) = -\frac{Ze^2}{r}$ to $V(r < R) = \frac{Ze^2}{R}(-\frac{3}{2} + \frac{r^2}{2R^2})$. In Mössbauer spectrometry, this results in a shift in the absorption line which is proportional to the difference of transition energies between the source S and absorber A, given by

$$E_{IS} = \frac{c}{E_p}[(E_{ex}^A - E_g^A) - (E_{ex}^S - E_g^S)] = \frac{4\pi cZe^2}{5E_p} r\Delta r(\sum |\psi_A^2(0)| - |\psi_S^2(0)|) \ , \tag{2.12}$$

where $|\psi^2(0)|$ is the relative electron density at the nucleus ($r = 0$). The electrostatic interaction at $r = 0$ is determined by integration of product of the nuclear charge density and the electron charge density. Wave function of s electrons is radially isotropic, thus gives large overlap for its interaction with the nuclear charge. On the other hand, p electrons and d electrons do not concentrate at $r = 0$, so their contributions to isomer shift are relatively smaller.

The relative isomer shift of ^{57}Fe versus ^{57}Co/Rh is -0.1 mm/s, and a Mössbauer spectrum is usually plotted with reference to bcc-Fe instead of Co/Rh source (as if "true" drive velocity). Besides a relative energy shift between a specific pair of radioactive source and absorber, values of isomer shift also depend on valence and spin state, and bonding of the target atoms in the specimen. Determination of its valence state and spin configuration from a Mössbauer spectrum is often reliable and straightforward. For example, high-spin Fe^{2+} (ferrous iron) has a range of isomer shift between 0.7 and 1.5 mm/s, while range of high-spin Fe^{3+} (ferric iron) spans from 0.3 to 0.6 mm/s [62, 63]. Even though Fe^{2+} and Fe^{3+} have the same s electron configuration, their d electrons help with shielding charge from outer shell s electrons at the nucleus, and their different $3d$ electron configurations result in different isomer shifts. Determining the change of the bonds and ligands of Fe atoms is also possible from the isomer shift, especially with references from the literature and databases. The isomer shift is influenced by different σ or π acceptance strength of surrounding ligands, ligand coordination, change of covalency, and other phenomena.

The second-order Doppler shift has to be considered when information about isomer shifts is extracted from temperature-dependent measurements. This thermal shift is caused by the slight change of absorber's mass after absorbing a photon ($\Delta m = E_p/c^2$). This mass change increases dynamics (i.e., velocity quadratic mean) of the absorber at elevated temperatures:

$$E_{2nd} = \Delta(\frac{p^2}{2m}) = \frac{p^2}{2}(\frac{-\Delta m}{m^2}) = -\frac{1}{2}\frac{< v^2 >}{c^2}E_p \ . \tag{2.13}$$

For ^{57}Fe, $E_{2nd} = -7.3 \times 10^{-4}$ mm/s/K.

2.1.3.2 Electric quadrupole splitting

Electric quadrupole splitting (EQS) is the hyperfine interaction between the nuclear quadrupole moment and the electric field gradient. By expanding the charge potential of the nucleus, the third term after monopole and dipole moment, its electric quadrupole moment $\mathbf{Q}$, is nonzero, given by a 3×3 tensor

$$\mathbf{Q} = \frac{1}{4\pi\epsilon_0}\frac{1}{2R^3}\sum Q_{ij}e_i e_j \ , \tag{2.14}$$

where e_i and e_j are unit vectors for Cartesian coordinate system $(i, j = x, y, z)$. When the nucleus is in its excited state with $I > \frac{1}{2}$, the shape of nucleus is not spherical. An elongated nucleus has a quadrupole moment.

The electric field gradient (EFG) of the surrounding electrons is the Laplacian of their overall electric potential, also in the form of 3×3 tensor, $\partial V/\partial e_i \partial e_j$. When the surrounding charge distribution is not isotropic, the shape of EFG becomes non-spherical. An orientation can be found relative to z axis, so that tensor components $\partial V/\partial e_i \partial e_j$ vanishes for all $i \neq j$. Since the electrostatic potential must satisfy the Laplace's equation

$$V_{xx} + V_{yy} + V_{zz} = 0 \ , \tag{2.15}$$

and assuming $|V_{xx}| \leq |V_{yy}| \leq |V_{zz}|$, only two independent variables, V_{zz} and η, are needed. The asymmetry parameter η is

$$\eta = (V_{xx} - V_{yy})/V_{zz} \ . \tag{2.16}$$

The interaction between the nuclear quadrupole moment $\mathbf{Q}$ and the EFG is described by the Hamiltonian

$$\mathcal{H}_{EQS} = eQV_{zz}\frac{3I_z^2 - I(I+1) + \eta(I_x^2 - I_y^2)}{4I(2I-1)} \ . \tag{2.17}$$

For ^{57}Fe and other isotopes with a nuclear spin transition from $I = \frac{1}{2}$ to $I = \frac{3}{2}$, $\mathbf{Q}$ of ground state is zero. Only the excited state has different eigenvalues for the Hamiltonian in Eq. 2.17, which split the energy for resonant absorption into two lines, with the difference between them

$$E_Q = \frac{1}{2}eQV_{zz}\sqrt{(1 + \eta^2/3)} \ . \tag{2.18}$$

The separation of the two absorption lines is often referred to as "electric quadrupole splitting" (EQS). As shown in Eq. 2.18, the EQS is largely affected by the asymmetry of EFG. This asymmetry can be caused by different distributions of the electron density from s,p,d electrons, the configuration of valence state, and bonding in the lattice. For example, many experiments show that high-spin $(S = 2)$ Fe^{2+} has larger EQS than high-spin $(S = 5/2)$ Fe^{3+}. According to crystal field theory, the five $3d$ orbital are half filled by the five $3d$ electrons in high-spin Fe^{3+}. Adding the sixth electron to

these 3d states increases the asymmetry of the overall charge distribution, which results in a larger EQS for Fe^{2+}.

2.1.3.3 Magnetic dipole splitting

A nucleus, either a proton or neutron, has a magnetic moment μ. When this magnetic moment interacts with the effective magnetic field of surrounding electrons, the "hyperfine magnetic field" (HMF), the nuclear energy levels are split into (2I+1) components. The interaction Hamiltonian is

$$\mathcal{H}_{HMF} = -\overrightarrow{\mu} \cdot \overrightarrow{B_{eff}} = -g\mu_N \overrightarrow{I} \cdot \overrightarrow{B_{eff}} = -g\mu_N B I_z \ , \tag{2.19}$$

where g is the nuclear gyromagnetic ratio, μ_N is the nuclear magneton, and I_z is the z-component of nuclear spin I with possible values of $-I$, $-I+1$,...,$I-1$, I.

2.1.4 Dynamical phenomena

2.1.4.1 Valence fluctuation

The EFG can fluctuate as a random function of time either by reversing its direction along z axis or by changing among z, x, and y axes [64]. Causes of fluctuations include electron hopping, diffusion of vacancies, atoms, ions or charges, and Jahn-Teller distortion. The electron hopping process (or a polaron hopping process when polarized field from crystal lattice is involved in an ionic solid) usually occurs in a mixed valence compound such as Fe^{2+}/Fe^{3+}, between Fe^{2+} and Fe^{3+}, with a thermal activation. It is often referred to as a "valence fluctuation". It requires the two types of Fe ions to be in similar or equivalent environment, e.g., center of adjacent corner-sharing or edge-sharing polyhedra with oxygen [65]. Also, the Franck-Condon principle in crystal field theory expects a vibronic coupling between two adjacent Fe in which vibrational wave functions spatially overlap significantly.

The nuclear lifetime at the excited state serves the upper limit time scale for this dynamical effect to be observed, ~ 100 ns for ^{57}Fe. When the electron hopping is slower than this characteristic time, the nucleus sees each EFG configuration independently. In other words, fluctuations slower than 100 ns are considered static by Mössbauer spectrometry. When the electron hops faster than the time scale from energy of EQS (by uncertainty principle), the nucleus sees a time-averaged EFG at both Fe^{2+} and Fe^{3+}, showing superposed features from the two valences in a Mössbauer spectrum. In the extreme case when hopping frequency is too high, the isomer shift will be an average of the two valences, and the EQS will collapse to a single line if the average is isotropic.

2.1.4.2 Superparamagnetic relaxation

Magnetic nanocrystalline materials often exhibit a dynamical effect of superparamagnetism. An important time scale for HMF in Mössbauer spectrometry is the Larmor precession frequency (or period). The nuclear magnetic moment can choose an orientation with an angle θ away from the direction of the effective magnetic field $\overrightarrow{B_{eff}}$. The nuclear magnetic moment then precesses in $\overrightarrow{B_{eff}}$. This Larmor precession provides a "clock" with its characteristic frequency. For ferromagnetic bcc ^{57}Fe, the characteristic nuclear precession frequency is 34 MHz (30 ns). If the transition rate is lower than the precession frequency, the nucleus will effectively see a static HMF. If the HMF alters faster than the nuclear precession, the nucleus can only see time-averaged fields of several HMFs. In the intermediate region, the spectrum is complex.

Small particles of ferromagnetic materials have a single domain of magnetization. If the particle grows large enough, energy in the external magnetic field exceeds that of forming a domain boundary, and the particle decomposes into smaller domains with different magnetization. In the other extreme when particles become small enough, thermal energy can reverse the magnetization of the entire nanocrystal. The energy required to reverse a magnetization has the form of κV, which is the domain volume times an anisotropy energy barrier. The frequency for a spontaneous reversal of magnetization is:

$$f = f_0 \exp(-\frac{\kappa V}{k_B T}) \,, \tag{2.20}$$

where the prefactor f_0 is of order 10^8 – 10^{12} Hz. When the crystal size is reduced below a certain range at a given temperature, the flipping frequency f becomes higher than the Larmor frequency. As described above, instead of seeing a HMF from a magnetic ordered structure, the nucleus sees a time-averaged field of zero and shows a Mössbauer spectrum with paramagnetic features. This fast dynamics of reversing magnetization in magnetic nanocrystallites is known as "superparamagnetic relaxation". Since there is usually a distribution of crystal sizes in a polycrystalline sample instead of a uniform size, only a fraction of the particles gain a frequency higher than needed for superparamagnetism at certain temperature. Therefore, the Mössbauer spectrum of this sample shows different mixtures of both magnetic features and superparamagnetic features at different temperatures. Acquiring Mössbauer spectra at varied temperatures provides a way of estimating the size distribution of the particles.

2.2 Experimental techniques

2.2.1 Sample preparation

For room-temperature measurements, aluminum plates with different thicknesses were used as sample holders. The Al plates have an open window of 1.27 cm in diameter at the center. Fine powder

samples were packed with uniform thickness for γ-ray beam transmission, and sealed with Kapton tape between the Al plates. The physical thickness of the sample is about the same as that of the Al plate. A more sophisticated approach calculates the needed weight of specimen from multiplication of optimized thickness, window area, and powder density.

If the sample is too thin, there may not be sufficient resonant nuclei, so the absorption remains small and the statistical scatter is relatively large. On the other hand, if the sample is too thick, most of the incident photons can be attenuated and the count rate becomes small. Therefore, optimizing sample thickness is often important in Mössbauer spectrometry. Assuming photon emission from the source is constant, N counts per unit time, the number of transmitted photons drops exponentially with sample thickness t, when scattering is off resonance

$$N_{off} = N \exp(-\overline{\mu}\rho t) \ , \tag{2.21}$$

where $\overline{\mu}$ (in unit of cm^2/g, for 14.4 keV photons) and ρ are the averaged mass attenuation coefficient and density.

$$\overline{\mu} = \sum \frac{m_i}{m_{total}} \mu_i \ . \tag{2.22}$$

When scattering is on resonance, counts of transmitted photons will further drop by a factor of $f_s a(t)$ due to resonant absorption at target atoms,

$$N_{on} = N \exp(-\overline{\mu}\rho t) f_s a(t) \ , \tag{2.23}$$

where f_s is the recoilless fraction at the source. The factor $a(t)$ is given by [66, 67, 68]

$$a(t) = 1 - \exp(-\frac{1}{2} f_a n \sigma t) J_0(\frac{1}{2} i f_a n \sigma t) \ , \tag{2.24}$$

where f_a is the recoilless fraction at the absorber, n is the number of resonant nuclei per cm^3, and σ is the cross section of resonant nuclei. $J_0(x)$ is the zero-order Bessel function with an imaginary argument. Criteria for optimizing sample thickness include largest dip, largest area, or best signal-to-noise ratio (SNR). Only the best SNR is considered here:

$$SNR = N_{on}/\sqrt{N_{off}} = N^{1/2} \exp(-\overline{\mu}\rho t/2) f_s (1 - \exp(-\frac{1}{2} f_a n \sigma t) J_0(\frac{1}{2} i f_a n \sigma t)) \ . \tag{2.25}$$

The derivative of SNR with respect to t is expected to go to zero at the optimized thickness t_0. However, with the Bessel function in Eq. 2.25, only a complicated dimensionless equation containing t_0 can be obtained [67, 68, 69]. Since $J_0(x)$ approaches 1 when x is close to zero, resonant absorption in Eq. 2.25 may be simplified to exponential attenuation. In addition, f_s can be approximated to

1. Eq. 2.25 becomes

$$SNR = N^{1/2} \exp(-\overline{\mu}\rho t/2)(1 - \exp(-\frac{1}{2} f_a n\sigma t)) \; . \tag{2.26}$$

Defining $k = f_a n\sigma$,

$$dSNR/dt = N^{1/2} - \frac{\overline{\mu}\rho}{2} \exp(-\overline{\mu}\rho t/2) + \frac{\overline{\mu}\rho + 2k}{2} \exp(-\frac{\overline{\mu}\rho}{2} - kt) \; . \tag{2.27}$$

When $dSNR/dt = 0$,

$$t_0 = -\frac{1}{k} \ln \frac{\overline{\mu}\rho}{\overline{\mu}\rho + 2k} = -\frac{1}{f_a n\sigma} \ln \frac{\overline{\mu}\rho}{\overline{\mu}\rho + 2 f_a n\sigma} \; . \tag{2.28}$$

Use natural Fe as an example, where $\overline{\mu} = 57.08\,\mathrm{cm}^2/\mathrm{g}$, $\rho = 7.86\,\mathrm{g/cm}^3$, $f_a n\sigma = 0.8 \times 0.022 \times 7.86/55.85 \times 6.023 \times 10^{23} \times 25 \times 10^{-19}\,\mathrm{cm}^{-1} = 3834\,\mathrm{cm}^{-1}$, $t_{Fe,0} = 7.55\,\mu\mathrm{m}$. In the case of $LiFePO_4$, where $\overline{\mu} = 23.69\,\mathrm{cm}^2/\mathrm{g}$, $\rho = 3.42\,\mathrm{g/cm}^3$, $f_a n\sigma = 621.7\,\mathrm{cm}^{-1}$, $t_{LiFePO_4,0} = 45\,\mu\mathrm{m}$. In the limit where there are very few target nuclei in the sample, i.e., $f_a n\sigma \ll \overline{\mu}\rho$, $t_0 \to 0$. This means sample has to be as thin as possible to give a good SNR.

2.2.2 Experimental setup

A ^{57}Co radioactive source from Cyclotron® Co. Ltd was used. It has ^{57}Co a in 7-μm-thick Rh matrix, mounted in an Al holder with a 20 μm Kapton window, with a line width of 0.109 mm/sec and recoilless fraction of 0.78 (data provided by the manufacturer). The intensity was 50 mCi measured in January 2009. The source is attached to the Mössbauer velocity transducer (Wissel® MDU-1200) and moves in a constant acceleration/deceleration motion controlled by a digital function generator (Wissel® DFG-1200).

The spectrometer is configured for transmission, as each photon travels linearly from the velocity transducer through the sample, and into the detector. Two detectors were used for gamma ray detection. The first one is a gas-filled detector with a plexiglass window on a cylindrical Al tube sealed by epoxy. The central anode wire is 0.002-in Au-plated W wire made by California Fine Wire Company. The detector is filled with P10 gas (90% Ar/10% CH_4) with a slow flow rate. Ar atoms ionized by incident photons fly to the cathode. Electrons are attracted to the anode wire and generate pulses, proportional to the photon energy. The pulses are shaped and amplified. Methane is used as quenching gas to prevent continuous electric discharge in the counter. A more costly and efficient Si detector (Amptek® XR-100CR) is alternatively used for measuring spectra from small samples. It has a Be window and a PIN (p-doped/intrinsic/n-doped) Si diode, so photons can deplete the intrinsic area and generate electric signals as electrons and holes drift to the electrodes. The detector is cooled by thermoelectric cooling. In the Single Channel Analyzer (SCA), the shaped analog signals are selected by a pair of discriminators and converted to TTL pulses. A multichannel analyzer (MCA) synchronizes counting TTL pulses and Mössbauer drive motion, usually with the

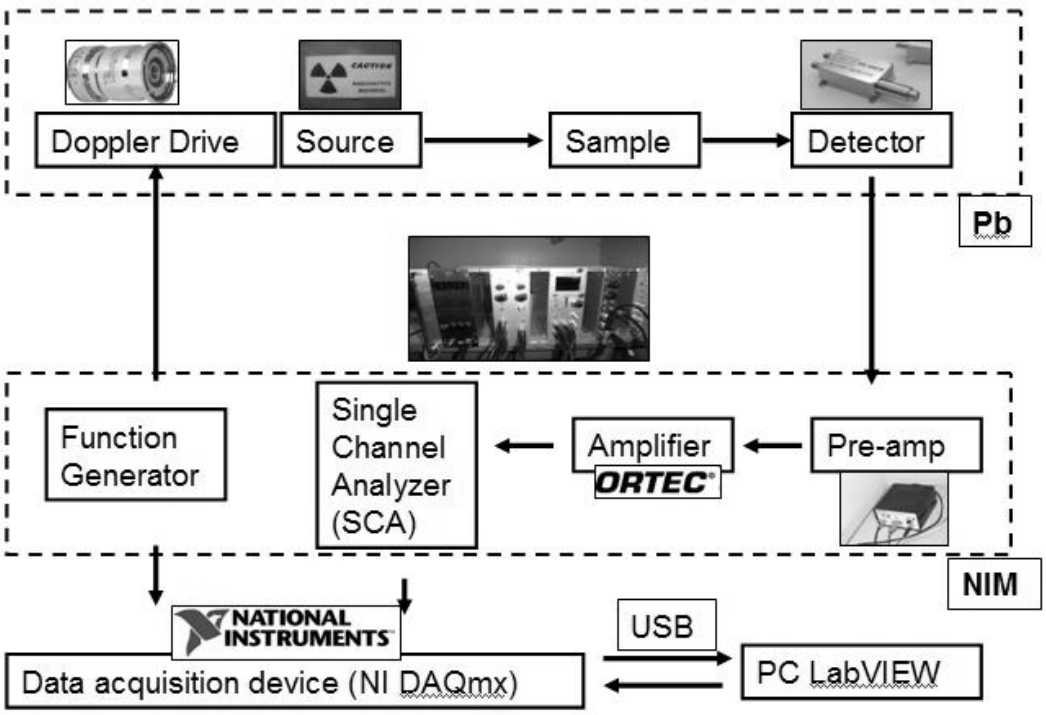

Figure 2.1: Illustration of the Mössbauer spectrometer setup

aid of a microprocessor or microcomputer control. A graphic illustration of the spectrometer setup is shown in Fig. 2.1.

A novel software-simulated MCA was constructed with a National Instruments 32-bit counter and a LabVIEW program. More description can be found in the appendix.

2.2.3 Furnace

A customized furnace was made for acquiring Mössbauer spectra at elevated temperatures, shown in Fig. 2.2. The core of the furnace consists of three pieces of aluminum plates, screw-tightened together with the same opening window at the center of the plates. Samples were sandwiched by Kapton tape in the central Al plate. Two resistive heating sticks (10 ohm each) were glued on one side of the core plates. Temperatures were read from three or four K-type thermocouples taped on the central plate at different positions. Temperature variations were less than 1° when heated to 200°C. The core of the furnace was wrapped with heat-resistant SiO_2 fibers and placed vertically inside a cardboard box with a graphite foil window. A variable DC power supply with a maximum of 20 V was used to heat the parallel-connected resistors.

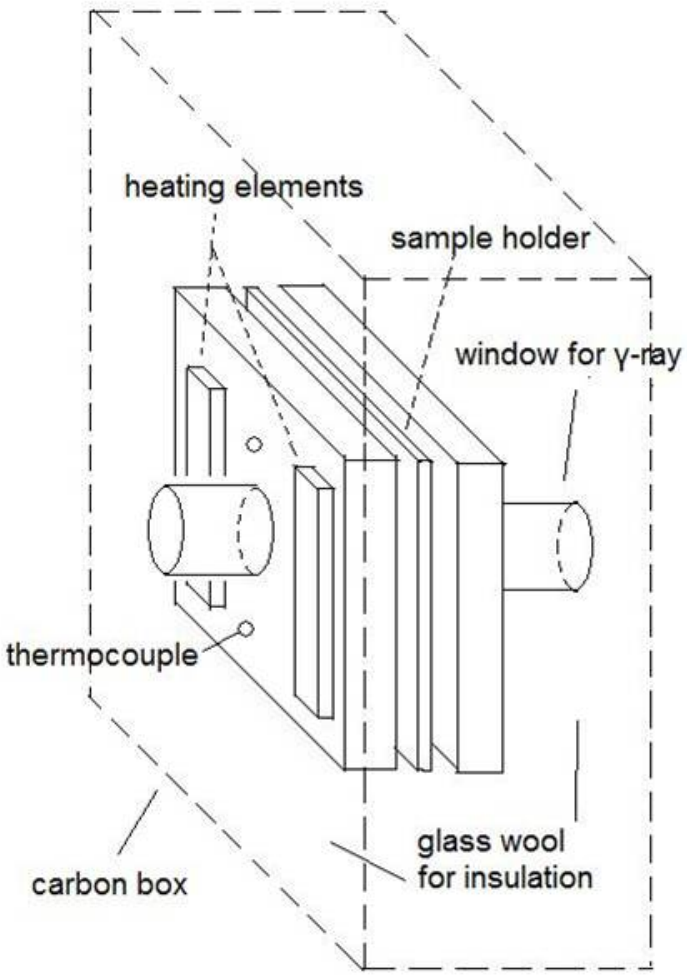

Figure 2.2: Sketch of the customized furnace used with the Mössbauer spectrometer at high temperatures

Chapter 3

Overview of $LiFePO_4$

3.1 Crystal structure

As the cathode material for lithium-ion batteries, $LiFePO_4$ has several advantages over many commercialized cathodes. It is made from elements that are abundant in nature, which lowers the manufacturing cost. It can be reversibly discharged at 3.45 V with a gravimetric capacity of 170 mAh/g, giving high energy density. It is stable against overcharge and has a long cycle life. Moreover, disposing it generates no contamination to the environment.

In nature, Li(Fe,Mn)PO_4 crystalizes in orthorhombic structure in space group *pnma* (# 62) and is known as triphylite (denoted T). Its X-ray diffraction pattern is shown in Fig. 3.1. By Rietveld refinement, the lattice parameters of this olivine-type structure are $a = 10.33\,\mathring{A}$, $b = 6.01\,\mathring{A}$, $c = 4.69\,\mathring{A}$, and the unit cell volume is $V = 291.2\,\mathring{A}^3$. The structure consists of corner-shared FeO_6 octahedra in the *bc* plane, edge-shared LiO_6 octahedra parallel to b-axis, and corner-shared PO_4 tetrahedra [70, 71]. Upon lithium extraction from the electrode, $LiFePO_4$ is oxidized to become $FePO_4$:

$$LiFe(II)PO_4 \rightarrow Fe(III)PO_4 + Li^+ + e^- \,, \tag{3.1}$$

with the Fe valence changing from Fe^{2+} to Fe^{3+}. $FePO_4$ (denoted H, for its mineral name heterosite) has the same olivine structure with lattice parameters $a = 9.81\,\mathring{A}$, $b = 5.79\,\mathring{A}$, $c = 4.78\,\mathring{A}$, and unit cell volume $V = 271.5\,\mathring{A}^3$ obtained from its XRD pattern (Fig. 3.2). From $LiFePO_4$ to $FePO_4$, the volume of the unit cell is changed only by 6.77%. The good reversibility of $LiFePO_4$ is largely attributed to this small change of its crystal lattice upon lithiation and delithiation.

Since the O atoms are strongly bonded with both Fe and P atoms in both triphylite and heterosite, olivine $LiFePO_4$ has an outstanding stability compared to hexagonal $LiCoO_2$, even up to 400°C. This is evident in the in situ $LiFePO_4$ Raman spectra in Fig. 3.3. The high-frequency peaks in the Raman spectra of $LiFePO_4$ correspond to vibrational modes of the P-O bonds, which have no visible change at elevated temperatures up to 400°C. The XRD patterns also show no variation when heated

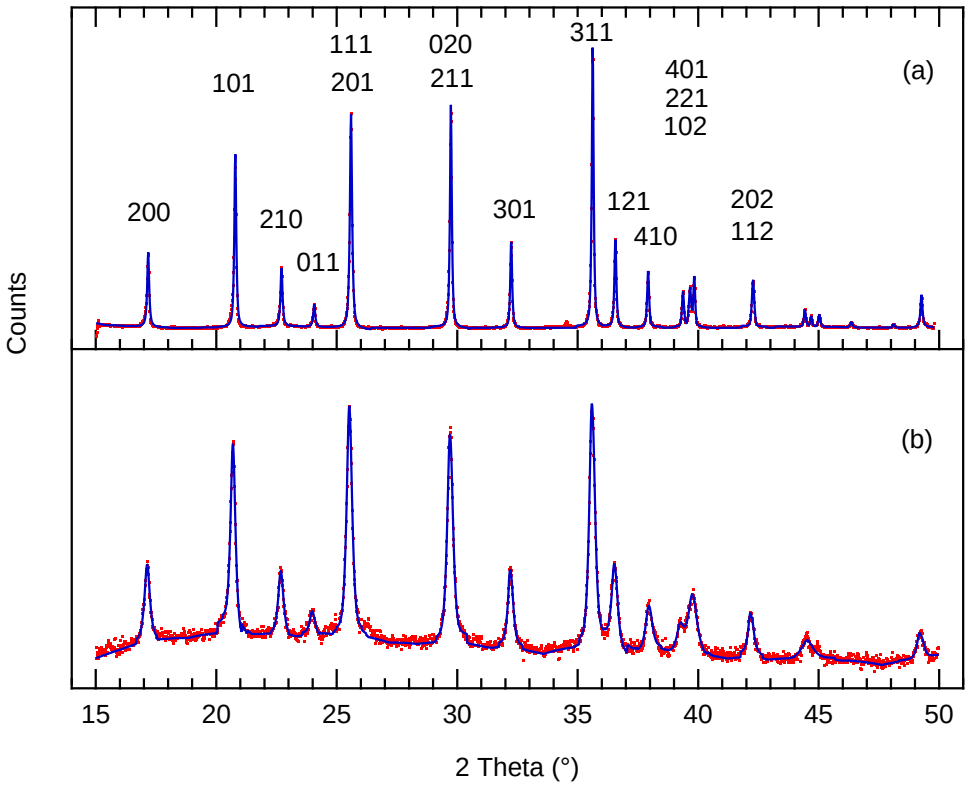

Figure 3.1: X-ray diffraction patterns of olivine $LiFePO_4$, (a) sample prepared by Argonne National Laboratory [1], (b) commercial electrode by A123® Inc. Diffraction peaks were indexed as the orthorhombic crystal structure in *pnma* space group.

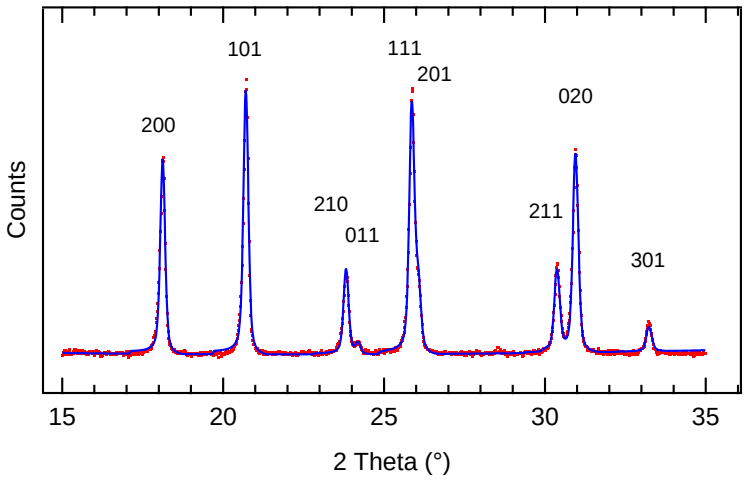

Figure 3.2: X-ray diffraction patterns of $FePO_4$, prepared by chemical delithiation [2]. Diffraction peaks were indexed as the orthorhombic structure in *pnma* space group.

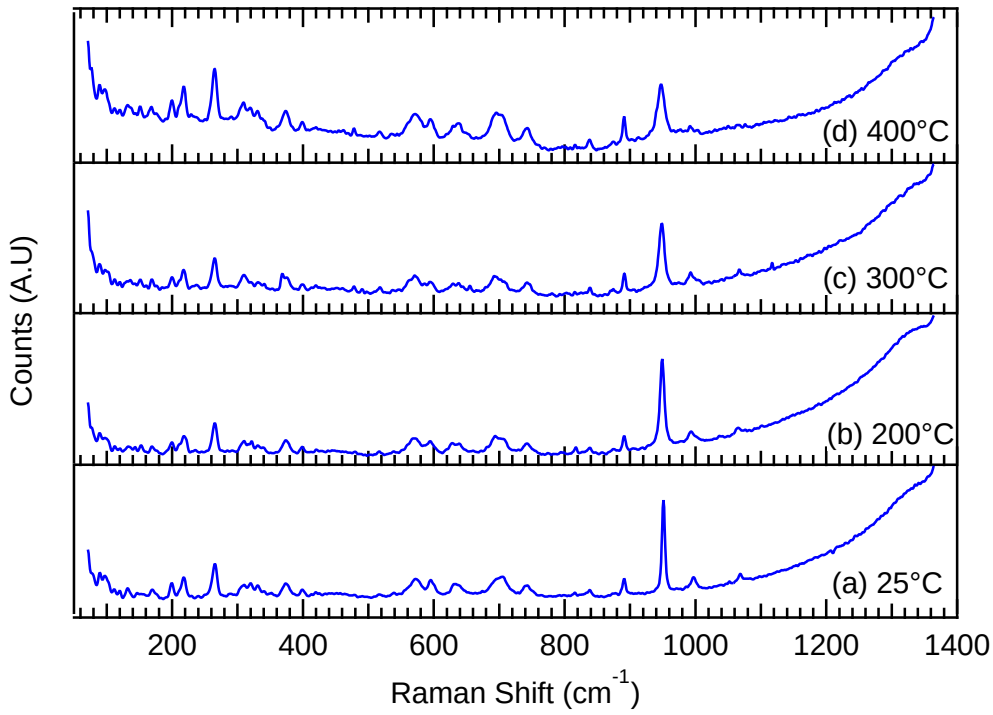

Figure 3.3: Raman scattering spectra of $LiFePO_4$ acquired at elevated temperatures: (a)25°C, (b)200°C, (c)300°C, and (d)400°C

up to 400°C. The small lattice change between triphylite and heterosite also leads to a modest lattice strain, providing the material excellent cycling performance and high energy efficiency.

3.2 Phase composition

During either charging or discharging, the cathode comprises a two-phase mixture of triphylite and heterosite (T+H) across most of the composition range. The phase transformation occurs through movement of an inter-phase boundary. The two-phase T+H can be expressed as $x\text{LiFePO}_4 + (1-x)\text{FePO}_4$, where x ($0 \leq x \leq 1$) is an indication of lithium concentration and charged/discharged state.

Upon heating, a phase transition from the two-phase mixture (T+H) to a homogeneous solid solution was discovered at around 200°C by X-ray diffraction [72]. This solid solution has the same olivine structure as triphylite and heterosite, with intermediate lattice parameters [72, 2]. A neutron diffraction study also showed that Fe-O and Li-O bonds have intermediate distances between those of pure $LiFePO_4$ and $FePO_4$ [73]. It appears that there is no long-range order of Li ions in the solid solution phase. The Li_xFePO_4 solid solution can be quenched and preserved at room temperature for months, due to the slow kinetics of Li diffusion. This made it possible to study the solid solution

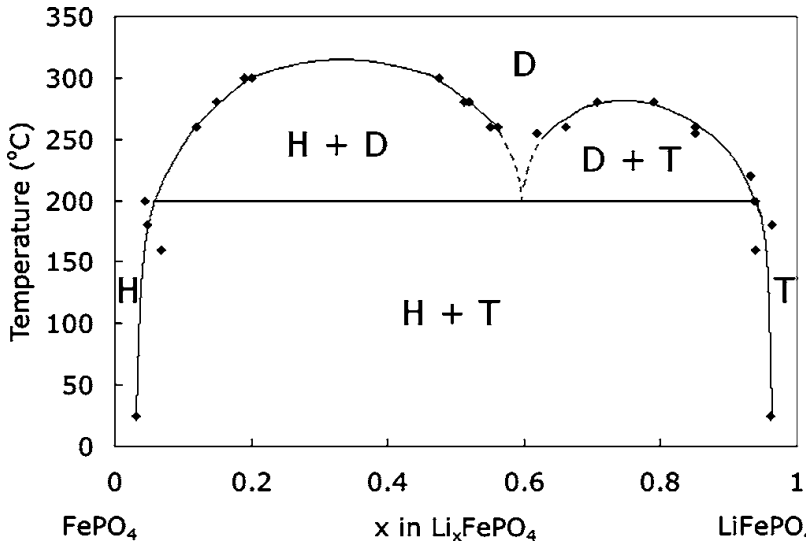

Figure 3.4: Phase diagram of $LiFePO_4$ (T, for triphylite), and $FePO_4$ (H, for heterosite) phases showing their merging to a solid solution (D, for disordered) in a eutectoid system. Figure from published work by Dodd et al. [3]

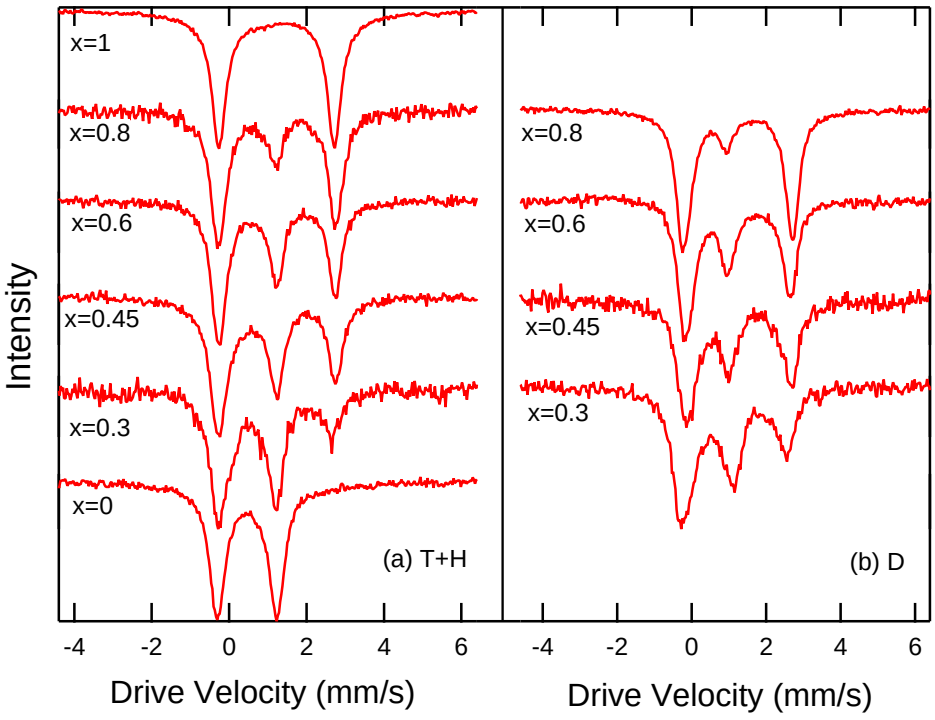

Figure 3.5: (a) Mössbauer spectra at 25°C of triphylite (x=1), heterosite (x=0), and two-phase Li_xFePO_4 with x=0.8, 0.6, 0.45, and 0.3. (b) Mössbauer spectra at 25°C of quench solid solution Li_xFePO_4 with x=0.8, 0.6, 0.45, and 0.3

behavior at temperatures below that of the phase transition. Mössbauer spectra of the Li_xFePO_4 solid solution at 25°C in Fig. 3.5 show distinctive local charge configurations of Fe^{2+} and Fe^{3+}, similar to those of a two-phase mixture.

The phase diagram assessed by XRD and DSC found a eutectoid point around x=0.6 [3] (Fig. 3.4). The cluster expansion was used to calculate formation energies of various Li/vacancy and Fe^{2+}/Fe^{3+} configurations in the lattice, to reproduce the phase diagram [74]. Electronic entropy was added to stabilize the eutectoid point around x=0.6.

At room temperature, a two-phase mixture of triphylite and heterosite is thermodynamically stable and occupies a wide range of composition. With a spinodal model, X-ray diffraction found that the intermediate Li_xFePO_4 ($\alpha < x < \beta$) region consists of two single phases $Li_\alpha FePO_4$ and $Li_\beta FePO_4$ with $\alpha = 0.032$ and $\beta = 0.962$ [75]. A further investigation by neutron diffraction determined a wider single-phase region with $\alpha = 0.05$ and $\beta = 0.89$ [73]. The solid-solution behavior in the electrochemical curve was seen in nanocrystalline $LiFePO_4$ and during fast discharging [76, 77]. The phase diagram for Li_xFePO_4 prepared as nanocrystallites was estimated to change as well [78, 79, 80], but this is not supported by other experimental results [81, 82].

3.3 Lithium and electron transport

Lithium diffusion in $LiFePO_4$ was first reported to be analogous to that in $LiCoO_2$ and other layered oxides in two dimension [70]. A core-shell model was proposed, as lithium is extracted from a particle surface while the surface area of the interface shrinks [83]. First-principles calculation on Li diffusion coefficients found the most likely paths are the one-dimensional channels along the b-axis with the lowest activation energy of 0.27 eV in the [010] direction [84]. Further computational work with the maximum entropy method confirmed this 1-D diffusion, and proposed the curved pathway of lithium motion through tetrahedral interstitial sites along the [010] direction [85]. Dislocations along the c-axis were found by high-resolution transmission electron microscopy when imaging ac planes [86]. The phase boundary was found to move in the a direction while lithium ions diffuse in the b direction, which contradicts the core-shell model. In another study, particles of single phases (either $Li_{1-y}FePO_4$ or Li_xFePO_4) were observed, and a domino-cascade model was proposed [87]. In this model, when the Li_xFePO_4 phase nucleates, the phase boundary quickly moves in the a direction (perpendicular to the b direction along which the lithium diffuses).

Experimental work on ionic and electronic conductivity of $LiFePO_4$ includes AC impedance measurements on crystals grown by a flux method [88], and DC polarization measurements on crystals grown by the optical floating zone method with titanium ion-blocking electrodes [89]. The results indicate an anisotropic ionic diffusion, and an activation energy of 0.6 eV for electronic conductivity in all directions. Small polaron hopping is now believed to be the mechanism of the

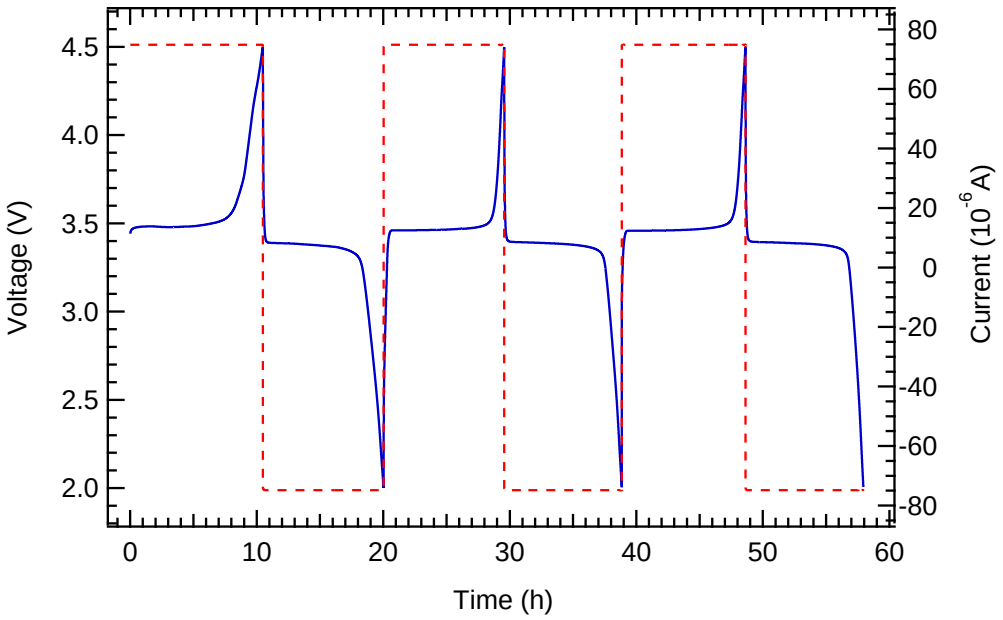

Figure 3.6: Galvanostatic cycling of $LiFePO_4$, at C/10 rate shown for the first 3 cycles. The solid line is the voltage profile, and the dashed line is the current.

electronic conductivity in $LiFePO_4$, like many ionic crystals with mixed valent states. Mössbauer spectrometry was used to measure the frequency and activation energy for the thermally activated polaron hopping in mixed Fe^{2+}/Fe^{3+} at different states of charge of Li_xFePO_4 prepared as two-phase mixtures and as solid solutions [90, 5, 2]. The measured activation energies varied from 300 meV to 600 meV, all higher than the DFT calculation on isolated free polaron transport in $LiFePO_4$ and $FePO_4$, in which activation energies of 215 meV and 175 meV were reported, respectively [91]. The coupling between Li ions and electrons was considered responsible for the increase of energy barrier for polarons.

3.4 Electrochemical performance

The potential curve of a $LiFePO_4$ cathode during galvanostatic cycling in a half cell (relative to a Li anode) shows a plateau of 3.45 V (Fig. 3.6). As discussed above, this plateau is evident for a two-phase mixture of triphylite and heterosite across a large range of composition during electrochemical lithiation and delithiation. Fast cycling with a high current density did not result in a drop of the voltage plateau as reported in the initial work on this cathode material [70]. With nanocrystalline $LiFePO_4$, the plateau was found to be replaced by a continuous potential variation [76, 77], as $LiFePO_4$ possibly took a solid solution pathway to suppress the energy cost of nucleation [92]. Figure 3.7 shows the evolution of the capacity and energy density of $LiFePO_4$ during cycling.

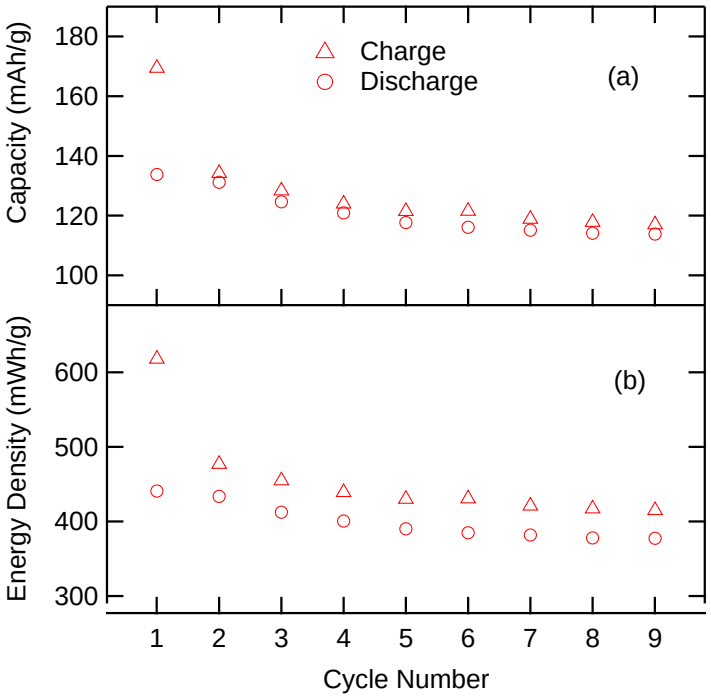

Figure 3.7: Evolution of the (a) capacity and (b) energy density during charge and discharge (C/10 rate) for the first 9 cycles, tested in a half- coincell with $LiFePO_4$ cathode

After 9 cycles, the cathode stabilized with about 70% capacity and energy density of its theoretical values.

Chapter 4

Synthesis and Strain Study of $LiFePO_4$ and Its Nanocrystallites

Our samples of nanocrystalline Li_xFePO_4 with the olivine structure were prepared by three different methods. This section describes the synthesis methods, and compares the crystal size and the lattice strain.

4.1 Introduction

Various methods have been adopted to synthesize lithium iron phosphate ($LiFePO_4$) including solid-state reaction, carbothermal reduction, aqueous precipitation, hydrothermal reaction, microwave heating, and pulsed laser deposition. Among them, the most common method is the solid-state reaction, grinding precursors without a solution environment and heating for long duration. Purity, crystalline formation, and crystalline sizes can be controlled during milling or annealing, as reported in several studies previously [70, 93, 94, 95, 96, 97, 1]. More practically, conductive carbon is often added with Li, Fe, and P precursors in solid-state reaction to prepare carbon-coated lithium iron phosphate ($LiFePO_4$/C), for the purpose of improving conductivity of $LiFePO_4$ and reducing ferric impurities.

Similarly, in mechanical attrition taking place in a planetary ball mill (like mechanical alloying) powders of Li, Fe, and P precursors are mixed in the vial in appropriate portions, and balls are added in certain weight ratio to the materials. The vial is sealed under inert gas atmosphere, and rotates vigorously in a high-speed mill to create collisions and stresses between balls and powders or vial and powders. Particles evolve continuously through repeated fracturing to a final state, usually ending up with submicron sizes. Particles are often composed of many nanocrystals, and are found to have large surface area and grain boundaries. However, secondary agglomeration often occurs and can be seen in an electron microscope.

Another practical method of synthesizing $LiFePO_4$ nanoparticles is aqueous precipitation, pro-

viding fine powders with uniform size distribution [98, 99]. $LiFePO_4$ is precipitated from mixed solutions of precursors with a careful control of temperature and pH value. The precipitates are then washed, dried, and annealed to form crystallites. Impurity phases are usually "co-precipitated" with $LiFePO_4$. Some impurity phases were found to be eliminated by adding carbon black or sucrose in the precursors [100, 101, 102, 103].

As described in this chapter, nanocrystalline $LiFePO_4$ was synthesized by both mechanical attrition and by aqueous precipitation. Ball-milling bulk $LiFePO_4$ material results in nanocrystalline triphylite phase with 25 nm crystal size, among the smallest so far reported in the literature.

4.2 Experimental

We usually prepared nanocrystalline $LiFePO_4$ by ball-milling bulk-size $LiFePO_4$ into nanoparticles. Samples of $LiFePO_4$ with large crystal sizes were first prepared by mixing iron oxalate ($Fe(C_2O_4)2H_2O$), ammonium dihydrogen phosphate ($NH_4H_2PO_4$) and lithium carbonate (Li_2CO_3) in a molar ratio of 1:1:0.5 in a ball mill, dried and reground, followed by annealing at 700°C with flowing N_2 gas for 24 hours, as described similarly by Amine et al. [1]. The above synthesis was done for us by Dr. K. Amine, Dr. J. Liu, and Dr. I. Belharouak at Argonne National Laboratory. These bulk-$LiFePO_4$ powders were then ball-milled at 400 rpm in Ar atmosphere to prepare samples of nano-$LiFePO_4$, in either stainless steel (Fe-Cr-Ni) or agate (SiO_2) vial and balls. Milling time varies from 2 h to 24 h. Typical ball-to-powder ratios are 5:1, 10:1, and 20:1. Longer time and larger ratios gave smaller crystallite sizes.

An alternative way of preparing nanocrystalline $LiFePO_4$ is a regular solid-state synthesis by annealing. Precursors of LiOH, $Fe(C_2O_4)2H_2O$, $NH_4H_2PO_4$, and carbon black (super P®) in a molar ratio of 1:1:1:3 were mixed and ground, followed by annealing with flowing N_2/H_2 mixed gas at 600°C or 700°C. Crystals grow during annealing, and the size can be controlled by varying annealing time, ranging from 5 h to 18 h. The added carbon black helps reduce Fe^{3+} and coats $LiFePO_4$ nanoparticles to reach higher conductivity. This synthesis was done for us by Dr. Steven Kaye and Dr. Mark Bailey at Wildcat Discovery Technologies.

We synthesized nano-$LiFePO_4$ by precipitation following a modification of procedures described by Delacourt et al [99]. Precursors of $FeSO_4$, H_3PO_4, and LiOH were mixed in aqueous solution in a molar ratio 1:1:3 to reach an optimized pH value of 7.3. Dimethyl sulfoxide (DMSO) was then added to the solution. Nanocrystalline $LiFePO_4$ precipitated after heating the solution to 108°C.

The two-phase mixture of nano-Li_xFePO_4 was obtained by chemically delithiating $LiFePO_4$ with $K_2S_2O_8$ in an aqueous solution, or with NO_2BF_4 in an acetonitrile solution.

A PANalytical X'pert PRO X-ray diffractometer (XRD) with Cu Kα radiation, a ZEISS 1550 VP field-emission scanning electron microscope (FE-SEM), and a Tecnai F30 transmission electron

microscope (TEM) were used to determine microstructure, phase compositions, and material morphology. Rietveld analysis with the software package Philips X'pert Plus was used to determine lattice parameters, strains, and crystal sizes.

4.3 Results

Samples prepared by mechanical attrition of larger crystals of $LiFePO_4$ into nanocrystals, and then delithiated were named Sample A. Figure 4.1 shows XRD patterns of two-phase $Li_{0.5}FePO_4$ with 3 different crystal sizes (300 nm, 70 nm, and 25 nm). Samples with about 300 nm particles are from partly delithiated bulk-$LiFePO_4$ before ball-milling (Fig. 4.1(a)). Samples with an averaged crystal size of 70 nm were obtained by ball-milling for 3 h at 400 rpm with a 10:1 weight ratio (Sample A1, Fig. 4.1(b)). Samples with an averaged crystal size of 25 nm were obtained by ball-milling for 5 h at 400 rpm with 20:1 ball-to-powder weight ratio (Sample A2, Fig. 4.1(c)). Stainless steel vial and balls were used and milling was done under Ar gas to protect the powder from oxidation. For ball-milled nanoparticles, the characteristic crystal sizes were confirmed by refining XRD patterns and using the Hall-Williamson method [104] to interpret the X-ray line broadening. Figure 4.2 shows the agglomeration of nanocrystallites, with powder particles with a range of $0.5 - 1\,\mu$m.

The series of XRD patterns shown in Fig. 4.3 are $LiFePO_4$ from milling with agate vial and balls. A ball-to-powder weight ratio of 5:1 and milling speed of 400 rpm were chosen. Crystal size was controlled by varying milling time. After 24 h, a lower limit of 36 nm was achieved. However, by using agate milling media, XRD and Mössbauer spectrometry found impurity phases after chemically delithiating the ball-milled triphylite samples.

Figure 4.4 presents XRD patterns of $LiFePO_4$ from a direct solid-state synthesis. Varying annealing time and temperature results in different sintered crystal sizes. Samples with crystal size $>$ 150 nm were annealed at 700°C for 18 h (Fig. 4.4(a)). Samples with 80 nm crystal sizes were annealed at 600°C for 10 h (Sample B1, Fig. 4.4(b)). Samples with 70 nm crystal sizes were annealed at 600°C for 5 h (Sample B2, Fig. 4.4(c)). Their characteristic crystal sizes were confirmed from peak width in XRD patterns and morphology in SEM images. Carbon impurities can also be seen in Figs. 4.4(b) and (c).

An XRD pattern from $LiFePO_4$ prepared by precipitation is shown in Fig. 4.5(a) (Sample C) and its delithiated two-phase mixture $Li_{0.6}FePO_4$ is shown in Fig. 4.5(b). The synthesized $LiFePO_4$ in Fig. 4.5(a) is a pure triphylite phase, also verified by Mössbauer spectrometry. Its mean crystal size is estimated to be 90 nm. However, probably due to some reaction between the amorphous impurity residues and oxidizer NO_2BF_4, the XRD pattern of the chemically delithiated $Li_{0.6}FePO_4$ found identified Fe^{3+} impurities in Fig. 4.5(b).

The lattice parameters, unit cell volume, internal strain, and crystal size of $LiFePO_4$ synthesized

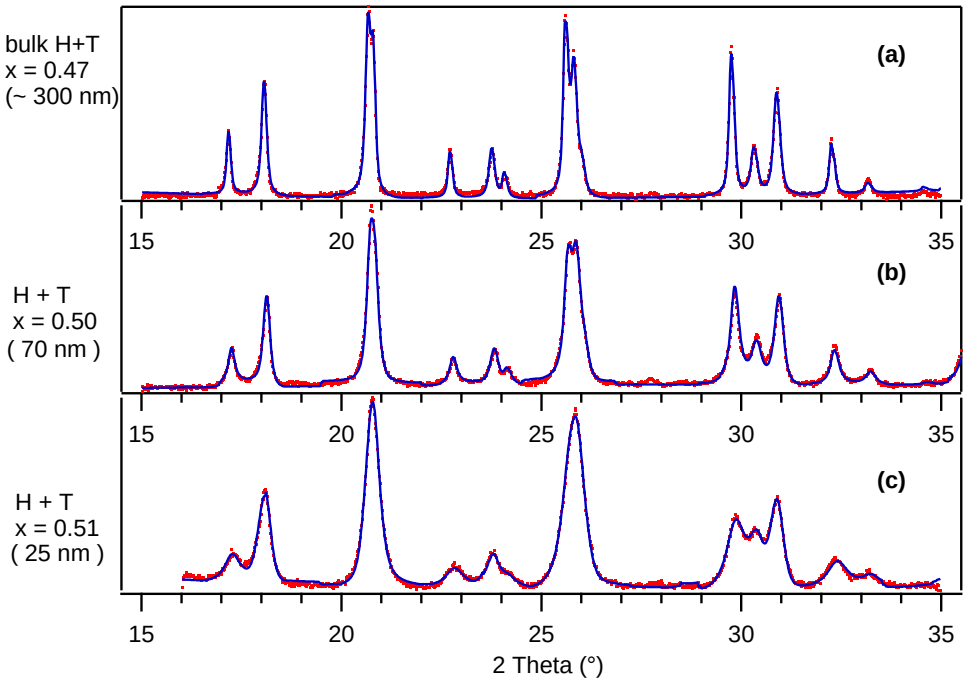

Figure 4.1: XRD patterns of $Li_{0.5}FePO_4$ before or after ball-milling $LiFePO_4$, followed by chemical delithiation. (a) Without ball-milling, crystal size is 300 nm, estimated from SEM and TEM. (b) Milled with 10:1 ball-to-powder weight ratio using steel balls and vial, 400 rpm 3 hrs under Ar, crystal size is 70 nm, estimated from XRD and TEM. (c) Milled with 20:1 ball-to-powder weight ratio using steel balls and vial, 400 rpm 5 hrs under Ar, crystal size is 25 nm, estimated from XRD and TEM.

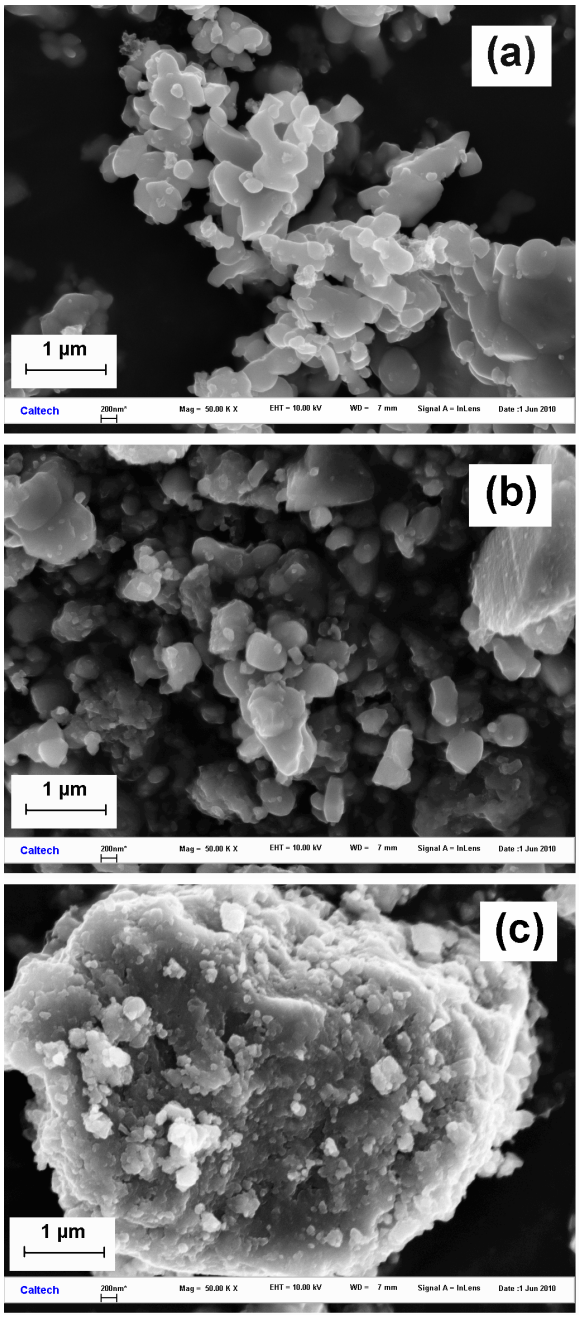

Figure 4.2: SEM images of $Li_{0.5}FePO_4$ with characteristic particle size of (a) 300 nm (before ball-milling), (b) 70 nm (after ball-milling), and (c) 25 nm (after ball-milling)

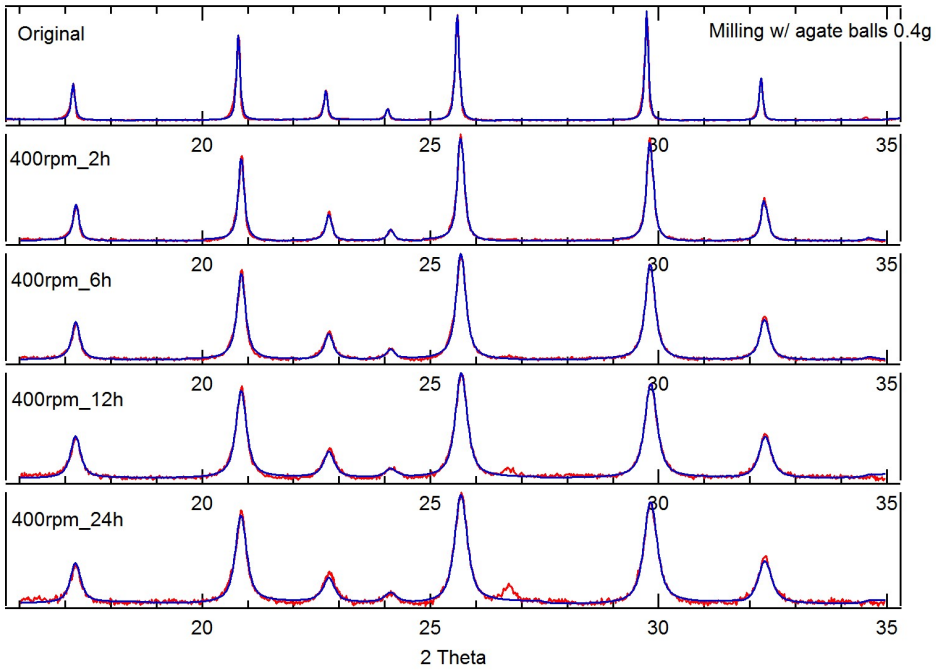

Figure 4.3: XRD patterns of $LiFePO_4$ before and after mechanical attrition with agate (SiO_2) balls and vial. Ball-to-powder weight ratio was 5:1 and crystal size can be controlled between 300 nm and 36 nm. Materials prepared with agate milling media, unfortunately, had impurity phases after chemical delithiation.

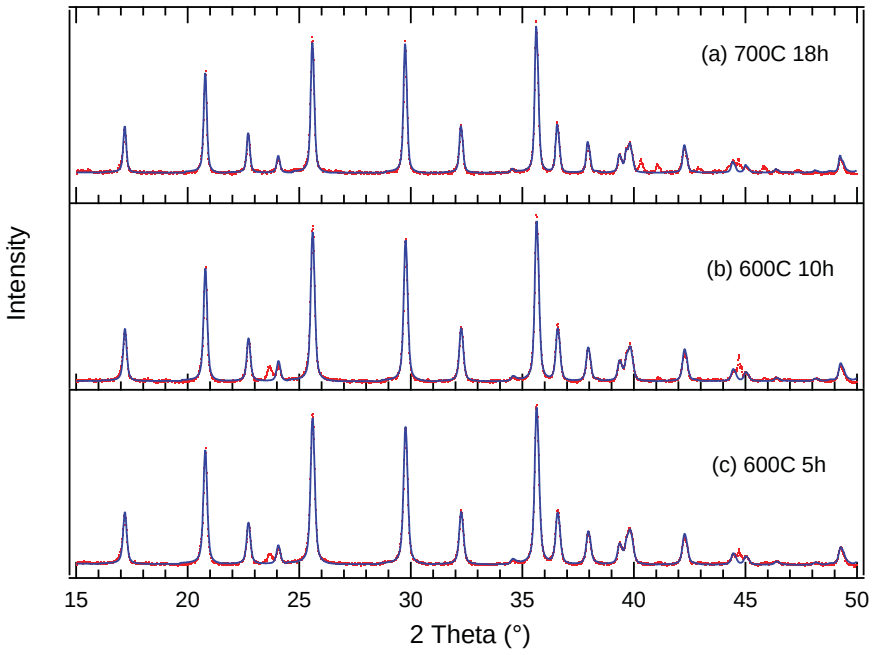

Figure 4.4: XRD patterns of $LiFePO_4$ synthesized from solid-state reaction by annealing at (a) 700°C for 18 h, (b) 600°C for 10 h (Sample B1), and (c) 600°C for 5 h (Sample B2)

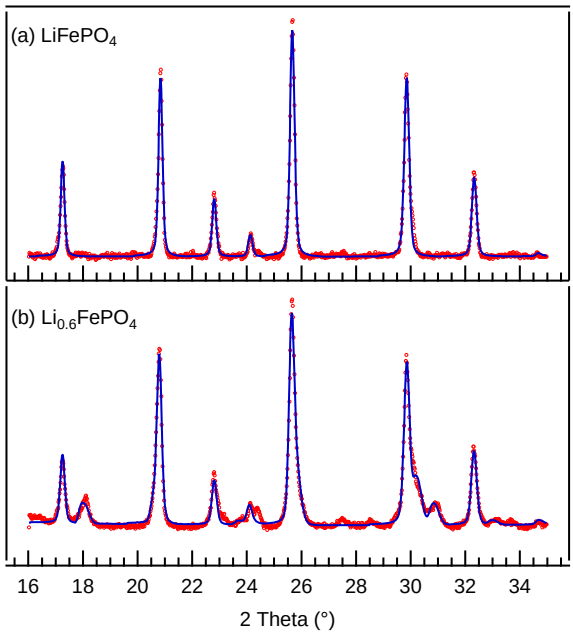

Figure 4.5: (a) XRD pattern of $LiFePO_4$ synthesized from co-precipitation of $FeSO_4$, H_3PO_4, and LiOH in DMSO solvent. (b) XRD pattern after chemical delithiation of $LiFePO_4$. Impurities with Fe^{3+} are identified.

Table 4.1: Structural characteristics, internal lattice strains, and mean crystal sizes of nano-$LiFePO_4$ synthesized by different methods. Samples A1 and A2 were obtained by mechanical attrition. Samples B1 and B2 were synthesized by solid-state reaction. Sample C was prepared by precipitation.

Sample	A1	A2	B1	B2	C
a[Å]	10.315	10.270	10.318	10.315	10.314
b[Å]	5.999	5.984	6.001	5.999	5.994
c[Å]	4.693	4.694	4.693	4.692	4.697
V[Å^3]	290.401	288.473	290.583	290.339	290.378
Strain[%]	0.41	0.76	0.35	0.36	0.29
Crystal size[nm]	70	25	80	70	90

different ways were analyzed using Rietveld refinement and are listed in Table 4.1. There is little difference in the lattice parameters of Sample A1, Sample B1, Sample B2, and Sample C, but Sample A2 (25 nm) has a 0.44% shorter side a and a 0.25% shorter side b. Sample A2 also has the largest strain distribution, probably due to the intensive ball milling. Sample C, which was obtained from precipitation in solution without any mechanical treatment, however, has a similar strain distribution to the samples prepared by ball milling.

4.4 Conclusion

$LiFePO_4$ nanocrystallites with the olivine structure were synthesized in three different ways. Mechanical attrition of bulk $LiFePO_4$ material by ball-milling can achieve crystal size as small as 25 nm.

An alternative routine of solid-state synthesis reduces crystal size by heating mixture of precursors at relatively low temperature ($\sim 600°C$) with carbon. The third method is precipitation of nano-$LiFePO_4$ from an aqueous solution. Physical and structural characteristics are similar among all samples, except for Sample A2 which has 25 nm crystal size.

Chapter 5

A Mössbauer Spectrometry Study of Thermally-Activated Electronic Processes in Li_xFePO_4

The solid solution phase of Li_xFePO_4 with different Li concentrations, x, was investigated by Mössbauer spectrometry at temperatures between 25°C and 210°C. The Mössbauer spectra show a temperature dependence of their isomer shifts (E_{IS}) and electric quadrupole splittings (E_Q), typical of thermally-activated, electronic relaxation processes involving ^{57}Fe ions. The activation energies for the fluctuations of E_Q and E_{IS} for Fe^{3+} are nearly the same 570±9 meV, suggesting that both originate from charge hopping. For the Fe^{2+} components of the spectra, the fluctuations of E_Q occurred at lower temperatures than the fluctuations of E_{IS}, with an activation energy of 512±12 meV for E_Q and 551±7 meV for E_{IS}. The more facile fluctuations of E_Q for Fe^{2+} are evidence for local motions of neighboring Li^+ ions. It appears that the electron hopping frequency is lower than that of Li^+ ions. The activation energies of relaxation did not have a measurable dependence on the concentration of lithium, x.

5.1 Introduction

Olivine-type Li_xFePO_4 ($0 \leq x \leq 1$) has been investigated as a promising cathode material for lithium ion batteries since 1997 [70]. This material has several attractive properties, such as low cost, a high capacity of 170 mAh/g, a high voltage of 3.5 V vs. Li^+/Li, environmental compatibility, and good thermal and chemical stability. Although methods of carbon coating and particle-size reduction have improved the electrical conductivity of practical Li_xFePO_4 electrode materials [93, 105, 99, 78, 106, 107, 108, 109, 110, 111, 112, 113, 114], low intrinsic electronic conductivity still may be a major challenge. Consistent measurements of intrinsic conductivity have proved difficult, with reported activation energies ranging from 150–1500 meV [106, 107, 115, 116, 117, 118, 119, 120, 121, 89].

A disordered solid solution phase of Li_xFePO_4 was discovered by in situ X-ray diffractometry

(XRD) at elevated temperatures [72]. This solid solution phase is kinetically stable after quenching to room temperature [3]. A transmission electron microscopy (TEM) study suggested that strain energy helps stabilize this phase during cooling [86]. In related work, the phase boundaries of the unmixed phases at room temperature were determined by neutron diffraction and open circuit voltage (OCV) measurements [73]. An experimental assessment of the phase diagram by XRD showed a eutectoid point around $x = 0.6$ and 200°C [3]. This disordered solid solution phase and its eutectoid point have generated considerable interest. The electronic and ionic conductivity of this phase may differ from the equilibrium two-phase mixture. Furthermore, a eutectoid point is not expected for a disordered solid solution dominated by a configurational entropy of mixing. A study of the phonon density of states (DOS) of $Li_{0.6}FePO_4$ by inelastic neutron scattering and differential scanning calorimetry (DSC) indicated that the vibrational entropy of mixing was much smaller than the larger configurational entropy of mixing, and probably does not alter the phase diagram qualitatively [122]. On the other hand, first-principles calculations indicated that a eutectoid point can be stabilized by an extra configurational entropy from electronic degrees of freedom [74].

Small polaron hopping is the expected mechanism for electronic conduction in Li_xFePO_4, as for other ferric/ferrous minerals. In the olivine-type orthorhombic structure of both $LiFePO_4$ (triphylite) and $FePO_4$ (heterosite), there are different distortions of FeO_6 octahedra around Fe^{2+} sites and Fe^{3+} sites. These distortions must accompany the motion of charge between Fe ions, a process called "small polaron hopping", and Li^+ ions may undergo motions in concert with the polarons. Additionally, Li^+ ionic transport has been studied together with surface morphology [123, 124, 125] and magnetic properties [126, 127].

Mössbauer spectrometry is an effective probe of local electronic structure and dynamics in iron compounds. Previous measurements on mixed-valence materials proved useful for assessing thermally activated electron delocalization between $Fe^{2+}$and Fe^{3+} and relaxation processes [65, 128, 129]. The heterosite-to-triphylite transformation was also studied by Mössbauer spectroscopy during charging and discharging of an electrochemical cell [71], and used for comparing different synthesis procedures [130]. The small polaron hopping process in Li_xFePO_4 was studied at high temperatures where a narrowing of absorption lines is observed in Mössbauer spectra [90]. A study of valence fluctuations in both $Li_{0.6}FePO_4$ two-phase mixtures and disordered solid solutions at elevated temperatures by Mössbauer spectroscopy showed rapid electronic fluctuations in the solid solution phase, but essentially no electronic dynamics in the two-phase mixture [5].

Here we extended the Mössbauer spectrometry results from our previous work [5] to investigate the dependence on Li concentration of valence and electric field gradient (EFG) fluctuations in the solid solution phase of Li_xFePO_4 (with different values of x) between 25°C and 210°C. Activation energies for the relaxations of isomer shifts and electric quadrupole splittings were obtained for both Fe^{2+} and Fe^{3+}. These were helpful for identifying a second source of fluctuations in Fe^{2+}

that is independent of charge hopping. We suggest it originates with local motions of Li^+ ions. Using this physical information with the Nernst-Einstein relations, intrinsic electronic and ionic conductivities were assessed from the hopping frequencies. The composition dependences of these activated processes were weak.

5.2 Experimental

Powders of $LiFePO_4$ were prepared by a solid-state reaction as described in previous work [1]. Two-phase mixtures of heterosite ($FePO_4$) and triphylite ($LiFePO_4$) were obtained by a chemical delithiation reaction using potassium persulfate ($K_2S_2O_8$) in an aqueous solution [3]. By altering the molar ratios of the reactants, four compositions were prepared: $Li_{0.3}FePO_4$, $Li_{0.45}FePO_4$, $Li_{0.6}FePO_4$, and $Li_{0.8}FePO_4$ ($x = 0.3, 0.45, 0.6, 0.8$). Disordered solid solutions were obtained by heating these materials for 12 hours at 380°C in vacuum-sealed glass ampoules, followed by quenching to room temperature. X-ray diffraction (XRD) patterns were obtained for all samples with a PANalytical X'pert PRO X'Celerator diffractometer using Cu Kα radiation. The diffraction patterns showed that the quenched samples retained the high temperature disordered solid solution phase, which had good stability at room temperature. (The quenched sample of $Li_{0.3}FePO_4$ contained some heterosite phase, however.) Rietveld analyses with the software package Philips X'pert Plus were used to determine lattice parameters and phase fractions. Samples were examined by XRD at the intermediate steps of preparation, and before and after Mössbauer spectrometry measurements at elevated temperatures.

Mössbauer spectrometry was performed with samples mounted and heated in a small electrical resistance furnace at fixed temperatures. The Mössbauer spectrometer was a conventional constant acceleration system with a ^{57}Co (in Rh) γ-ray source. Spectra were acquired for 12 hours at each temperature and again after cooling, to ensure that heating did not change the spectra measured at 25°C. These are measurable differences in the room temperature Mössbauer spectra of the two-phase mixture and the quenched samples for a particular composition x. These differences were consistent between samples, and did not change after annealing the samples at a temperature of 160°C for 10 hours, for example. Velocity and isomer shift calibrations were performed with reference to room-temperature α-Fe spectra. Quadrupole splitting (E_Q) distributions were analyzed by the method of Le Caër and Dubois [4] as a continuous function in the range 0 to 7 mm/s. A correlation between the isomer shift and E_Q distribution was assumed, with parameters determined by the best fits of the recalculated spectra to measured spectra.

5.3 Results

Figure 5.1 shows XRD patterns measured at 25°C for both two-phase mixtures of heterosite and triphylite, and for disordered solid solutions. All are similar to those reported previously [3, 87]. The phase diagram of $FePO_4$ – $LiFePO_4$ shows stable solid solutions above 350°C, but by rapid quenching this high-temperature equilibrium state can be retained at room temperature with good stability owing to slow atomic diffusion [3]. The solid solution has the same olivine structure as the triphylite and heterosite. The XRD patterns of the quenched solid solutions are consistent with patterns measured in situ at high temperatures [72]. In addition to the consistency of Mössbauer spectra of quenched samples, before and after annealing, further evidence for the stability of the samples is shown in Fig. 5.2. Lattice parameters of $Li_{0.45}FePO_4$ and $Li_{0.8}FePO_4$ solid solutions do not change after a 10-hour annealing at 160°C. However, heating above 210°C for 12 hours caused irreversible changes in the state of the material (except for $x = 0.6$), so our in situ Mössbauer spectrometry measurements were confined to temperatures of 210°C and below. The refinement results presented in Fig. 5.2 show a monotonic change of lattice parameters with Li concentration. Instead of straight lines, the concave-downwards curvature of lattice parameters, especially for the more robust results for the a-axis and b-axis, are distinctly different from a linear combination of two-phase mixtures. Although these XRD and Mössbauer results do not rule out some clustering of Li^+ or vacancies in the high-temperature solid solution phase, they do indicate that the clustering does not change at the lower temperature of our in situ measurements. Quenched samples can therefore be used to study disordered solid solutions at low and intermediate temperatures, without any observable changes in the structure.

Owing to the different distortions of the FeO_6 octahedra and the different valences of Fe^{3+} and Fe^{2+}, different electric field gradients (EFG) and isomer shifts (IS) are found for Fe^{3+} and Fe^{2+}. Mössbauer spectra of $FePO_4$ (heterosite with Fe^{3+}) and $LiFePO_4$ (triphylite with Fe^{2+}) at 25°C are shown in Fig. 5.3(a). These two spectra each show one quadrupole splitting, larger for the Fe^{2+} in triphylite than the Fe^{3+} in heterosite. Spectra of the other two-phase mixtures are approximately linear combinations of these two doublets. Spectra of the corresponding quenched solid solutions are shown in Fig. 5.3(b), and spectra of two-phase mixtures at 210°C are shown in Fig. 5.3(c). The spectra of the two-phase mixtures show little temperature dependence from 25°C to 210°C.

Figure 5.4(a) and (b) show quadrupole splitting (E_Q) distributions of heterosite and triphylite spectra at 25°C obtained with the fitting method of Le Caër and Dubois [4]. Both exhibit an approximate Gaussian distribution around a mean quadrupole splitting, associated with one doublet in their spectra (seen in Fig. 5.3(a)). For the Fe^{3+} and Fe^{2+}, the average E_Q are 1.59 mm/s and 2.96 mm/s with isomer shifts (IS) of 0.35 mm/s and 1.26 mm/s, respectively. Figure 5.4(c) and (d) show the E_Q distribution of the $Li_{0.6}FePO_4$ two-phase mixture and solid solution at 25°C. These

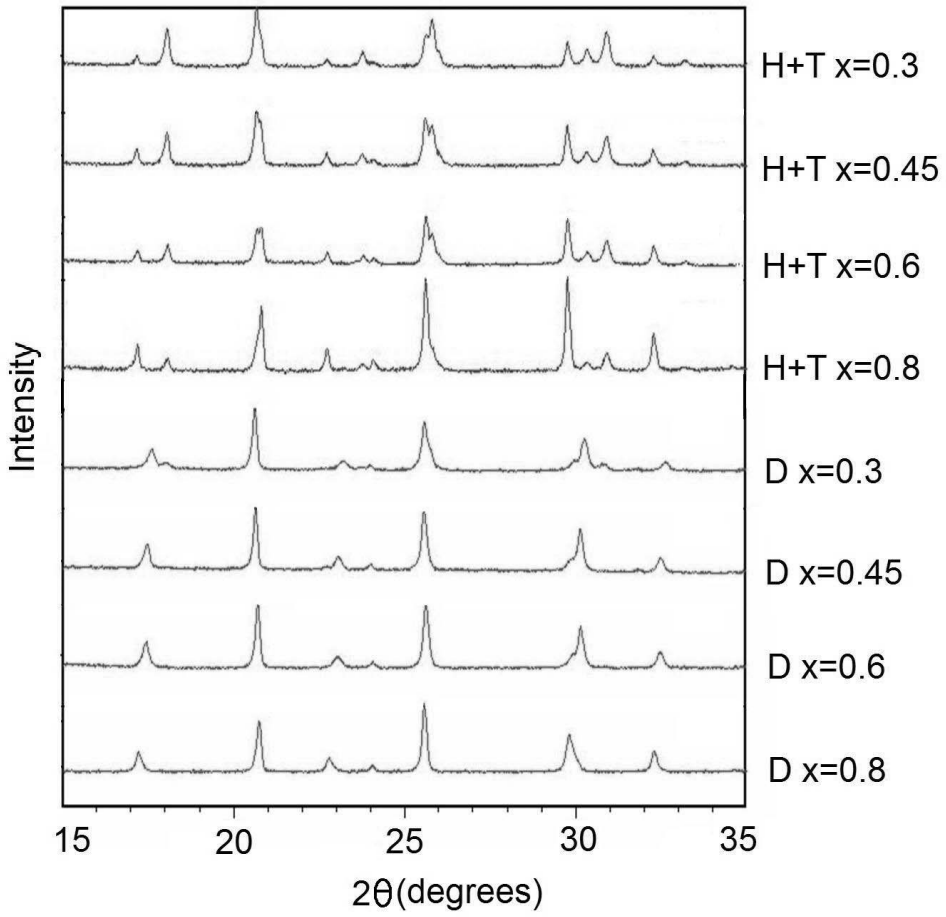

Figure 5.1: XRD patterns of two-phase mixtures (H+T) and quenched solid solutions (D) of Li_xFePO_4 at 25°C, with x=0.3, 0.45, 0.6, 0.8

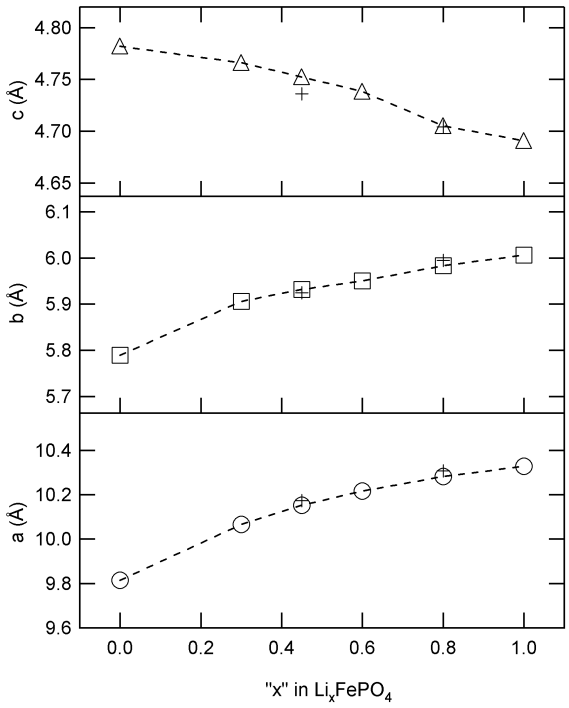

Figure 5.2: Lattice parameters a, b, and c (Å) of Li_xFePO_4 solid solutions for a range of x values. The cross markers show solid solution after annealing to 160°C for 10 hours and cooleding to RT in samples with x=0.45 and 0.8.

distributions show two local maxima corresponding to the two doublets in their Mössbauer spectra (the Fe^{2+} doublet is somewhat larger, consistent with the composition $x = 0.6$). The E_Q distribution of the disordered sample in Fig. 5.4(d) has a somewhat smaller E_Q (mean of 2.04 mm/s) than that of its two-phase counterpart in Fig. 5.4(c) (mean of 2.26 mm/s). Evidently the more homogeneous Li^+ arrangement in the solid solution weakens the average EFG at Fe sites. From the fitting analysis, the $Li_{0.6}FePO_4$ solid solution has two IS values, 0.187 mm/s and 1.19mm/s, which are somewhat smaller than those of heterosite and triphylite. As discussed below, analyses of the other solid solutions also gave two local maxima, i.e., evidence for two distinct local chemical environments of Fe, even at the temperature of 210°C, although the two IS values were merging together at 210°C. This is in contrast to spectra at much higher temperatures, where the disordered solid solution shows one doublet with an averaged valence [90].

Figure 5.5 shows Mössbauer spectra of disordered solid solutions with the compositions $x = 0.3, 0.45, 0.6$, and 0.8 at temperatures from 25°C to 210°C. Each temperature series shows a collapse of the doublets (changes in the Fe^{2+} are the most obvious, and start at the lowest temperatures) and distortions of the spectral lineshapes, indicating a dynamical relaxation process with a time scale within the Mössbauer window of 1 to 100 ns. Interestingly, we did not observe the same phenomena in spectra of two-phase mixtures at 210°C — their spectra showed very little change at elevated

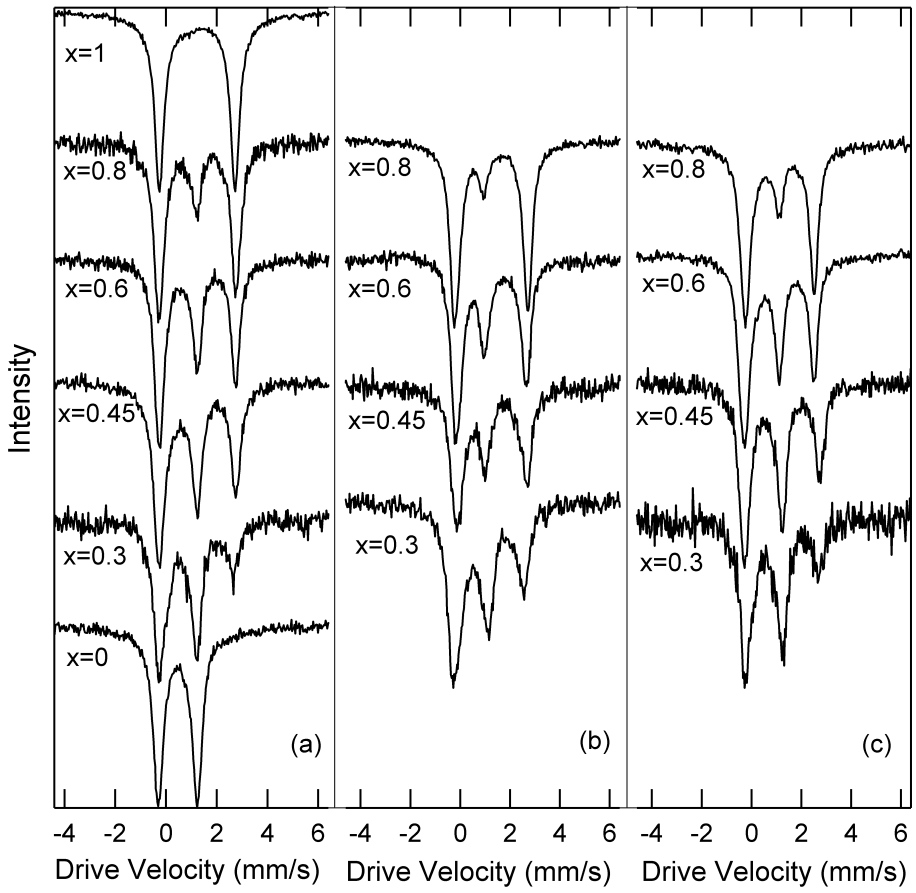

Figure 5.3: Mössbauer spectra of (a) triphylite (x=1), heterosite (x=0), and two-phase mixtures of x=0.8, 0.6, 0.45, and 0.3 at 25°C; (b) quenched solid solutions of x=0.8, 0.6, 0.45, and 0.3 at 25°C; (c) two-phase mixtures at 210°C

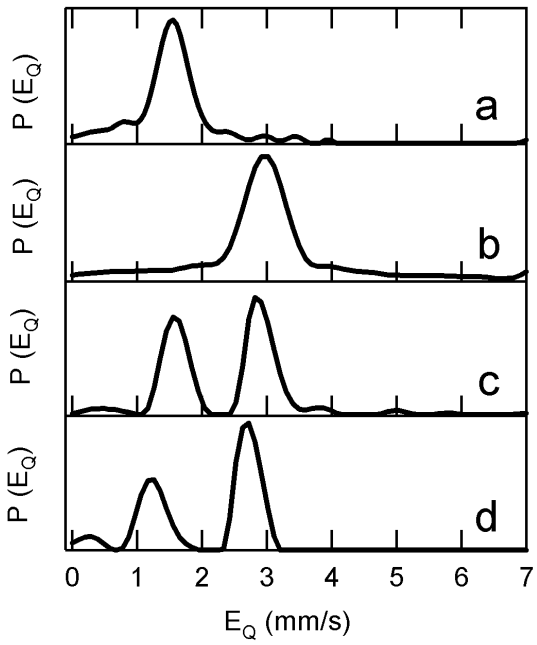

Figure 5.4: Quadrupole splitting distributions $P(E_Q)$ of (a) heterosite, (b) triphylite, (c) $Li_{0.6}FePO_4$ two-phase mixture, (d) $Li_{0.6}FePO_4$ solid solution at 25°C

temperatures, as shown in Fig. 5.3(c).

For quantitative analyses, the spectra were fitted and smoothed by calculating the correlation matrix between counts in each channel and the E_Q distribution with the software of Le Caër and Dubois [4]. Figure 5.6 shows the change of isomer shift with temperature. For each composition there are two values of IS, corresponding to the two doublets in the spectra. They approach each other as the temperature increases, indicating a rapid hopping of valence electrons between the Fe valence states. At higher temperatures these curves would be expected to merge, but structural changes in the materials caused us to stop data acquisition at 210°C.

Figure 5.7 shows the distribution of the electric quadrupole splitting (E_Q) at increasing temperature. For each composition the distribution decreases in velocity (energy) as the temperature increases from 25°C to 210°C. There is a distinct shift of the local maxima in the temperature ranges: 195°C–210°C for $x = 0.8$, 175°C–195°C for $x = 0.3$, 150°C–175°C for $x = 0.45$, and below 150°C for $x = 0.6$. This correlates with the change of E_{IS} values (Fig. 5.6), where E_{IS} of Fe^{2+} and Fe^{3+} have a monotonic increase or decrease with temperature, and a distinct temperature for the onset of the temperature range for changes in E_{IS} for each composition. The onset temperatures for the E_Q relaxations are lowest for Fe^{2+} and for the composition $x = 0.6$.

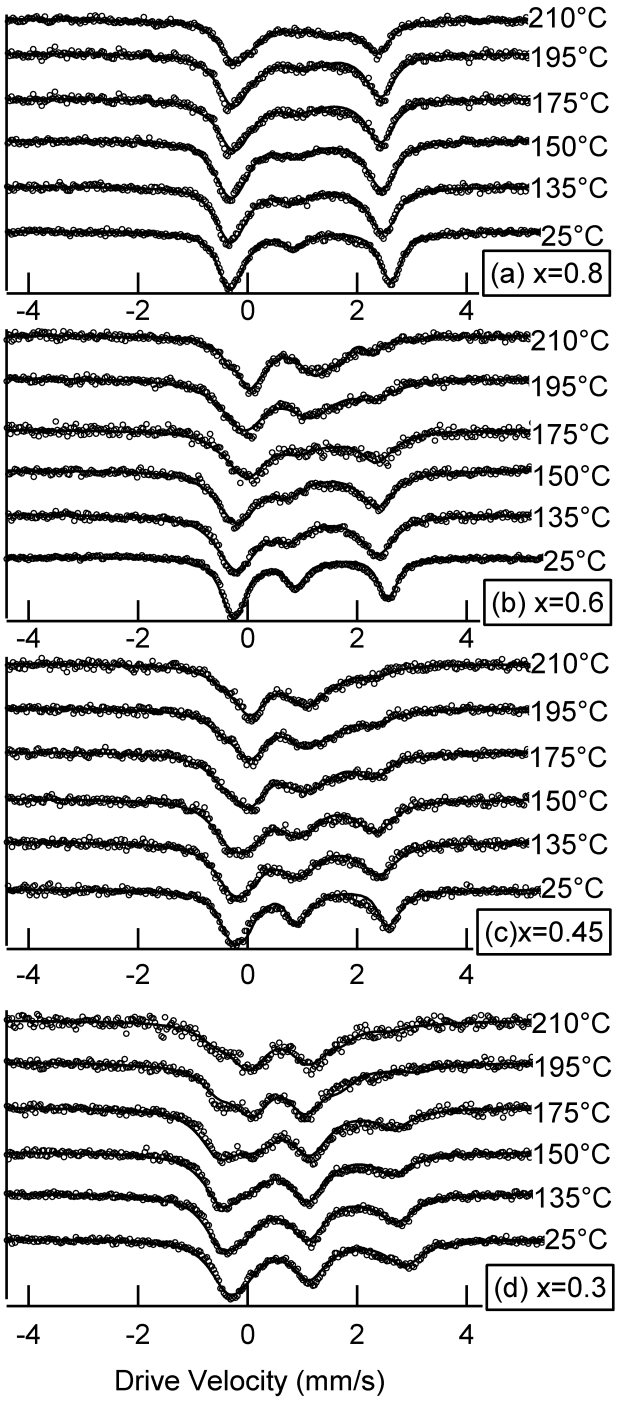

Figure 5.5: Mössbauer spectra of solid solutions at elevated temperatures for four compositions: $Li_{0.8}FePO_4$, $Li_{0.6}FePO_4$, $Li_{0.45}FePO_4$, $Li_{0.3}FePO_4$. All spectra were overlaid with fits from the method of Le Caër and Dubois [4].

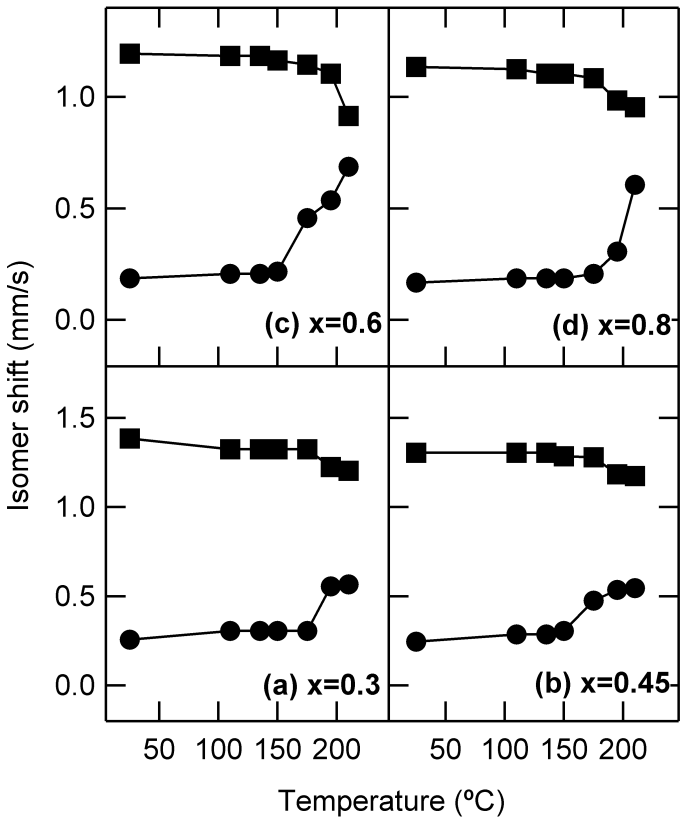

Figure 5.6: Change of isomer shift (mm/s) of Fe^{2+} (squares) and Fe^{3+} (circles) vs. temperature (°C) fitted from Mössbauer spectra in Fig. 5.5 for the four compositions: (a) x=0.3, (b) x=0.45, (c) x=0.6, and (d) x=0.8

Table 5.1: Activation energies and pre-factors of relaxation from change of isomer shift energies, $E_{\rm IS}$. $\Gamma_0 = 2 \times 10^{13}$ Hz

x	valence	ΔQ (meV)	valence	ΔQ (meV)
0.8	Fe^{2+}	546	Fe^{3+}	581
0.6	Fe^{2+}	560	Fe^{3+}	560
0.45	Fe^{2+}	554	Fe^{3+}	556
0.3	Fe^{2+}	543	Fe^{3+}	572
Avge	Fe^{2+}	(551 ± 7)	Fe^{3+}	(567 ± 10)

Table 5.2: Activation energies and pre-factors of relaxation from change of quadrupole splitting energies, $E_{\rm Q}$. $\Gamma_0 = 2 \times 10^{13}$ Hz

x	valence	ΔQ (meV)	valence	ΔQ (meV)
0.8	Fe^{2+}	532	Fe^{3+}	564
0.6	Fe^{2+}	511	Fe^{3+}	571
0.45	Fe^{2+}	510	Fe^{3+}	578
0.3	Fe^{2+}	497	Fe^{3+}	580
Avge	Fe^{2+}	(512 ± 12)	Fe^{3+}	(573 ± 6)

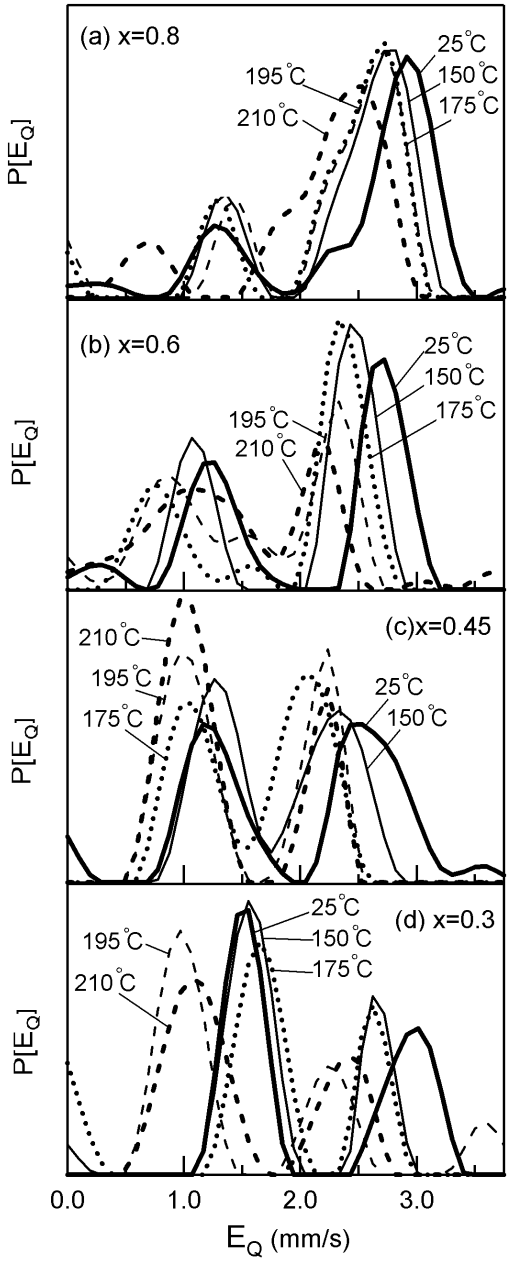

Figure 5.7: Electric quadrupole splitting distribution $P(E_Q)$ of Li_xFePO_4 solid solution vs. temperature, with (a) x=0.8, (b) x=0.6, (c) x=0.45, (d) x=0.3. Solid thick line: 25°C, thin solid line: 150°C, thick dotted line: 175°C, thin dashed line: 195°C, thick dashed line: 210°C. (Only distributions above 150°C are shown for clarity.)

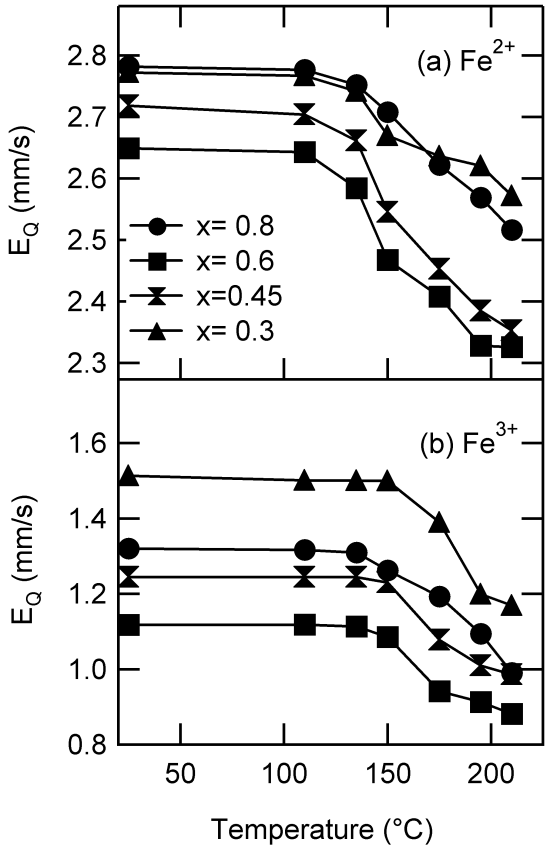

Figure 5.8: Values of quadrupole splitting E_Q obtained from 5.7. Parts (a) and (b) correspond to the Fe^{2+} and Fe^{3+} doublets, respectively, from the two peaks in the quadrupole splitting distribution of Fig. 5.7.

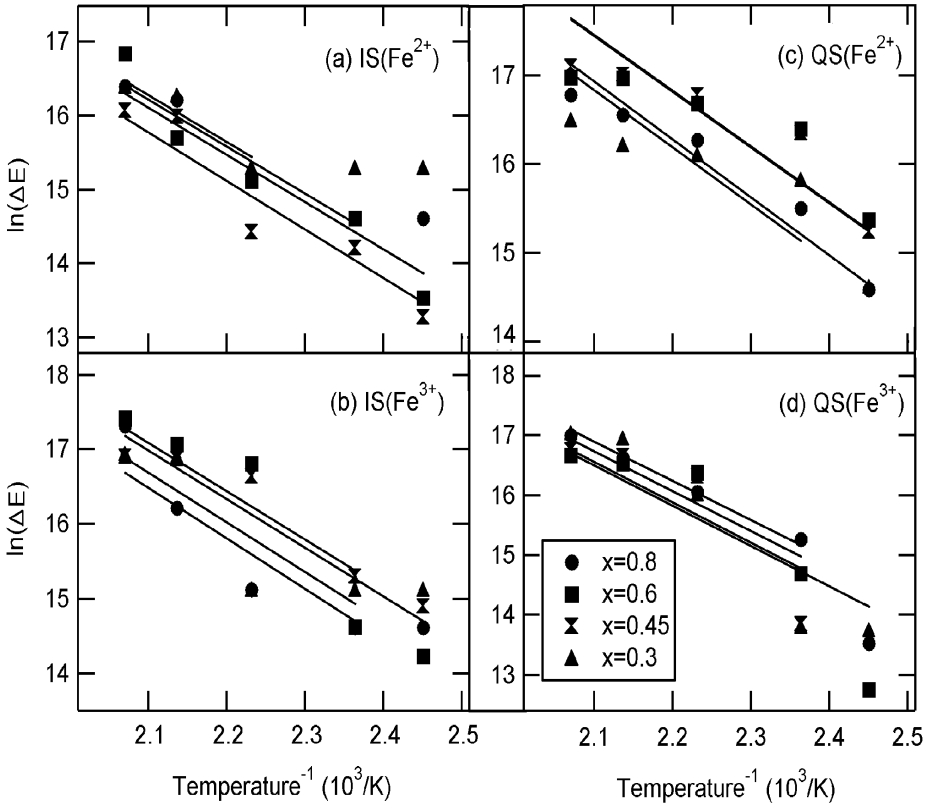

Figure 5.9: Arrhenius plot of $\ln[\Delta E_{\rm IS}(T)]$ and $\ln[\Delta E_{\rm Q}(T)]$ vs. $1/T$ $(10^3 K^{-1})$ using fitted $\rm E_{IS}$ and $\rm E_Q$ results of Fe^{2+} and Fe^{3+} from $\rm Li_xFePO_4$ solid solutions of four compositions. Activation energies are obtained from the fit lines.

5.4 Discussion

We define a frequency, Γ, in terms of the energy change measured with the isomer shift and EFG parameters of the Mössbauer spectra: $\Gamma_{\rm IS}(T) = \Delta E_{\rm IS}(T)/h$, and $\Gamma_{\rm Q}(T) = \Delta E_{\rm Q}(T)/h$. Figure 5.9 presents graphs of the temperature dependences of these parameters, useful for evaluating parameters of the Arrhenius relationship

$$\Gamma(T) = \Gamma_0 \exp(-\Delta Q/kT) \; . \tag{5.1}$$

Fits to these data were performed with both Γ_0 and ΔQ as free parameters, but Γ_0 showed variations over a wide range. Instead, for Table 5.1 and Table 5.2 we selected the intermediate value of $\Gamma_0 = 2 \times 10^{13}$, typical of phonon frequencies obtained from phonon DOS curve [122] and Raman spectra [131], which are the expected attempt frequencies for the polaronic charge hopping process. The activation energies ΔQ for the temperature-dependent $\rm E_{IS}$ and $\rm E_Q$ for Fe^{2+} and Fe^{3+} give four columns of data in Tables 5.1 and 5.2. The fitting was done at the higher temperatures where the $\rm E_{IS}$ and $\rm E_Q$ showed deviations from their low-temperature values, and it was this deviation that was used for the fit.

The composition dependences in Tables 5.1 and 5.2 are weak. The activation energies for the quadrupole splittings of Fe^{2+} show a monotonic change with x in Fig. 5.9. The composition dependence of the activation energy for Fe^{3+} is smaller and harder to measure. The variation for Fe^{2+} is larger and easier to measure, however. The activation energy for $\rm E_Q$ of Fe^{2+} may show a real compositional trend, with slower dynamics as x increases from 0.3 to 0.8.

Figure 5.8 shows that relaxations of $\rm E_Q$ for Fe^{2+} occur at relatively lower temperatures than the relaxations of $\rm E_{IS}$ shown in Fig. 5.6. It is curious that the activation energy of $\rm E_Q$ for Fe^{2+} is lower than the activation energy for $\rm E_{IS}$ of Fe^{2+} (Tables 5.1 and 5.2). The difference is significant experimentally, however, and is therefore important to consider in models of electronic processes. The activation energy for $\rm E_{IS}$ of Fe^{2+} may be lower than for Fe^{3+}, but the trend is not robust statistically. We expect that the activation energy for charge hopping should be the same for Fe^{2+} and Fe^{3+} because charge hopping involves both ions.

We suggest that there is an additional electronic process involving Fe^{2+} that contributes measurable fluctuations in its EFG. The simplest viewpoint is that this process is independent of the mechanism of charge hopping, so its fluctuations add to the fluctuations from charge hopping. This explanation adequately accounts for the trends in the experimental data — Fig. 5.8 shows that $\rm E_Q$ for Fe^{2+} begins to relax at a lower temperature than $\rm E_Q$ for Fe^{3+}. The $\rm E_Q$ for Fe^{2+} may be starting to reach a plateau for the intermediate composition $x = 0.6$ (and $x = 0.45$). The relaxations of $\rm E_{IS}$ for Fe^{2+} shown in Fig. 5.6 (top curves) are relatively small, and do not seem significantly different from those of $\rm E_{IS}$ for Fe^{3+}. Measuring an activation energy from these small changes is not reliable, so the accuracy is low for the activation energies of the isomer shift data in Table 5.1 for Fe^{2+}.

Nevertheless, the changes in E_Q for Fe^{2+} are large and easy to measure reliably, and the peak from Fe^{2+} in the plots of $P(E_Q)$ of Fig. 5.7 is seen to change at the lowest temperatures.

A physical process consistent with this simplest viewpoint of an additional electronic process is that the local environment of an Fe^{2+} ion is affected by the dynamics of a neighboring Li^+ ion. On the other hand, the Fe^{3+} ions are less affected because the Li^+ ions are not so often in their immediate vicinity. Evidently the Li^+ dynamics begin to cause fluctuations in E_Q for Fe^{2+} at lower temperatures than does the charge hopping processes, consistent with a picture where Li^+ ions shuttle between two sites that are both nearest-neighbors of an Fe^{2+} ion. Because the Li^+ ion does not leave the neighborhood of the Fe^{2+} ion, the isomer shift is not altered significantly, although the dynamical distortions of the environment may alter E_{IS} somewhat. The EFG is sensitive to the orientation of the charge distortion, which changes as the Li^+ shuttles between adjacent sites. A quantitative interpretation of the experimental data would require an advanced model [64], with parameters that probably cannot be determined uniquely with the present data. For example, it is not known how many Fe^{2+} ions are affected by the Li^+ dynamics, or how these effects extend to the higher temperatures where charge hopping becomes important.

We can, however, use this information on the relaxations of Fe^{3+} to gain understanding of the charge transfer process. The activation energies for E_{IS} and E_Q are very similar, suggesting that both originate from the charge transfer process. Averaging these activation energies for Fe^{3+} gives 570±9 meV. This is larger than the calculated activation energy for hopping of a simple polaron [74, 84], and suggests that charge transport in Li_xFePO_4 requires other activations. We suggest that the correlation to Li^+ ion dynamics is responsible for a larger activation energy. This does not necessarily mean that individual electrons and ions move together. In fact, if charge transfers occur between neighboring FeO_6 octahedra, the two are not in equivalent positions with respect to Li^+ sites on one a-plane (although there are equivalent sites on the next Li^+ layer). The three-dimensional configuration of Li^+ ions and vacancies allows some independence of electronic and ionic conductivity. It should also be mentioned that Mössbauer spectrometry is sensitive to averages of the residence times of Li^+ ions and Fe valence on the different crystallographic sites, so less-favorable configurations (i.e., Li^+ near Fe^{3+}) contribute less to the spectra even though such configurations could occur during thermal activation. In other words, a Li^+ ion may pass near Fe^{3+}, but if it passes quickly, the Fe^{3+} doublet in the spectrum will be little affected.

With the physical pictures above, we can use the Nernst-Einstein relation to convert the jump frequencies for charges and ions into electronic and ionic conductivity, respectively. Using the data of Tables 1 and 2 for Fe^{3+}, for all compositions we find an electrical conductivity 10^{-10} to 10^{-9} S/cm if we extrapolate the results to 25°C. As noted earlier, a faster jump frequency is found for the quadrupole splittings of Fe^{2+}. This implies a conductivity 10^{-8} to 10^{-9} S/cm if we extrapolate to 25°C. This does not correspond precisely to an ionic conductivity because the ionic motions that

alter the Fe^{2+} hyperfine parameters are not necessarily diffusive. Nevertheless, this discrepancy between conductivities for Fe^{2+} and Fe^{3+} does indicate that the intrinsic electronic mobility in Li_xFePO_4 is relatively low compared to the mobility of Li^+. The weak dependence on composition suggests that the rate capability of the solid solution phase of Li_xFePO_4 may be difficult to alter by chemical modifications.

In the $FePO_4$ – $LiFePO_4$ composition-temperature phase diagram, there is a eutectoid point around $x = 0.6$ and T=200°C [72, 3]. The present experimental work does not show any large fluctuations in the charge dynamics at the composition $x = 0.6$, suggesting that there is no large dynamical source of entropy that stabilizes the solid solution at this composition.

5.5 Conclusion

In the temperature range 25°C to 210°C, similar temperature dependences were observed in the Mössbauer spectra of four compositions of the solid solution phase of olivine Li_xFePO_4. Spectral contributions from Fe^{2+} and Fe^{3+} were separated, and it was found that the electric quadrupole splitting of Fe^{2+} showed dynamics at lower temperatures than for Fe^{3+}. Activation energies for the fluctuations of E_{IS} and E_Q for Fe^{3+} were similar, approximately 570 meV. For the Fe^{2+} components of the spectra, the fluctuations of E_Q occurred at lower temperatures than the fluctuations of the isomer shift (E_{IS}), with an activation energy of 512 meV for E_Q and of 551 meV for E_{IS}. The more facile fluctuations of E_Q for Fe^{2+} are evidence for fast motions of Li^+ ions that remain in the neighborhood of an Fe^{2+} ion. It appears that the intrinsic electronic mobility is lower than the mobility of Li^+.

Chapter 6

Rapid Electron Dynamics at Fe Atoms in Nanocrystalline $Li_{0.5}FePO_4$ Studied by Mössbauer Spectrometry

Two-phase mixtures of $Li_{0.5}FePO_4$ with crystal sizes as small as 25 nm were prepared by solid-state reaction, ball milling, and chemical delithiation. Mössbauer spectra of nanocrystalline $Li_{0.5}FePO_4$ found evidence for a thin layer of Fe^{3+} at crystal surfaces. Spectra acquired at temperatures from 25°C to 225°C showed thermally-driven electronic relaxations, where the electric field gradients (EFG) of the main Fe^{3+} and Fe^{2+} spectral components decreased with temperature. The isomer shifts (IS) of Fe^{3+} and Fe^{2+} showed similar thermal trends, indicative of valence fluctuations caused by small polaron hopping. The activation energies obtained from the temperature dependence of the EFG were 410 meV for Fe^{3+}, 330 meV for Fe^{2+}, and an activation energy of 400 meV was obtained for the IS of both. The rapid valence electron hopping between Fe sites is intrinsic to electronic conductivity in Li_xFePO_4, which is calculated to be higher than most reports for bulk material.

6.1 Introduction

Electrode materials for lithium-ion batteries require high ionic and electronic conductivities, high capacity, low cost, and environmental compatibility. The cathode material Li_xFePO_4 [70] meets many of these criteria, but it has the electronic structure of an insulator. The electrical conductivity of Li_xFePO_4 has been enhanced by carbon-coating [110, 132, 108, 133, 111], but there may be an additional improvement by preparing this material in nanocrystalline form. Several methods of nanocrystal synthesis have produced better electrochemical performance and faster charge conduction compared to large crystals of $LiFePO_4$ [99, 76, 79, 134, 80, 135, 77, 136, 137]. Recent experiments and simulations have addressed how nanocrystals of Li_xFePO_4 have altered kinetics

and thermodynamics [124, 125, 138, 123, 139, 140, 81, 137], but there have been few basic studies on electron mobility.

Small polaron hopping [141] is the likely mechanism for charge conduction in olivine Li_xFePO_4 [142, 91]. A small polaron includes the displacements of the positions of neighboring atoms when there is a change of valence at a central atom. For example, the Fe-O bond distance shortens by about 5% if an Fe^{2+} ion loses an electron to become an Fe^{3+}. Moving this electronic hole to an adjacent Fe site requires moving the local distortion too, often immobilizing the charge at low temperatures. The charge plus distorted environment, called a small polaron, moves at higher temperatures when atomic vibrations bring the local atomic structure of the adjacent site to a configuration compatible with bond distances and angles for Fe^{3+}. The electron then moves more rapidly than the ions. The thermally-activated polaron hopping frequency $f(T)$, as explained by Mott [141], is

$$f(T) = \nu \frac{e^2}{r} \frac{1}{k_B T} c(1-c) e^{-2\alpha r} e^{-Q/k_B T} \ , \tag{6.1}$$

which includes the frequencies, ν, of phonons that move adjacent Fe and O atoms, the concentrations of the Fe^{2+} and Fe^{3+}, c and $1-c$, an overlap of the adjacent Fe electron wavefunctions across the distance r, and an activation energy for achieving the conditions for polaron hopping, Q. For bulk $LiFePO_4$, an assessment of Q gave a value of approximately 650 meV [121]. Density functional theory calculations on free polaron motion gave a much lower value of 200 meV. However, since the polaron environment is likely affected by the presence of Li^+ ions, a higher activation energy is expected [91].

Mössbauer spectrometry gives a view of the electron density and electron dynamics from the perspective of nuclei of iron atoms. The static electron density was used to characterize the fractions of heterosite (Li-poor) and triphylite (Li-rich) phases in Li_xFePO_4 by Mössbauer spectrometry measurements on samples in an electrochemical cell [71]. Previous studies on Fe^{2+}/Fe^{3+} mixed-valence systems showed how the dynamics of thermally-activated charge transfers cause distortions of Mössbauer spectra [65, 128, 129]. More recently, small polaron hopping in Li_xFePO_4 was studied by measurements at elevated temperatures of Fe isomer shifts, IS, (characteristic of the charge density at ^{57}Fe nuclei) and electric quadrupole splittings, EQS, (characteristic of the electric field gradient, EFG, at ^{57}Fe nuclei) [90, 5, 2]. Especially at temperatures approaching 200°C, rapid valence fluctuations were seen clearly in the solid solution phase of Li_xFePO_4, although not in two-phase mixtures of the equilibrium heterosite and triphylite phases [5, 2]. These charge dynamics showed only a weak dependence on the concentration of Li, x, but the difference between activation energies for Fe^{2+} (approximately 510 meV) and Fe^{3+} (approximately 570 meV) suggests an additional electronic effect on Fe^{2+} caused by Li^+ ion motions [2].

The electronic quadrupole splitting is sensitive to the structural and electronic environment

of ^{57}Fe atoms, and when there are multiple environments in a sample, it is typical to observe a distribution of electric quadrupole splittings. An EQS distribution can be obtained by fitting the measured spectra to sums of doublets with various splitting centroid shifts (i.e., isomer shifts). We used the software package of Le Caër and Dubois [4] to analyze the spectra in this study. In the present study of nanocrystalline $Li_{0.5}FePO_4$ prepared as a mixture of heterosite and triphylite phases, the interpretation emphasized the effects of temperature on change dynamics, not local environments. Unlike Li_xFePO_4 with large crystals studied previously as a two-phase mixture of heterosite and triphylite [5, 2], thermal relaxations of the EQS and IS in nanocrystalline $Li_{0.5}FePO_4$ were observed at temperatures below 200°C. This indicates a much faster rate of small polaron hopping and electron dynamics in nanocrystalline material with similar phases. In addition, we report evidence that the nanocrystalline materials have an enrichment of Fe^{3+} at crystal surfaces.

6.2 Experimental

Nanocrystalline $LiFePO_4$ was prepared by a solid-state reaction with precursors of $Fe(C_2O_4)\cdot 2H_2O$, $NH_4H_2PO_4$, and Li_2CO_3, followed by milling in a Fritsch planetary ball mill, as described previously [1]. The $LiFePO_4$ crystal size was controlled by varying the ball-to-powder weight ratio and milling time. The two-phase mixture of nano-$Li_{0.5}FePO_4$ was prepared by chemically oxidizing Fe^{2+} in an acetonitrile solution with NO_2BF_4. A PANalytical X'pert PRO X-ray diffractometer (XRD) with Cu Kα radiation, a ZEISS 1550 VP field-emission scanning electron microscope (FE-SEM), and a Tecnai F30 transmission electron microscope (TEM) were used to determine crystal sizes, microstructure, and phase fractions.

Mössbauer spectrometry was performed in transmission geometry, with a ^{57}Co in Rh source mounted on a Wissel MVT1000 Doppler drive unit. Data acquisition and synchronization were controlled by a LabVIEW system with a buffered counter. Velocity calibration of the spectrometer was referenced to room-temperature α-Fe spectra. For in situ measurements, samples were heated in an electrical resistance furnace at fixed temperatures, monitored by a few thermocouples. Spectra were acquired for 12 hours after 1 hour of equilibration at each temperature. After cooling back to room temperature, the samples were checked again by XRD and Mössbauer spectrometry to determine phase fractions. Distributions of electric quadrupole splitting energies (E_Q) were analyzed by the method of Le Caër and Dubois [4] using a linear correlation between isomer shift and quadrupole splitting for each valence.

6.3 Results

The as-prepared $LiFePO_4$ (bulk-$LiFePO_4$) was confirmed by XRD to have the olivine structure with a large crystal size, consistent with the 300 nm estimated from SEM and TEM. Using the Hall-Williamson method to interpret the X-ray line broadening [104], the ball-milled nanocrystalline $LiFePO_4$ had a characteristic crystal size of 25 nm. The SEM and TEM images showed an aggregation of the nanocrystals into secondary particles of 0.5–1 μm (Fig. 6.1).

Figure 6.2 shows Mössbauer spectra measured at room temperature on 25 nm Li_xFePO_4 two-phase mixtures, with $x = 0.65$, 0.5, and 0.35. The two different valences, Fe^{3+} and Fe^{2+}, characteristic of heterosite and triphylite, respectively, show distinct electric quadrupole splittings (EQS) and isomer shifts (IS). Consistent with previous work [2] on 300 nm bulk-Li_xFePO_4, spectra of the two-phase mixtures are approximately linear combinations of the two doublets of Fe^{3+} and Fe^{2+}.

For the 25 nm nanocrystalline Li_xFePO_4 (x=0.65, 0.5, and 0.35), two maxima from Fe^{3+} and Fe^{2+} are prominent in distributions of the electric quadrupole splitting energies, $P(E_Q)$ (Peak 1 and Peak 2 in Fig. 6.3). The areal fractions of Fe^{3+} and Fe^{2+}, integrated from $P(E_Q)$ in Fig. 6.3, are consistent with their molar concentrations from Rietveld refinement of XRD patterns. Although XRD shows only two phases of triphylite and heterosite in the three samples, there is an extra intensity observable around 0.8 mm/s, Peak 0 in Fig. 6.3, indicating another local configuration of Fe. For the different crystal sizes of 300 nm, 70 nm, and 25 nm, the areal fraction of Peak 0 is approximately linear with the inverse of crystal size (Fig. 6.4), but independent of composition. Such a scaling is consistent with the presence of Fe^{3+} at crystal surfaces, which may be too thin or too disordered to give a signature pattern in XRD.

Figure 6.5 shows Mössbauer spectra of 25 nm $Li_{0.5}FePO_4$, measured at temperatures from 25°C to 210°C. Upon heating, a gradual decrease of the EQS is visible in the spectra, starting around 145°C. For samples with larger crystals, this change of Mössbauer lineshapes with temperature was not observed for two-phase Li_xFePO_4 at any composition x, although the solid solution phase of Li_xFePO_4 shows similar behavior at slightly higher temperatures [2].

Figure 6.6 presents distributions of electric quadrupole splitting energies, E_Q, fitted from the data of Fig. 6.5 with the method of Le Caër and Dubois. As in the study of bulk crystalline Li_xFePO_4 by Mössbauer spectrometry using Le Caër's method [2], peaks 1 and 2 correspond to Fe^{3+} and Fe^{2+}, respectively. Although these two peaks change shape at temperatures above 145°C, the ratio of their areas is approximately one from 25°C to 200°C, as expected for a two-phase mixture with a composition of $x = 0.5$. The areal fraction and center of Peak 0 ($E_Q \simeq 0.7$ mm/s) for surface Fe^{3+} stays almost constant with temperature from 25°C to 200°C. This lack of temperature sensitivity is consistent with the observation that the crystallite size determined by XRD did not change after heating the sample in this temperature range.

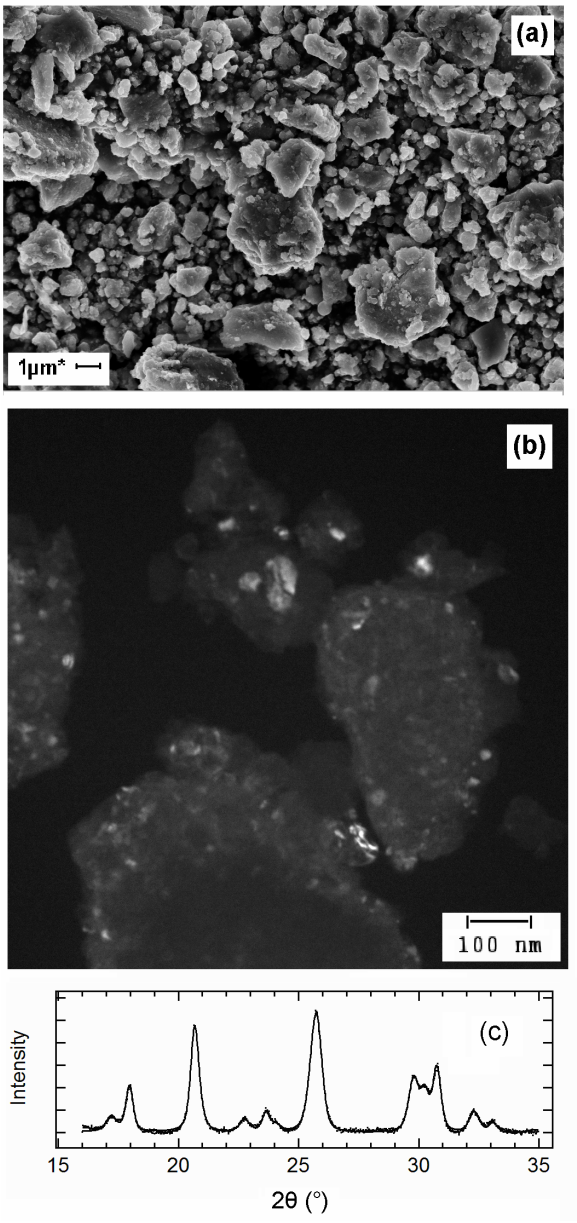

Figure 6.1: (a) SEM image of 25 nm $Li_{0.5}FePO_4$ showing agglomeration into larger secondary particles. (b) TEM dark-field (DF) image of 25 nm $Li_{0.5}FePO_4$ showing internal crystal sizes in the range of 20–30 nm. (c) XRD of 25 nm $Li_{0.5}FePO_4$, obtained with Cu Kα radiation

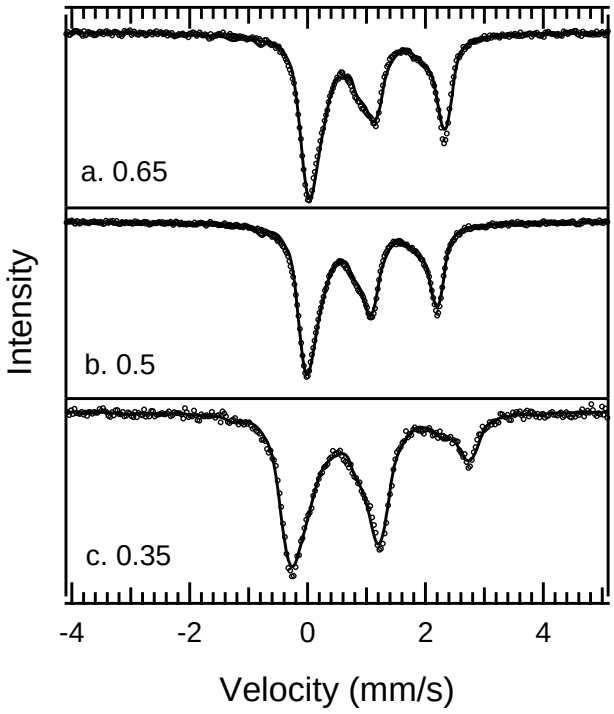

Figure 6.2: Room-temperature Mössbauer spectra of two-phase mixtures of heterosite and triphylite in materials with 25 nm crystallites. (a) $Li_{0.65}FePO_4$, (b) $Li_{0.5}FePO_4$, and (c) $Li_{0.35}FePO_4$

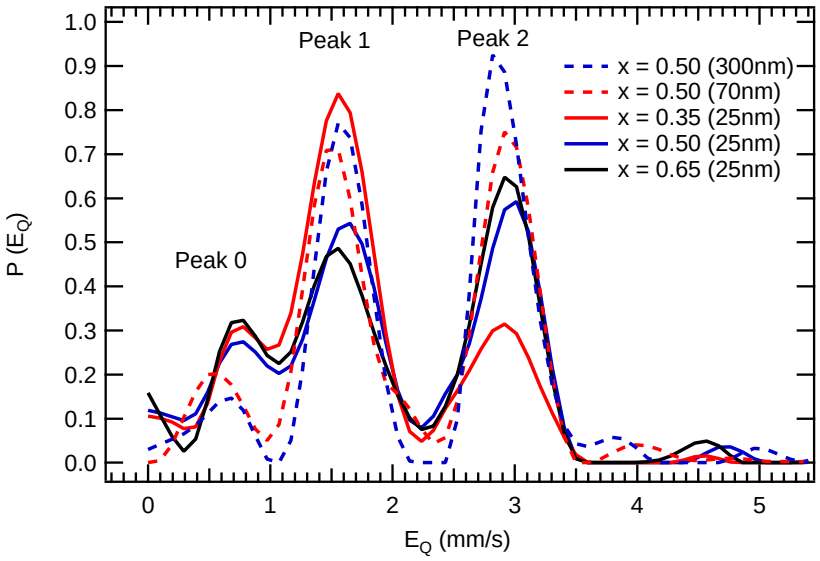

Figure 6.3: Electric quadrupole splitting distribution $P(E_Q)$ of Li_xFePO_4 with different crystal sizes, from spectra of Fig. 6.2

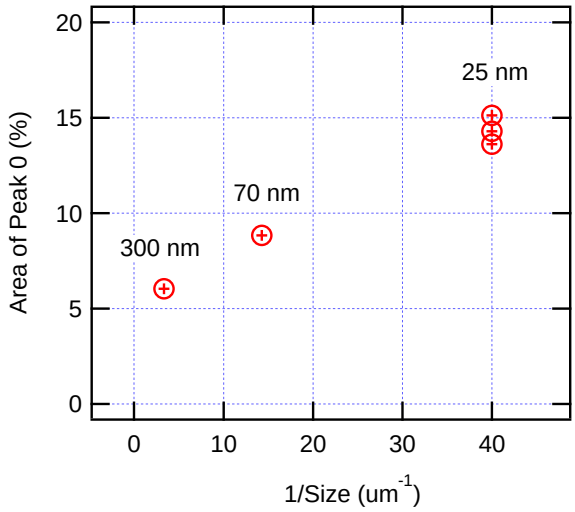

Figure 6.4: Areal fraction of Peak 0 with different crystal sizes, obtained by integrating the intensity below 1 mm/s in Fig. 6.3

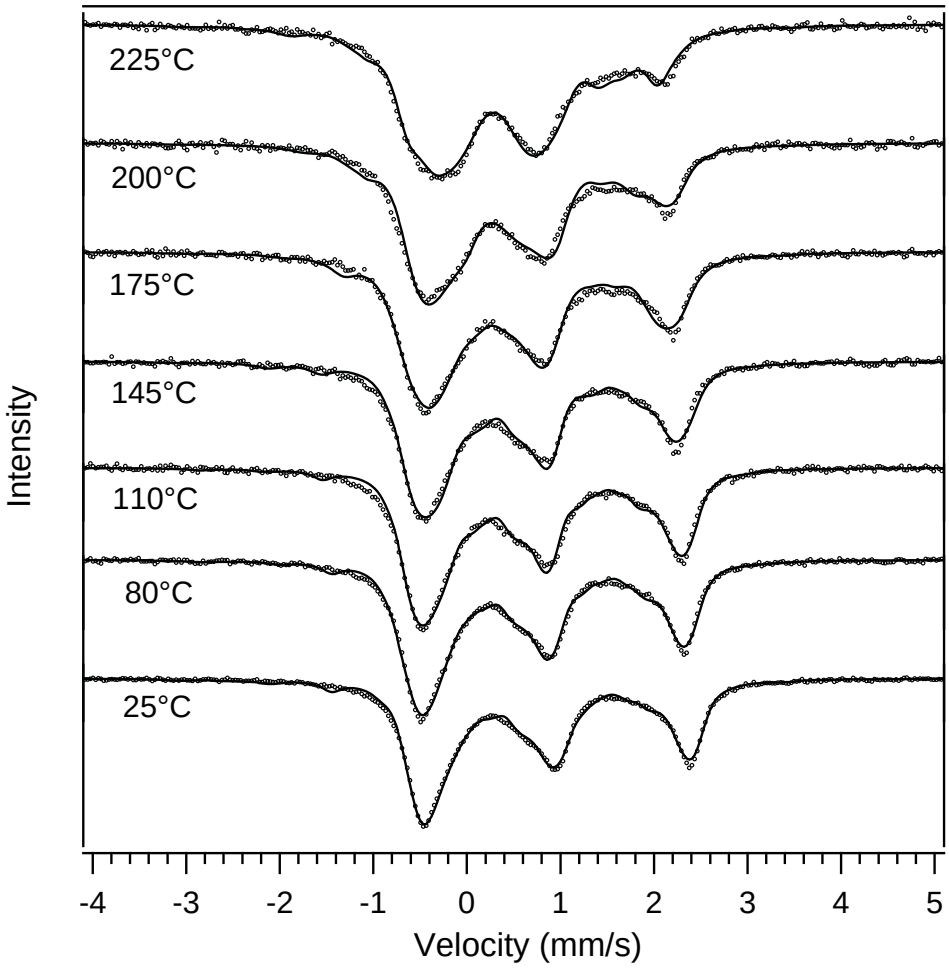

Figure 6.5: Mössbauer spectra of 25 nm $Li_{0.5}FePO_4$ at elevated temperatures. Solid lines show fits from the hyperfine field distribution obtained by the method of Le Cäer and Dubois [4].

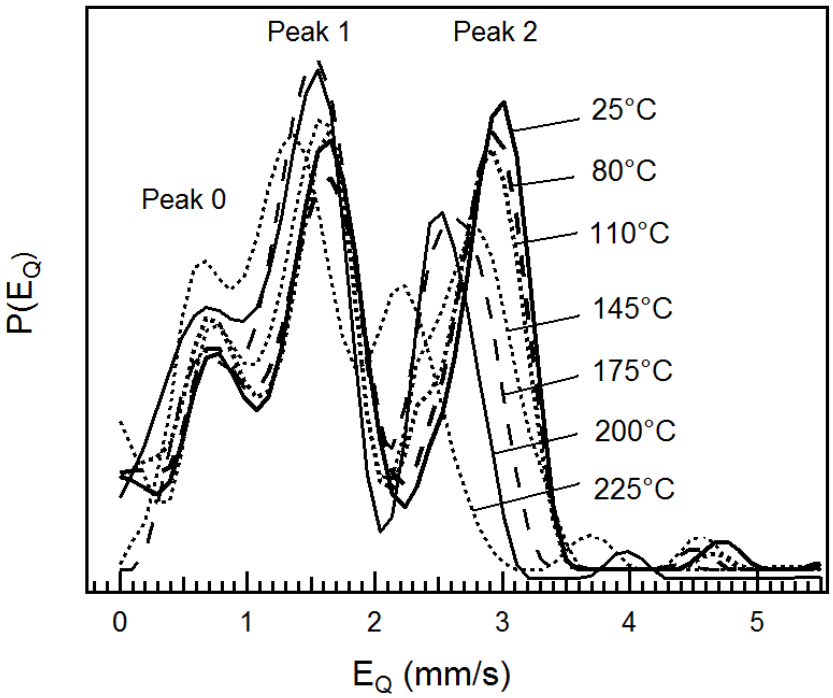

Figure 6.6: Electric quadrupole splitting distribution $P(E_Q)$ of 25 nm $Li_{0.5}FePO_4$ vs. temperature, obtained from the spectra of Fig. 6.5

Figure 6.6 shows that the two major peaks shift to smaller E_Q with increased temperature, particularly Peak 2 for Fe^{2+}. These two peaks were fit to two Gaussian functions to obtain averaged values of E_Q for Fe^{2+} and Fe^{3+} at each temperature, and results are shown in Fig. 6.7. The difference between the E_Q measured at elevated temperatures and at room-temperature, ΔE_Q, is graphed vs. $1/T$ in Fig. 6.9. The Arrhenius behavior gives an activation energy for Fe^{3+} of 410 meV, which is larger than the 330 meV obtained for Fe^{2+}.

The isomer shifts (IS) were in the range of 1.0 to 1.4 mm/s for Fe^{2+}, and in the range of 0.4 to 0.8 mm/s for Fe^{3+} (Fig. 6.8). These are typical of high-spin configurations for both valences of Fe ($S = 2$ for Fe^{2+} and $S = 5/2$ for Fe^{3+}). At higher temperatures the IS of Fe^{2+} decreased, but it increased for Fe^{3+}, so the isomer shifts became more similar. The formation of the solid solution phase stopped us from acquiring data above 230°C, limiting the upper range of Fig. 6.8. The isomer shifts for bulk $Li_{0.6}FePO_4$, on the other hand, are independent of temperature. The Arrhenius behavior of the isomer shifts (Fig. 6.10) gave activation energies of 400 and 420 meV, essentially the same, for Fe^{2+} and Fe^{3+}. By fitting directly the plot of ΔE_{IS} versus $1/T$ in Fig. 6.8, the activation energies for the isomer shift dynamics of both Fe^{2+} and Fe^{3+} were about 400 meV with a prefactor of 1.0×10^{11} Hz.

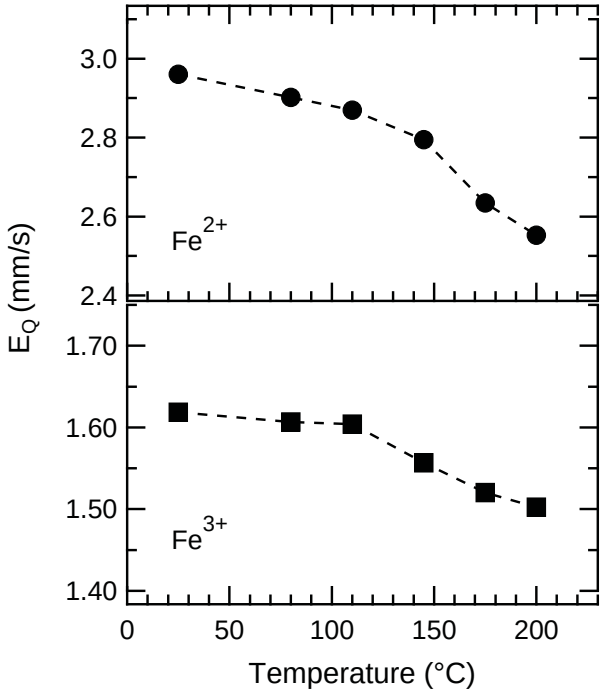

Figure 6.7: Values of electric quadrupole splitting energy E_Q (mm/s) obtained from Fig. 6.6, corresponding to Fe^{2+} and Fe^{3+}

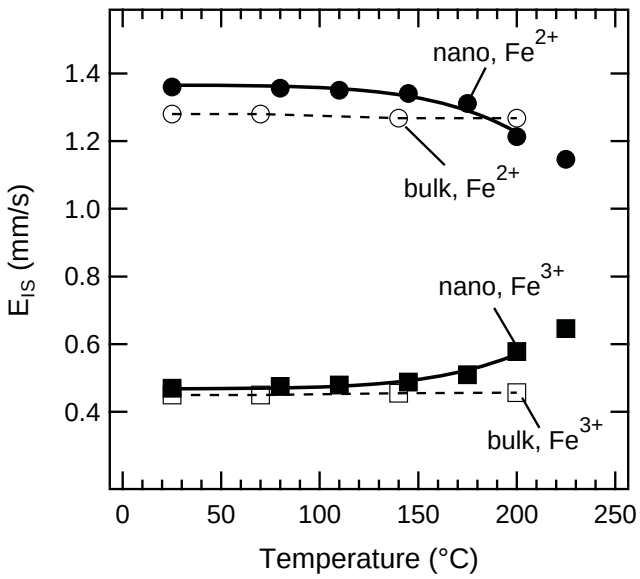

Figure 6.8: Values of isomer shift energy E_{IS} (mm/s) of Fe^{2+} and Fe^{3+} vs. temperature, from fitting Mössbauer spectra of Fig. 6.5, plotted together with E_{IS} of Fe^{3+} and Fe^{2+} in the bulk $Li_{0.6}FePO_4$ [5]. The effect from the second-order Doppler shift was subtracted. Solid lines show fitting of Arrhenius relation between IS and temperature, with an activation energy of about 400 meV and prefactor of 1.0×10^{11} Hz.

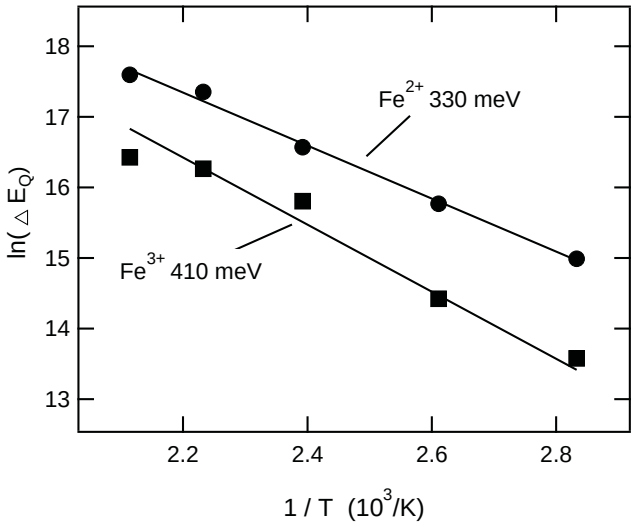

Figure 6.9: Arrhenius plot of $\ln(\Delta E_Q)$ vs. $1/T$ for Fe^{3+} and Fe^{2+}. Activation energies for EFG were obtained from the lines between 80°C and 200°C.

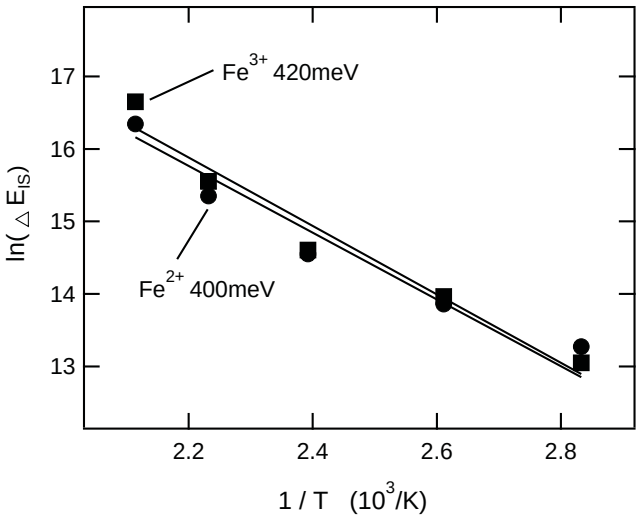

Figure 6.10: Arrhenius plot of $\ln(\Delta E_{IS})$ vs. $1/T$ for Fe^{3+} and Fe^{2+}. Activation energies for isomer shifts were obtained from the lines between 80°C and 200°C.

6.4 Discussion

Mössbauer spectrometry has a characteristic measurement time of $\tau = h/\varepsilon$, where ε is the energy width of the nuclear resonance line, or the hyperfine interaction energy that gives rise to the EQS or IS (for ^{57}Fe, $\varepsilon = (v/c)\,14.41\,\text{keV}$, where v is the Doppler velocity and c is the speed of light). Values of τ from several ns to 100 ns give measurable effects in Mössbauer spectra, and we use this feature to study thermal fluctuations of charge dynamics in Li_xFePO_4.

If electrons are thermally excited to a higher energy level on a ^{57}Fe atom, a widely-used theory of Ingalls [143] predicts a change in EFG from the anisotropy of the $3d$-orbital charge distribution of Fe^{2+}. A high-spin configuration of Fe^{2+} may have each of its first five $3d$ electrons occupying one d-orbital, giving a spherical shell and no variation of EFG, but the sixth $3d$ electron has probability of occupying different orbitals, causing an EFG. With thermal energy, this sixth valence electron changes between these levels, and the charge distribution of Fe^{2+} appears more isotropic on the time scale of the Mössbauer effect, reducing the EFG. Ingalls theory predicts no such effect on the EFG for Fe^{3+}, which has one electron in each $3d$ orbital. Nevertheless, we do observe a thermal reduction in EFG for Fe^{3+}. Furthermore, we also see a change in the IS, indicating fluctuations of charge at ^{57}Fe atoms [2, 5]. For these two reasons, we discount the Ingalls theory for the main effects observed for Li_xFePO_4.

Thermal fluctuations of both the EQS and IS with increased temperatures are consistent with electrons hopping between FeO_6 octahedra, switching them between Fe^{2+} and Fe^{3+} configurations. Several previous studies reported this behavior in mixed-valence materials [144, 65, 128, 129]. At low temperatures, Fe valence electrons move infrequently between two corner-shared FeO_6 octahedra, and the Mössbauer spectra sample a static charge configuration when the electron dwell time is longer than the 100 ns lifetime of the ^{57}Fe nuclear excited state. The electron dynamics are faster at higher temperatures, and when valence electrons move between iron ions more frequently than 100 ns, the EFG is reduced because the ion appears more symmetrical on the time scale of the measurement. Likewise, the IS does not distinguish so clearly the Fe^{3+} and Fe^{2+} valences when charge is hopping rapidly. (In the high-temperature limit, not achieved in this investigation, Fe^{3+} and Fe^{2+} become indistinguishable by Mössbauer spectrometry.)

Our previous work on two-phase mixtures of Li_xFePO_4 with larger crystals and compositions $x =$ 0.8, 0.6, 0.45, and 0.3 showed little temperature dependence of the spectra in the temperature range from 25°C to 210°C [5, 2]. For the nanocrystalline materials of the present study, the temperature variation of the EFG was big enough to determine activation energies for Fe^{3+} of 410 meV, and Fe^{2+} of 330 meV. These are smaller than for bulk materials prepared as solid solutions [2], where similar analysis gave activation energies for Fe^{3+} of 570 meV and Fe^{2+} of 510 meV. From previous measurements of electrical conductivity or AC impedance spectroscopy, the reported activation

energies for electron mobility in $LiFePO_4$ varied over a wide range from 150 meV to 750 meV [116, 117, 115, 119, 121, 89].

The dynamics of the thermally-activated IS fluctuations originate with small polaron hopping, and give detailed information about charge mobility. For a prefactor of 1.0×10^{11}, obtained from constants in Eq. 6.1, and an activation of 400 meV, we obtain hopping frequencies at 25°C of about 2.8×10^7 Hz. Using the Nernst-Einstein relation, the polaron hopping rate can be converted to electrical conductivity, giving 1.4×10^{-7} S/cm at 25°C.

We find a lower activation energy for the EQS broadening for Fe^{2+} than Fe^{3+}, 330 vs. 410 meV. The activation energy for the EQS of Fe^{3+} is essentially the same as for the isomer shift, consistent with a common origin in small polaron hopping. The Ingalls explanation would perhaps lower the activation energy for the EQS of Fe^{2+}, but we suggest this lower activation energy may originate with neighboring Li^+ ions or vacancies. This coupling was suggested in previous work [91, 90] as an extra binding energy barrier added to free polarons, but discounted by others [121]. If a Li^+ ion were in a static position near one of the two Fe sites of the polaron hop, it should bias the nearby Fe towards Fe^{2+}, making a higher barrier for the electron to leave this site than to return. Although this site may spend more time as Fe^{2+} than Fe^{3+}, the other Fe site has the opposite trend, so Mössbauer spectrometry cannot detect a difference in the fluctuation times of Fe^{2+} and Fe^{3+}. On the other hand, if the Li^+ ions were performing diffusional jumps at rates comparable or faster than the polarons, it is possible that Mössbauer spectrometry could detect a difference in the fluctuations of the EFG at Fe^{2+} and Fe^{3+}. The effects are expected to be larger at Fe^{2+} ions, which are more likely to have Li^+ ions in their vicinity, so a lower activation energy for the EQS at Fe^{2+} seems reasonable [2].

With decreasing crystallite size, Li_xFePO_4 will have more crystal surfaces, and perhaps more grain boundaries and interfaces between heterosite and triphylite phases. Approximately, reducing the average crystal size from 300 nm to 25 nm could create 12 times more interface area. Mössbauer spectrometry shows a spectral component of small EQS that likely originates with Fe^{3+} ions at crystal surfaces. The fraction of Peak 0 in the spectrum (Fig. 6.3) increases from 6 to 14% when the crystal size decreases from 300 nm to 25 nm, approximately consistent with an increase of Fe^{3+} on the surface layer over a characteristic thickness of one unit cell. There has been much interest in the thermodynamics of surfaces for nanoparticles of Li_xFePO_4 [79, 139, 145, 125]. A shell at the crystal surface enriched in Fe^{3+} and having an altered structure could play a role in the kinetics of lithiation. This shell may also affect the stability of the crystal against transformation to another phase. Surface effects were suggested as a possible reason for the kinetic stability of the solid solution phase of nanocrystalline Li_xFePO_4 at low temperatures [81].

6.5 Conclusion

Nanocrystalline $Li_{0.5}FePO_4$ powders were synthesized by solid-state reaction followed by ball milling. X-ray diffractometry showed them to be two-phase mixtures of Li-rich triphylite and Li-poor heterosite with characteristic crystal sizes as small as 25 nm. Mössbauer spectrometry showed a spectral component from Fe^{3+} that increased with the inverse of crystallite size, correlating to the amount of crystal surface. Mössbauer spectrometry also showed a decrease with temperature of the electric field gradients (EFG) at $^{57}Fe^{3+}$ and $^{57}Fe^{2+}$ nuclei in nanocrystalline $Li_{0.5}FePO_4$, a behavior not seen in two-phase materials with larger crystal sizes. The isomer shifts of Fe^{3+} and Fe^{2+} showed a similarly anomalous temperature dependence, merging together with temperature as is characteristic of valence fluctuations, owing to small polaron hopping between FeO_6 octahedra. Both isomer shift and electric quadrupole effects indicate a fluctuation time of order 10 ns at a temperature of order 200°C. The activation energies for the IS fluctuations were approximately 400 meV, and the activation energies for the EFG fluctuations were 410 meV for Fe^{3+} and 330 meV for Fe^{2+}. The activation energies are lower in these 25 nm nanocrystalline materials than reported for comparable two-phase bulk materials, indicating a higher intrinsic electrical conductivity.

Chapter 7

Thermodynamic and Kinetic Stability of the Solid Solution Phase in Nanocrystalline Li_xFePO_4

Samples of nanostructured Li_xFePO_4 with characteristic crystal sizes of 26 nm, and compositions of x=0.35 and 0.65, were synthesized by ball-milling and chemical delithiation. X-ray powder diffraction showed that the solid solution phase with x=0.65 started to form when heated above 200°C. The solid solution phase of nanocrystalline $Li_{0.65}FePO_4$ was quick to form above 200°C, but did not unmix at lower temperatures. Unmixing below 200°C was found after long-time annealing of nanocrystalline $Li_{0.35}FePO_4$, however, consistent with the equilibrium phase diagram of bulk Li_xFePO_4. The stability of the solid solution of nanocrystalline Li_xFePO_4 is kinetic in origin, perhaps originating with effects of crystal surfaces.

7.1 Introduction

Olivine-structured $LiFePO_4$ has been studied extensively since it was first reported as a promising cathode material for rechargeable Li batteries [70]. In battery applications, the fractions of $LiFePO_4$(triphylite) and $FePO_4$(heterosite) are changed during lithium insertion and extraction. At high temperatures above 200°C, there is a phase transformation in the Li_xFePO_4 binary system from a two-phase mixture of triphylite and heterosite to a single solid solution phase of the same olivine structure, with lithium ions randomly occupying Li sites [72]. The phase diagram was assessed both experimentally and theoretically [3, 74]. In related work, phase boundaries of the unmixed phases at room temperature were determined [73]. A transmission electron microscopy (TEM) and in situ X-ray diffractometry (XRD) study suggested a metastable Li_xFePO_4 phase appeared during heating and cooling [86]. The Li_xFePO_4 two-phase mixtures and solid solutions were also investigated by Mössbauer spectrometry to evaluate activation energies of Fe^{2+}/Fe^{3+} valence fluctuations, evidently coupled to Li^+ ionic mobility [90, 5, 2].

More recently, nanocrystalline $LiFePO_4$ has attracted much attention. Nanostructured $LiFePO_4$ can be synthesized in various ways [99, 146, 79, 76, 147]. The phase boundary at room temperature was reported to change with decreasing crystal size, as indicated by electrochemical cycling and synchrotron XRD [78, 80]. On the surfaces of 40 nm, carbon-free $LiFePO_4$ crystals produced by jet-milling, a thin amorphous layer was reported to help stabilize the solid solution inside [134]. A thermodynamic assessment suggested that the surface energy of nanocrystals stabilizes the disordered phase [139].

In this work, we tested the stability of nanocrystalline solid solutions and two-phase mixtures of Li_xFePO_4 ($x = 0.35$ and 0.65) at various temperatures. Compared to Li_xFePO_4 with large crystals, the unmixing transformation is slower in the nanocrystalline material, making thermodynamic equilibrium more difficult to achieve. Nevertheless, results from $Li_{0.65}FePO_4$ suggest, and results from $Li_{0.35}FePO_4$ show, that the equilibrium temperature for the unmixing transformation is similar in bulk and nanocrystalline materials.

7.2 Experimental

The $LiFePO_4$ material was prepared by a solid-state reaction with precursors of $Fe(C_2O_4)2H_2O$, $NH_4H_2PO_4$, and Li_2CO_3 in a molar ratio (1:1:0.5) as described previously [1]. These bulk-$LiFePO_4$ powders were then ball-milled for 2 hours at 400 rpm in Ar atmosphere to prepare samples of nano-$LiFePO_4$. The two-phase mixture bulk-$Li_{0.65}FePO_4$, nano-$Li_{0.65}FePO_4$, and nano-$Li_{0.35}FePO_4$ were obtained by chemical delithiation using $K_2S_2O_8$ as an oxidant [3]. Heat treatments of all two-phase mixtures were done by heating samples in vacuum-sealed glass ampoules at proposed temperatures. Heat treatment to form the solid solution was achieved by heating the two-phase mixtures in vacuum-sealed glass ampoules at 380°C for 12 hours, followed by annealing at intended temperatures.

X-ray diffraction (XRD) patterns were collected for all samples with a PANalytical X'pert PRO X'Celerator diffractometer using Cu Kα radiation. All XRD measurements were taken in the 2θ range 15°–35°, with a slow scanning rate of step size 0.002653°/s. A high-temperature stage with a furnace was used with flowing ultra-pure N_2 for in situ high temperature (HT) XRD measurements. The heating and cooling rates of the furnace were 5°C per minute, and the temperature was held for 1 hour at each step before each measurement.

Bright-field (BF) and dark-field (DF) transmission electron microscopy (TEM) images were taken with Philips EM420 and Tecnai F30 instruments, operating at 120 kV and 300 kV, respectively. Samples were gently ground and dispersed in isopropyl solvent before being transferred to 3 mm copper grids. Ultrasonic vibration was also used to decrease agglomeration.

Mössbauer spectrometry was performed at room temperature with a conventional constant acceleration system with ^{57}Co (in Rh) γ-ray source. Velocity and isomer shift calibrations were performed

with reference to room-temperature α-Fe spectrum. Distributions of electric quadrupole splitting (E_Q) were analyzed by the method of Le Caër and Dubois [4], using a linear correlation between isomer shift and quadrupole splitting.

7.3 Results and discussion

The XRD patterns of bulk-$LiFePO_4$ and nano-$LiFePO_4$ are shown in Fig. 7.1(a) and (b). The XRD pattern of nano-$LiFePO_4$ shows significant peak broadening in Fig. 7.1(b), and analysis with the Scherrer equation gave a crystal size of 26 nm. After eliminating instrumental contribution, broadening of XRD peaks has weak dependence on $\sin\theta$, so the broadening is mostly from the crystal size effect. By comparing the integrated areas of peaks and backgrounds in the XRD patterns of bulk-$LiFePO_4$ and nano-$LiFePO_4$, we find the nano-$LiFePO_4$ to be composed of at least 90% crystalline material.

Mössbauer spectra (Fig. 7.1(c)) and electric quadrupole splitting distributions (Fig. 7.1(d)) of both bulk-$LiFePO_4$ and nano-$LiFePO_4$ verified that our nano-$LiFePO_4$ obtained after ball milling was not contaminated by iron from the milling process. Furthermore, the spectrum from nano-$LiFePO_4$ was acquired after air exposure for 1 month. Perhaps owing to agglomeration, there is little oxidation of the Fe^{2+}, similar to the bulk material. The surface areas measured by the BET method were 6.6 m^2/g and 4.7 m^2/g for the bulk and nanocrystalline material, respectively, so the particles of agglomerated nanocrystallites actually had less surface exposed to air.

Figure 7.2 shows BF and DF TEM images of bulk-$LiFePO_4$ and nano-$LiFePO_4$. The crystals are agglomerated, but the crystal sizes are consistent with the XRD results of 26 nm for the nano-$LiFePO_4$ and 330 nm for bulk-$LiFePO_4$.

Results from in situ XRD at elevated temperatures are shown in Fig. 7.3(a)–(d) for bulk-$Li_{0.65}FePO_4$ and nano-$Li_{0.65}FePO_4$. The measurements of Fig. 7.3(a)–(d) started with two-phase mixtures, identifiable by the two (200) peaks at approximately 2θ=17.2° and 18.0°, for example. The series of patterns on the left show that upon heating the solid solution appears around 210°C, and above 330°C this phase is formed completely. Upon cooling, Fig. 7.3(b) shows that the two-phase mixture becomes visible below 210°C. When cooled to room temperature, there is a coexistence of the heterosite, triphylite, and solid solution phases. The XRD patterns obtained during heating and cooling of bulk-$Li_{0.65}FePO_4$ (Fig. 7.3(a) and 7.3(b)) are consistent with previous results [72, 3]. The heating trend is similar for nano-$Li_{0.65}FePO_4$ but the cooling trend is quite different (Fig. 7.3(c) and 7.3(d)). Figure 7.3(c) shows that during heating of nano-$Li_{0.65}FePO_4$, the phase transformation to the solid solution phase begins around 210°C and is complete above 290°C–similar to the results for bulk-$Li_{0.65}FePO_4$. During cooling, however, the solid solution phase persists down to room temperature (Fig. 7.3(d)).

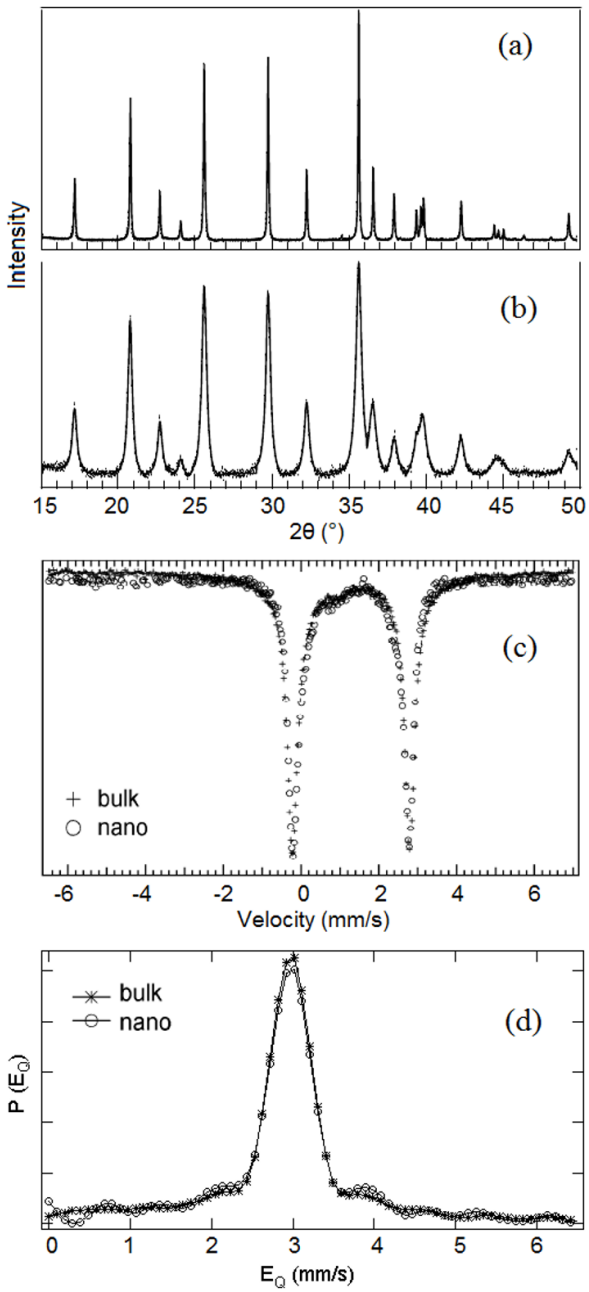

Figure 7.1: XRD patterns of (a) bulk-$LiFePO_4$ with 330 nm crystal size and (b) nano-$LiFePO_4$ with 26 nm crystal size. Crystal structure and lattice parameters were determined by Rietveld refinement as shown by the solid line. (c) Mössbauer spectra of bulk-$LiFePO_4$ and nano-$LiFePO_4$ at room temperature. The nano-$LiFePO_4$ was kept for one month at room temperature before measurement. (d) Distribution of electric quadrupole splitting $P(E_Q)$ of bulk-$LiFePO_4$ and nano-$LiFePO_4$, fitted from (c)

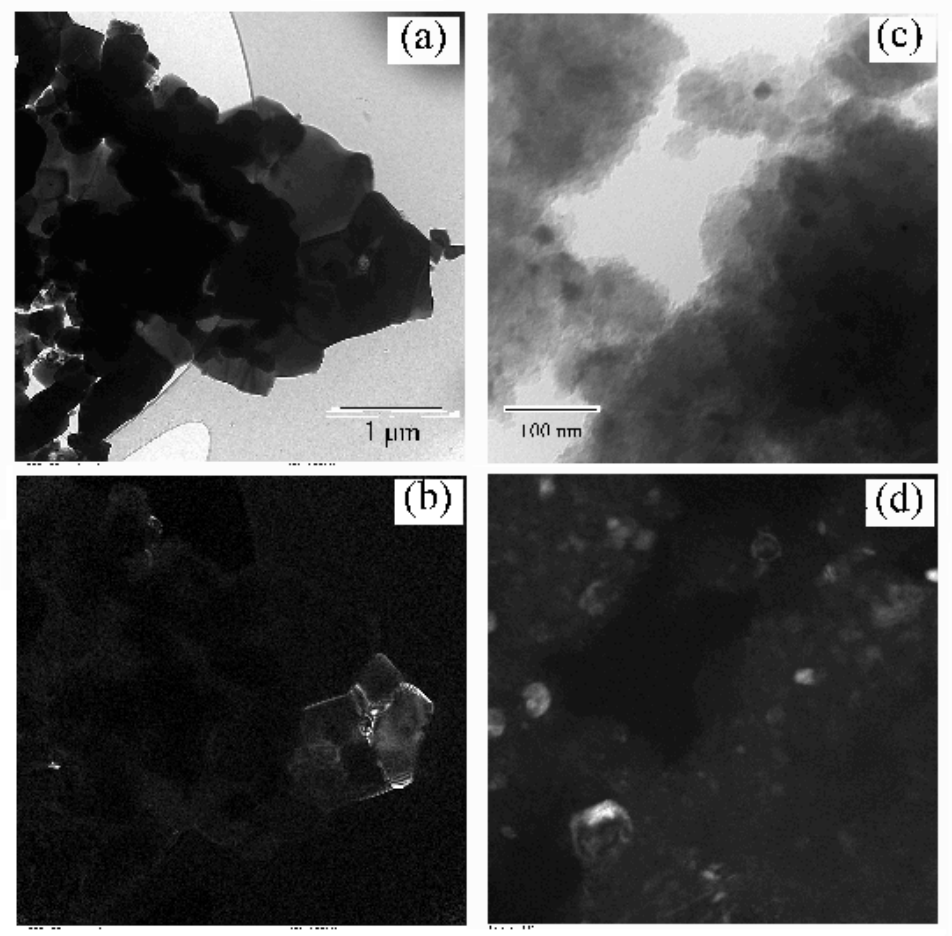

Figure 7.2: TEM images of (a) bright-field (BF) of bulk-$LiFePO_4$; (b) dark-field (DF) of bulk-$LiFePO_4$; (c) BF of nano-$LiFePO_4$; (d) DF of nano-$LiFePO_4$

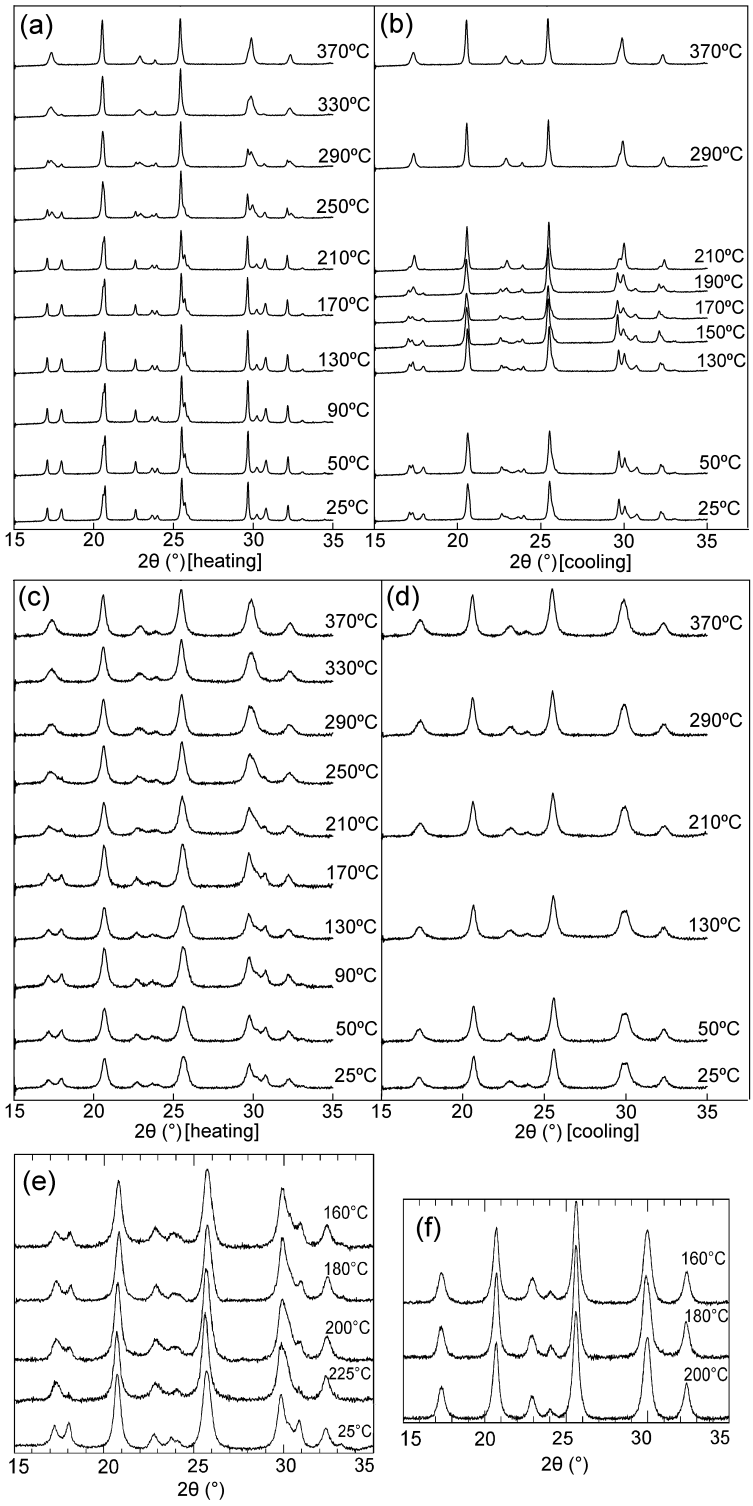

Figure 7.3: (a–d) In situ HT XRD patterns taken with the same conditions: (a) bulk-$Li_{0.65}FePO_4$ during heating from 25°C to 370°C, and (b) during cooling back to 25°C; (c) nano-$Li_{0.65}FePO_4$ during heating from 25°C to 370°C, and (d) during cooling back to 25°C. XRD patterns of (e) nano-$Li_{0.65}FePO_4$ two-phase mixture annealed at temperatures as labeled before quenching to room temperature, and (f) nano-$Li_{0.65}FePO_4$ two-phase mixture heated to 380°C for 12 hours and held at temperatures as labeled before quenching to room temperature. Annealing time at the given temperatures was 1 week for all samples in (e) and (f).

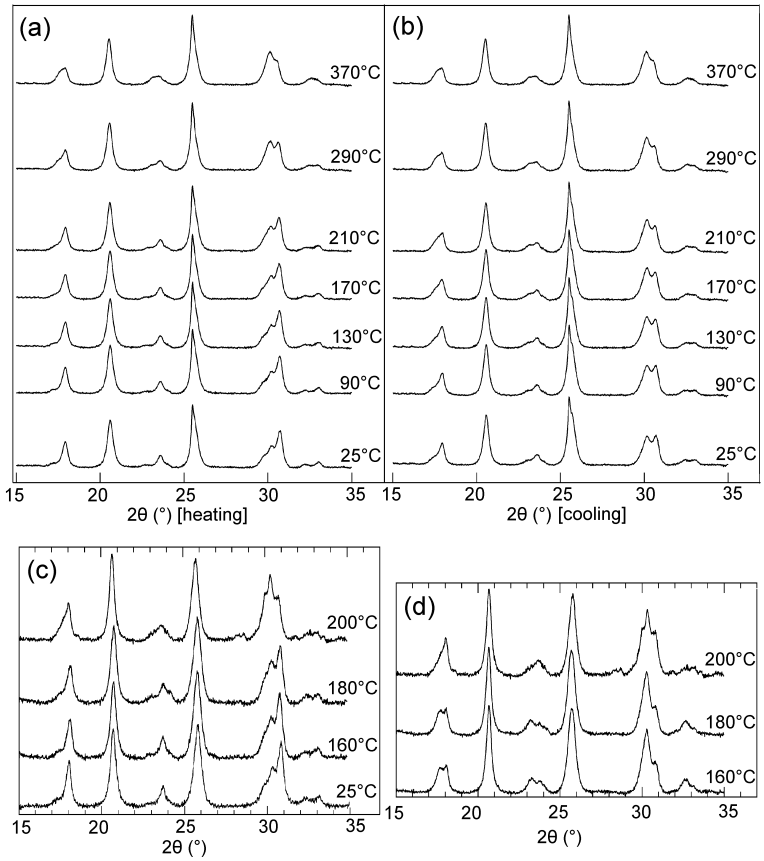

Figure 7.4: (a,b) In situ high-temperature XRD patterns of: (a) nano-$Li_{0.35}FePO_4$ during heating from 25°C to 370°C, and (b) during cooling back to 25°C. XRD patterns of (c) nano-$Li_{0.35}FePO_4$ two-phase mixture annealed at temperatures as labeled before quenching to room temperature, and (d) nano-$Li_{0.35}FePO_4$ two-phase mixture heated to 380°C for 12 hours and held at temperatures as labeled before quenching to room temperature. Annealing time at the given temperatures was 1 week for all samples in (c) and (d).

In previous work on bulk-Li_xFePO_4, unmixing upon cooling occurred when the temperature was decreased below 200°C [3]. In the case of nano-$Li_{0.65}FePO_4$, although the solid solution phase persisted for many days at temperatures below 200°C (Fig. 7.3(f)), we were unable to confirm that it is thermodynamically stable at these low temperatures. Although it is possible for the kinetics to differ between forward and reverse phase transformations, the thermodynamics must be the same. If the solid solution phase were stable thermodynamically, the two-phase mixture would transform to the solid solution phase at temperatures below 200°C. Figure 7.3(e) shows that this did not occur until temperature exceeded 200°C. Upon heating, it appears that the two-phase mixture has similar transformation behavior in both bulk-$Li_{0.65}FePO_4$ and nano-$Li_{0.65}FePO_4$ (compare Fig. 7.3(a) and (c)).

For the nano-$Li_{0.35}FePO_4$, both in situ XRD and long-time annealing treatments of the two-phase mixtures showed similar transformations to the solid solution phase (Fig. 7.4(a) and (c)). As

was found for the nano-$Li_{0.65}FePO_4$, once the solid solution phase formed in the nano-$Li_{0.35}FePO_4$, this phase was relatively stable against unmixing. Nevertheless, although the in situ XRD measurements did not show unmixing during cooling (Fig. 7.4(b)), the long-time annealing showed that the nano-$Li_{0.35}FePO_4$ solid solution undergoes unmixing below 200°C (Fig. 7.4(d)). The solid solution phase of nano-$Li_{0.35}FePO_4$ is not stable thermodynamically at low temperatures. Both the forward and reverse transformations indicate a transformation temperature of around 200°C for unmixing, nearly the same as for bulk-$Li_{0.35}FePO_4$ reported by Dodd et al. [3]. By measurements on more compositions, the temperature of 200°C was found to be an eutectoid temperature for bulk-Li_xFePO_4, and evidently this feature of the phase diagram is not changed for Li_xFePO_4 of 26 nm crystallite size.

All data of Fig. 7.3 and Fig. 7.4 are consistent with different kinetic effects of unmixing the solid solution in nano-Li_xFePO_4, but the two-phase mixture has similar thermodynamic stability compared to the solid solution in both bulk and nano-Li_xFePO_4. We note, however, that the present results are consistent with ideas that the surface structure around the crystallites, perhaps grain boundaries in agglomerated particles, help to stabilize the solid solution phase kinetically. The solid solution phase is most stable in crystallites with a large ratio of surface to crystal volume. Nevertheless, these suggestions, and evidence for extended solubility of the heterosite and triphylite phases in nanostructured materials, are worthy of further studies that test for stability over very long times.

7.4 Conclusion

Nanocrystalline $LiFePO_4$ with the olivine structure (triphylite) can be formed readily by ball milling. The crystal size as determined by XRD and TEM was approximately 26 nm. The crystals agglomerated into larger particles with relatively low exposed surface area, and were robust against forming Fe^{3+}. By heating and cooling treatments, followed by XRD measurements (sometimes in situ), it was found that the solid solution phase of the nano-$Li_{0.65}FePO_4$ material is much more stable than for the bulk-$Li_{0.65}FePO_4$. Once formed in nano-$Li_{0.65}FePO_4$, the solid solution did not unmix at any temperature. On the other hand, heating of the two-phase mixtures in the nano-Li_xFePO_4 ($x = 0.65$ and 0.35) above 200°C was unstable against forming the solid solution, similar to their bulk counterparts. More significantly, after long-time annealing of the solid solution of nano-$Li_{0.35}FePO_4$ at temperatures below 200°C, the material began to unmix into heterosite and triphylite. There is clearly a kinetic difference between the mixing and unmixing transformations in bulk-Li_xFePO_4 and nano-Li_xFePO_4. The solid solution phase of nano-$Li_{0.65}FePO_4$ is rather stable kinetically against unmixing, perhaps owing to surface structures around crystallites in materials having more Fe^{2+}. However, the equilibrium transformation temperatures are not substantially

different for bulk-Li_xFePO_4 and for nano-Li_xFePO_4 with 26 nm crystallite size.

Chapter 8

Phase Boundaries of the Heterosite and Triphylite Phases in Li_xFePO_4 $(0 \leq x \leq 1)$

8.1 Introduction

$LiFePO_4$, a promising cathode material for rechargeable lithium batteries, has been studied intensively since it was first proposed in 1997 [70]. Despite its well-known advantages, such as large capacity (170mAh/g), high stability, and low cost, substantial effort has been made to try to understand its thermodynamics, and to improve its conductivity of lithium ions and electrons. Olivine $LiFePO_4$ suffers a low electronic conductivity because electronic motion in its crystal lattice has to accommodate local distortions of atom positions in a process called small polaron hopping. Carbon coating has proved practical for improving electrical conductivity, as has preparing the material in nanocrystalline form.

At room temperature, lithium intercalation or deintercalation involves a transition between the two phases $LiFePO_4$ (triphylite) and $FePO_4$ (heterosite), giving a 3.45 V flat potential vs. lithium across most of the composition range. A solid solution phase was discovered above 200°C [72] and the eutectic phase diagram was assessed [3]. Previous work suggested that the phase diagram of Li_xFePO_4 should change with decrease of the crystal size [78]. This argument was supported by studies of the miscibility gap of Li_xFePO_4 at room temperature, which was found to shrink due to the crystal size reduction from hundreds of nanometers to below 100 nm [79, 85, 78, 80], and completely disappeared below 20 nm [78]. Other evidence of an altered phase boundary includes the extended solid solution behavior observed during cycling of nanocrystalline $LiFePO_4$ [76], or during the fast charging [77]. However, the change of the Li_xFePO_4 phase diagram was questioned in some recent work. For example, XRD patterns of annealed 25 nm Li_xFePO_4 showed the consistent transition temperature from the two-phase to the solid solution at 200°C [81]. Electrochemical cycling of jet-

milled 25 nm $LiFePO_4$ still resulted in a voltage plateau that was the same as the bulk material [82]. A recent calculation argued that the system is likely to choose a thermodynamic non-equilibrium path to avoid energy cost of nucleation and phase growth for kinetic advantages [92]. Coherent strain and surface modification were also reported as factors affecting the phase composition [148, 124]. These can be the reasons for observed cases of metastable "solid solution behavior", although they are not evidence for a change of the equilibrium phase diagram.

Confirming a change of phase diagram for nanocrystalline Li_xFePO_4 requires more experimental work on materials with crystal size below 50 nm. Our approach was to measure the boundaries between the two-phase mixture and the single-phase $Li_\alpha FePO_4$ or $Li_{1-\beta}FePO_4$, where α and β are small. A precise measurement requires the system to be in equilibrium. An electrochemical thermodynamic measurement system (ETMS) was used in this work, and its measurements are based on the following principles.

In an electrochemical cell, the Gibbs free energy ΔG represents the maximum amount of work that can be done by the system. The ΔG can be determined from an open-circuit measurement of potential V,

$$\Delta G = W_{max} = -nFV \ , \tag{8.1}$$

where $n = 1$ for Li^+/Li pair, and F is the Faraday constant of a mole of charge. Meanwhile, the second law of thermodynamics gives

$$\Delta G = \Delta U - T\Delta S + P\Delta V \ . \tag{8.2}$$

The temperature dependence of the potential V in Eq. 8.1 can be used to measure the entropy difference; by combining Eq. 8.1 and Eq. 8.2 it yields (assuming $dP = 0$, and replacing molar fraction by composition $x = n/N_A$)

$$\frac{\partial S}{\partial x}|_T = F\frac{\partial V}{\partial T}|_x, \tag{8.3}$$

and

$$\frac{\partial H}{\partial x}|_T = -FV + T\frac{\partial S}{\partial x}|_T = -FV + TF\frac{\partial V}{\partial T}|_x. \tag{8.4}$$

Equations 8.3 and 8.4 relate basic thermodynamic functions to electrochemical parameters. For example, a change of the entropy difference between the two electrodes with Li^+ concentration is proportional to the change of how the open-circuit voltage depends on temperature at a fixed state of charge.

In this work, we evaluated the boundaries of the two-phase mixture of heterosite and triphylite during Li insertion and extraction in Li_xFePO_4. We used the $LiFePO_4$ sample with an averaged crystal size of 70 nm, similar to the sample sizes in many previous studies on $LiFePO_4$ nanocrystallites. The boundaries between the two-phase mixture and the single-phase regions of $Li_\alpha FePO_4$

or $Li_{1-\beta}FePO_4$ were evaluated by open-circuit voltage measurements of profiles of entropy and enthalpy changes with composition. These boundaries were found narrower for the single phases than previous studies on nano-Li_xFePO_4 with even smaller crystal sizes.

8.2 Experimental

Samples of $LiFePO_4$ were prepared through an ordinary solid-state route. Precursors of LiOH, $Fe(C_2O_4)2H_2O$, $NH_4H_2PO_4$, and carbon black (Super P®) in a molar ratio of 1:1:1:3 were mixed and ground, and then annealed at 600°C with flowing gas of 95% N_2 and 5% H_2. Crystal size can be controlled by varying the annealing time from 5 h to 18 h. The added carbon black helps reduce Fe^{3+} and coats $LiFePO_4$ nanoparticles to reach higher conductivity.

A PANalytical X'pert PRO X-ray diffractometer (XRD) with Cu Kα radiation, a ZEISS 1550 VP field-emission scanning electron microscopy (FE-SEM), and a Tecnai F30 transmission electron microscopy (TEM) were used to determine the crystal structures and crystal sizes. Rietveld refinement was done with the software package Philips X'pert Plus to determine lattice parameters and phase fractions.

As-prepared $LiFePO_4$ powder was mixed with Super P Carbon and polyvinyldiene difluoride (PVDF) in a mass ratio of 85%:7.5%:7.5% and stirred in N-methyl-pyrrolidone (NMP) for 6 hours. The obtained slurry was deposited onto an Al spacer using a Finnpipette II single-channel pipetter, then dried on a hot plate at 150°C for 1 hr and immediately placed in a vacuum antechamber for an additional hour, before being brought into an argon-filled glove box (H_2O level of < 0.1ppm). Lithium metal ribbon and 1 M $LiPF_6$ in a 1:1 ethylene carbonate (EC) and dimethyl carbonate (DMC) solution were used as the counter electrode and electrolyte, respectively. A Millipore glass fiber prefilter was used as the separator. The 2032 coin cells were then assembled in an argon-filled glove box and were tested on a battery cycler. The tests were conducted between 1.8 V and 4.5 V at a constant current rate of C/10 and a constant voltage rate of C/100. After 3–5 cycles, the cells were then programmed to be charged at a C/20 rate on a Viaspace ETMS (Electrochemical Thermodynamic Measurement System) to above 4 V and were held at the charged state for 30 minutes or to a C/200 current, then discharged to 1.8 V, followed by holding this voltage to C/200 current. The cells were put at rest at each state of charge (SOC) for at least 6 hours to reach equilibrium. Then the cells were cooled down (either 25°C → 20°C → 15° or 25°C → 15°C → 5°) and heated back to 25°C using a thermoelectric cooling stage TE® CP-031, and open-circuit voltages were read by an Agilent 34970 data acquisition switch unit after 1 hour of relaxation at different temperatures.

As described in the introduction, using bulk Li on the anode can let us assume a constant entropy and enthalpy evolution at the anode, and our measurement thus evaluates only the effects

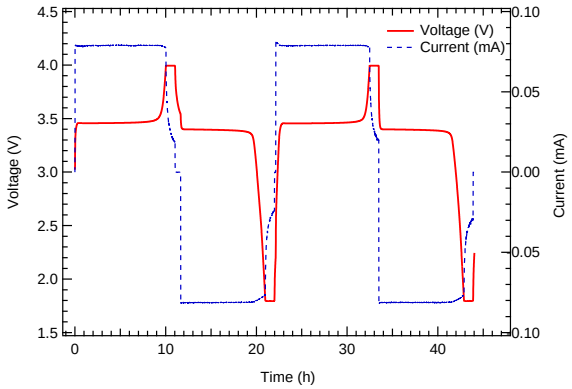

Figure 8.1: Galvanostatic charging and discharging of $LiFePO_4$ half cell under C/20 rate between 4.0 V and 1.8 V, followed by holding voltage limits at C/200 current rate for 30 minutes. The charging and discharging capacities are determined during the two cycles. Voltage (red solid line) and current (blue dashed line) are plotted with time.

of composition changes in the Li_xFePO_4 at the cathode. If the open-circuit voltages are measured under the thermodynamically reversible condition and plotted with corresponding temperatures, the slope and intercepts can give results of entropy and enthalpy change with composition at a specific x. This technique was used previously to measure thermodynamic parameters of Li_xCoO_2 and graphite electrode [149, 150]. The structural phase transitions during lithiation in Li_xCoO_2, for example, were associated with changes in the entropy profile [149].

8.3 Results and discussion

Synthesized $LiFePO_4$ materials crystalized into the olivine structure and have a characteristic crystal size of 70 nm estimated in XRD patterns and SEM images. Results of lattice parameters from the Rietveld refinement of its XRD patterns are in good agreement with previous studies [71, 79, 80]. Figure 8.1 shows a typical half-cell galvanostatic cycling of $LiFePO_4$ vs. Li. The voltage plateau around 3.4 V is usually attributed to a two-phase reaction in Li_xFePO_4. A cycling rate of C/10 was able to maintain about 148 mAh/g capacity which became stabilized after 5 cycles.

The stabilized cell was then put at rest at each state of charge (SOC). As an example, open-circuit voltage (OCV) measurement at 96% SOC is plotted in Fig. 8.2 with temperature. The OCV was read at 298K, 288K, 278K, and back to 298K at the end of one hour of relaxation at each temperature stage. When heated back to 298K, the OCV was expected to coincide with the initial reading at 298K. However, this reversibility cannot usually be achieved, due to factors including kinetic hysteresis and self-discharge, which are probably more influential at the fully charged and discharged states. A linear fitting in Fig. 8.2 of the OCVs with temperature gives the entropy and enthalpy change as function of SOC (or Li concentration x).

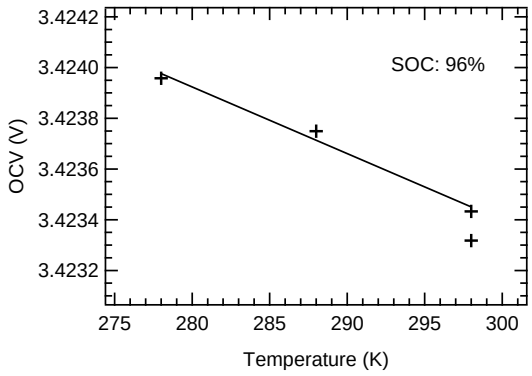

Figure 8.2: Open-circuit voltages (OCV) measured at temperatures of 298K, 288K, 278K, and back to 298K, for $LiFePO_4$ half cell at 96% state of charge. Slope of a linear fitting of OCVs suggests entropy change at this state of charge.

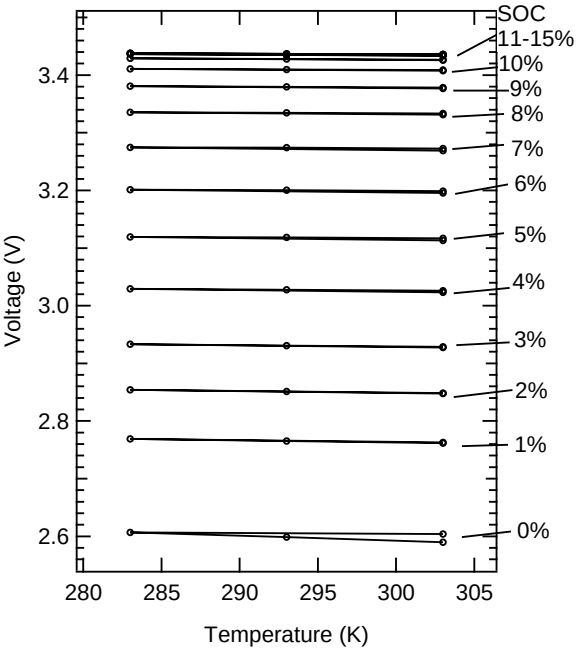

Figure 8.3: Open-circuit voltages (OCV) measured at temperatures of 303K, 293K, 283K, and back to 303K, for $LiFePO_4$ half cell at states of charge from 0% to 15%. Slope of a linear fitting of OCVs suggests entropy change at each state of charge.

Figure 8.3 shows the change of OCV with temperatures from 0% to 15% SOC with 1% increment. The OCV has a monotonic increase from 0% to about 10%. Above 11% SOC, the plots overlap at approximately 3.42 V, indicating the electrochemical reaction comes into the two-phase plateau. Similar voltage profile was reported previously [80] as the OCV reaches the plateau at about 9% SOC for 80 nm $LiFePO_4$ and another OCV study [151] in which 10% SOC was found as the beginning of voltage plateau during charging. Nonetheless, our investigation of entropy and enthalpy profiles provides a more thorough investigation, as described below.

During discharging when starting as $FePO_4$ (x=0), Fig. 8.4 shows the OCVs, entropy profile (ΔS), and enthalpy profile (ΔH) of Li_xFePO_4 vs. Li concentration between the composition ranges of x from 0 to 0.15. The trend of OCV does not differ between various temperatures, so only those measured at 298K are plotted here. The enthalpy profile in Fig. 8.4 resembles the mirrored OCV curve. The OCV, entropy, and enthalpy curves do not show much difference, as the plateau begins all around x=0.05 (or even earlier). This indicates the boundary between the homogenous $Li_\alpha FePO_4$ and two-phase mixture of triphylite and heterosite near the heterosite end is around x=0.05.

At the other end, starting as $LiFePO_4$ (x=1) during charging, Fig. 8.5 shows the OCVs, entropy profile (ΔS), and enthalpy profile (ΔH) of Li_xFePO_4 vs. Li concentration between the composition ranges of x from 0.84 to 1. The OCV curve in Fig. 8.5 shows that voltage is stabilized at 3.42 V from x=0.90, equivalent to Fig. 8.3. The entropy profile in Fig. 8.5, however, does not look the same as the OCV curve. The plateau of the entropy change (ΔS) starts as early as x=0.95. The entropy plateau is around -6 J/Mole/K, or -0.72 k_B, where k_B is the Boltzman constant. The enthalpy profile in Fig. 8.5 resembles the mirrored OCV curve.

The entropy is expected to remain constant in a two-phase system, where Li insertion or extraction occurs as moving of interphase boundary. On the other hand, random mixing of vacancy into the lithium atoms or vice versa as a single homogenous phase creates change of entropy in logarithmic relation to the composition, as a derivation of entropy of mixing over composition shown in Eq. 8.5:

$$\frac{\partial S}{\partial x} = -k_B \frac{\partial}{\partial x}[x \ln x + (1-x)\ln(1-x)] = k_B \ln \frac{1-x}{x} \,, \tag{8.5}$$

where k_B is the Boltzman constant. Thus entropy change helps determine if the system is in a single-phase or two-phase region during charge that begins as $LiFePO_4$ or discharge as $FePO_4$. Starting as x=1 in Fig. 8.5, as a transition from logarithmic curve to a constant flat line happens at a composition of x=0.95, the entropy change may be an alternative indication of the two-phase boundary to OCV. Previous studies on Li_xFePO_4 raised the issue of temperature-dependent measurements of OCVs [151]. In their work, the measured potential values showed the sloped region became narrower when the temperature was raised from 30°C to 60°C. Results of entropy change, which are independent of temperature, may provide more precise information on the phase boundaries.

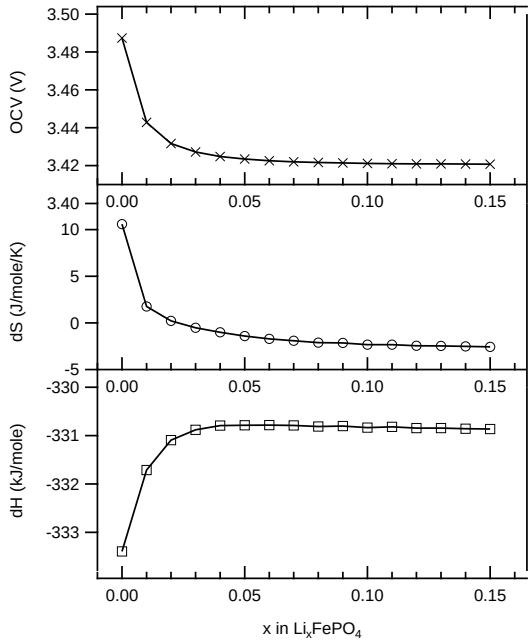

Figure 8.4: The open-circuit voltage (OCV), entropy profile (ΔS), and enthalpy profile (ΔH) of Li_xFePO_4 vs. Li concentration between x=0 and x=0.15

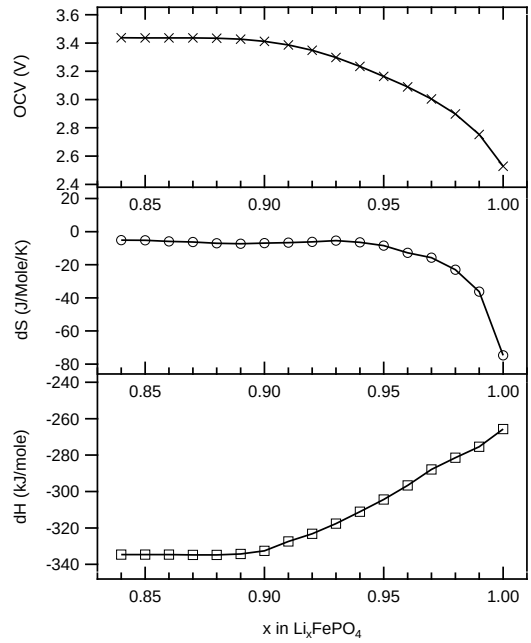

Figure 8.5: The open-circuit voltage (OCV), entropy profile (ΔS), and enthalpy profile (ΔH) of Li_xFePO_4 vs. Li concentration between x=0.84 and x=1

The ΔS stays around -0.7 k_B instead of 0 k_B across the plateau from x=0.05 to x=0.95, This deviation suggests a constant decrease of the entropy from the charged state to the discharged state with increase of x. The decrement is likely to come from the vibrational entropy on the electrode of Li_xFePO_4. The vibrational entropy is probably different between the two-phase of heterosite and triphylite and the solid solution phases of $Li_\alpha FePO_4$ or $Li_{1-\beta}FePO_4$. However, whether the vibrational entropy is large enough to affect the phase diagram of Li_xFePO_4 is unclear.

Enthalpy values on both ends fall on a plateau of about -335 kJ/mole, except for the compositions of x=0.9 to 1.0 with high lithium concentration. This is equivalent to about -3.48 eV per unit molecule, and about -2.7 eV per unit molecule for compositions between x=0.9 and x=1.0. A recent calculation of mixing energy with various atomic configuration showed a 15 meV plateau from x=0.05 to x=0.9, relative to that at x=0 or 1 [92], which is substantially small compared to the measurement in this work. Enthalpy of mixing is expected to only affect single-phase system during vacancy or lithium intercalation. Reasons for the difference between the enthalpy curve and entropy curve in Fig. 8.5 are unclear, as is the difference between the vacancy disordering at x close to 1 and Li disordering at x close to 0. One possible reason can be the additional energy cost of lattice relaxation when the interface boundary forms with increased vacancies, which means the system is more sensitive to the lattice strain caused by entering vacancies. This is supported by refinement work of solid solution XRD patterns, in which lattice parameters with small Li concentration deviate from the two-phase counterparts further [72, 2]. Another reason can be the different phase stability at the two ends. When the Li atoms mix with more and more vacancies, the system cannot maintain the homogeneity, which changes the flat plateau between x=0.90 and x=0.95 to be a slope region in the OCV and enthalpy curves.

8.4 Conclusion

Based on the results of the OCV, ΔS, and ΔH, the boundaries of the two-phase mixture of heterosite and triphylite can be determined as x=0.05 for the Li-poor end, and x=0.95 for the Li-rich end in Li_xFePO_4 with a characteristic crystal size of 70 nm. These are similar values with previous results on Li_xFePO_4 in bulk crystal size of hundreds of nanometers. These are also wider range for the two-phase plateau than those previously reported results on Li_xFePO_4 with similar or even smaller crystal sizes. It is thus fair to conclude that phase boundaries of heterosite and triphylite at room temperature do not change with decrease of crystal size, nor does the phase diagram of Li_xFePO_4.

Chapter 9

Future Work

9.1 Summary

In the past ten years, tremendous effort has been made to try to understand $LiFePO_4$ as a cathode material for rechargeable Li batteries, and to improve its performance for commercialization. The low electric conductivity is recognized as the biggest disadvantage of $LiFePO_4$. Carbon coating and crystal size minimization have been reported as the two most effective methods to enhance its electric conductivity. We contributed to the understanding of these issues of conductivity by studying the thermodynamics and charge kinetics of $LiFePO_4$ with crystal sizes reduced to the nanoscale.

We pioneered several different processes for engineering nanocrystalline $LiFePO_4$ including a simple method of mechanical attrition. There is a big controversy in the community over whether decreasing the crystal size can change the kinetics, the electrochemical performance, or even the thermodynamics. We first studied the polaronic dynamics in nano-Li_xFePO_4 by Mössbauer spectrometry and found a valence fluctuation between Fe^{2+} and Fe^{3+}. The results showed that the electric conductivity in the nano-Li_xFePO_4 are comparable to that of the bulk-Li_xFePO_4 prepared as solid solutions, but both are much higher than the conductivity in the bulk-Li_xFePO_4 two-phase mixtures, which is the expected phase for electrochemical lithiation. This increase of intrinsic conductivity in nano-Li_xFePO_4 is consistent with the evidence of improved rate capability shown by some other groups.

Because some previously published work argued that the phase diagram could be altered with reduced crystal size, we studied the phase transition from the two-phase mixtures to the solid solutions in nano-Li_xFePO_4 at elevated temperatures. We observed a consistent phase transition temperature around 200°C, and a change in the stability in the solid solution phase for some compositions in nano-Li_xFePO_4. We also studied the phase boundaries of the two-phase heterosite and triphylite at room temperature by measuring the thermodynamical parameters during electrochemical lithiation or delithiation. The profiles of the open-circuit voltage, entropy change, and enthalpy change as functions of composition showed boundaries of x=0.05 and x=0.95 for Li_xFePO_4 with characteristic

crystal size of 70 nm. The results are consistent with other studies of the bulk-Li_xFePO_4. Our results on the nano-Li_xFePO_4 call into question of the validity of previous claims of a significant change in the phase diagram of Li_xFePO_4 when the crystal size is 30 or 40 nm.

9.2 Future work on nano-Li_xFePO_4

9.2.1 Further attempts to improve the kinetics of Li_xFePO_4

Engineering $LiFePO_4$ into nanocrystallites increases the crystal surface area and shortens Li ion diffusion paths. Because we showed that there is impurity Fe^{3+} at the surface, it would be best if only the length of the one-dimensional Li channels (b-direction in Pnma symmetry) is minimized while the crystal still keeps a larger structure in the other two dimensions. To achieve this, fabricating $LiFePO_4$ as a thin film on a carbon substrate with controlled thickness along b direction, e.g., by mechanical or chemical deposition, seems promising. A well-structured cathode with folded $LiFePO_4$ thin films can possibly provide high rate capability.

Our study showed that the intrinsic electric conductivity of Li_xFePO_4 is low, due to a high activation energy barrier for polaron hopping above 400 meV. The most common route to increase the electric conductivity of $LiFePO_4$ is carbon coating, which helps conduct electron motion. Carbon coating probably works in a physical way, unlike the many catalysts used in chemical engineering for the purpose of reducing the activation energy barrier. Recently, an improved rate capability has been observed in the layered metal oxide system by coating with catalyst oxides, such as SiO_2, Al_2O_3, or $AlPO_4$. The reaction mechanism is still not clear, but perhaps they may give olivine $LiFePO_4$ a similar improvement. Could they participate in the small polaron hopping as a catalyst to lower the activation energy?

9.2.2 Further study on the electrical conductivity of the olivine cathodes

Mössbauer spectrometry provides an accurate evaluation on the intrinsic electric conductivity in Li_xFePO_4 nanocrystallites by measuring the dynamical change of hyperfine interactions caused by small polaron hopping at Fe atoms. The advantage of its sensitivity can let us carry out further studies on polaronic dynamics that occur at Fe ions with mixed valences. It is also useful for comparing materials with similar chemical environments for Fe, but with modified elemental compositions or preparations.

Introducing a second metallic cation in the olivine can change the chemical environment and charge distribution at Fe atoms. One good option could be a lighter transition metal, for example Ti. The titanium-doped $LiFe_{0.9}Ti_{0.1}PO_4$ has the same olivine structure as $LiFePO_4$, with slight decrease of the lattice parameters (about 0.01 Å shown in Fig. 9.1). Ti appears to substitute on

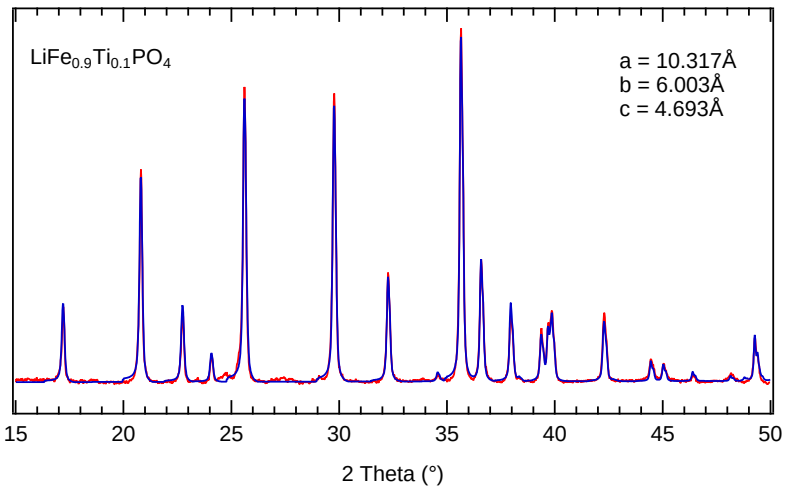

Figure 9.1: The XRD pattern of $LiFe_{0.9}Ti_{0.1}PO_4$. The red line is the raw data and the blue line is the Rietveld refinement with olivine $LiFePO_4$.

Fe sites. However, at high cycling rates, $LiFe_{0.9}Ti_{0.1}PO_4$ showed a much better rate capability than $LiFePO_4$. In situ Mössbauer spectrometry found a change of absorption line positions and shape when delithiated $Li_{0.45}Fe_{0.9}Ti_{0.1}PO_4$ was heated to 200°C (Fig. 9.2). The spectrum was recovered after the sample was cooled back to room temperature. This probably indicates increased dynamics at elevated temperatures which are not seen at room temperature. Further studies of the thermodynamics and the charge kinetics on this doped olivine $LiFe_{0.9}Ti_{0.1}PO_4$ could be important to the battery community.

Besides Mössbauer spectrometry, other techniques are necessary to understand the intrinsic conductivity in olivine materials. Since polaron hopping occurs between two FeO_6 octahedra, the electron has to tunnel through the barrier at the oxygen atom shared by the two FeO_6. The previous DFT calculation [91] suggested low energy cost for the hopping of an isolated charge, and a binding of Li ion and the electron. This work has been used to explain many experimental results, although far from being accurate. However, the suggestion of Li^+–e^- coupling is important for understanding the electric conductivity. Isolating lithium motion experimentally seems hard to realize, and computational work requires more advanced theories. However, the dynamics of lithium atoms can be studied by nuclear magnetic resonance or electron spin resonance. It may be useful to study if there are correlations between the temperature dependence of Li motions and valence fluctuations at Fe atoms.

9.2.3 Further study on the phase diagram of Li_xFePO_4

To investigate the phase diagram in the nano-Li_xFePO_4, we determined boundaries of triphylite and heterosite two-phase mixtures by the electrochemical thermodynamic measurement using $LiFePO_4$

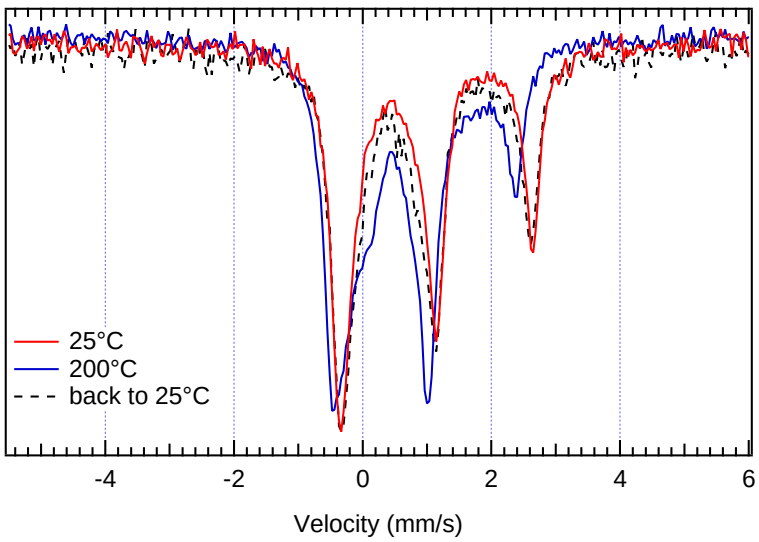

Figure 9.2: Mössbauer spectra of $Li_{0.45}Fe_{0.9}Ti_{0.1}PO_4$, similar to that of Li_xFePO_4. Red line is the measurement at 25°C, the blue line was measured at 200°C, and the dashed black line was measured after sample was cooled back to 25°C.

samples with 70 nm crystal size, described in the previous chapter. It may be important to compare results on $LiFePO_4$ samples with different crystal sizes. We prepared the nano-$LiFePO_4$ ($\sim$ 50 nm) by ball-milling with carbon, together with a controlled bulk-$LiFePO_4$ ($\sim$ 300 nm) prepared in the same procedure. The nano-$LiFePO_4$, however, did not show better rate capability than the bulk counterpart (Fig. 9.3). It would be interesting to see if they give the same results on the open-circuit voltage, entropy, and enthalpy profiles.

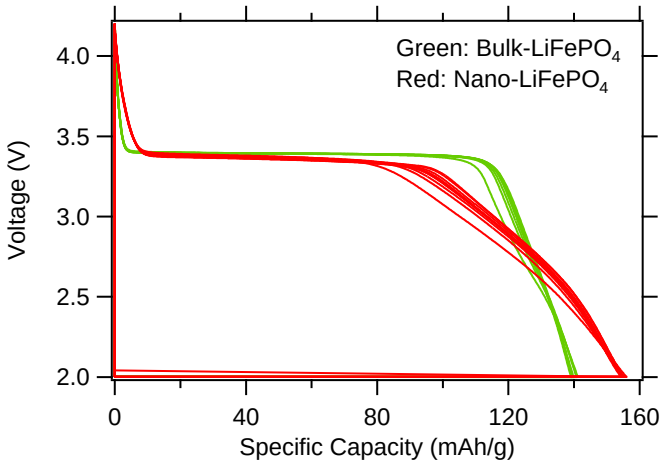

Figure 9.3: Comparison between the galvanostatic cycling of bulk-$LiFePO_4$ ($\sim 300\,nm$) and nano-$LiFePO_4$ ($\sim 50\,nm$) at C/20 rate

Appendix A

A Mössbauer Spectrometer Using Buffered Counting and LabVIEW Software

A simple "simulated" multichannel analyzer (MCA) for Mössbauer spectrometer was constructed with a 32-bit buffered counter from National Instruments and LabVIEW programming. Unlike Mössbauer data acquisition by an expensive commercial external MCA device with inflexible software, signal synchronization and spectrum construction are achieved directly by the buffered counter controlled by our customized LabVIEW-based platform.

A.1 Introduction

A Mössbauer spectrometer uses the Mössbauer effect to study nuclear hyperfine interactions by counting photons or electrons. The source photon energy is modulated by a Doppler drive unit, which maintains a constant acceleration/deceleration motion and scans periodically through an adequate velocity range. At each sequential registered velocity (noted as a channel), output signals from the detector are counted within a certain time interval, usually tens of microseconds. In transmission geometry, these signals correspond to transmitted photons not resonantly absorbed by the Mössbauer nuclei, and are used to construct the spectrum. The periodic velocity scan is synchronized with the detector signal counting, and repeated to build up a spectrum over time.

Data acquisition for Mössbauer spectrometry is conventionally handled with a single-purpose electronic system called multichannel analyzer (MCA). A MCA performs essential functions of storing counts in multiple channels, displaying histograms, and saving the data for further analysis. Despite many options of commercial MCA add-on cards, customized designs based on microprocessors, micro-controllers, or personal computers (PC) were reported to build up "simulated" MCAs [152, 153, 154, 155, 156]. Examples of using LabVIEW to collect Mössbauer data directly from detector signals show the convenience and versatility of this graphical programming technique

[157, 158].

In this chapter, we report our design of an MCA on a LabVIEW platform with a single 32-bit counter from National Instruments, now the key component of our Mössbauer spectrometer. Compared to many commercial MCA add-on units with redundant features [159], our virtual MCA provides a straightforward and elegant solution for multichannel scaling (MCS), controlling, and data storage. It has a low cost, high accuracy, high efficiency, and good compatibility with multiple computer operating systems.

A.2 Signal Processing Description

Our Mössbauer spectrometer is set up in a transmission configuration. The 25 kHz TTL pulse train, "CHA", generated from a digital function generator (Wissel DFG-1200), is used as gate signal for counting. For every 1024 CHA pulses, a second TTL pulse train, "START", is generated from a frequency divider circuit. This START pulse train (about 25 Hz) sets the frequency of the triangular velocity waveform, and indicates the starting time of a new period of a velocity scan.

The counter function on a National Instruments data acquisition module (USB-6221) is used with LabVIEW commands control. The counter has an 80 MHz onboard clock and 32-bit resolution, both high enough for Mössbauer spectrometers. It counts TTL signals from the single channel analyzer (SCA), which converts amplified analog signals from the detector that pass its two thresholds into digital signals. Buffered event counting is realized by using an active edge of TTL signal "CHA", which acts as a control signal to register a memory address. It then counts source signals from the SCA until the next active edge of "CHA" signal is received. Then the current count value is locked into the registered memory, and a new memory address is allocated for the next counting. This repeats and there is a finite number (1024) of counting results corresponding to every two adjacent "CHA" signals. Every time counting starts after receiving "START" signal, and stops to start from the beginning when another "START" signal arrives. After 10 cycles of the 1024 channel counting, the set of counting results in the buffer is read by LabVIEW through a USB interface as an array of 32-bit integers. To construct a spectrum, each array of counts is added, and a real-time histogram is displayed. Since every time counting starts at a "STAR" trigger signal, this synchronizes the motion of the Doppler drive, which is critical for obtaining a correct spectrum. By using signals generated from the function generator and buffered event counting, an MCA function is achieved in a simple way. Figure A.1 is a schematic illustration of the whole spectrometer. The signal processing is shown in Fig. A.2, where the left column explains how the counter functions for data collection and the right column shows how signals from the detector are processed before being counted. The logic flowchart in Fig. A.3 illustrates the synchronization and data acquisition in the MCA LabVIEW program.

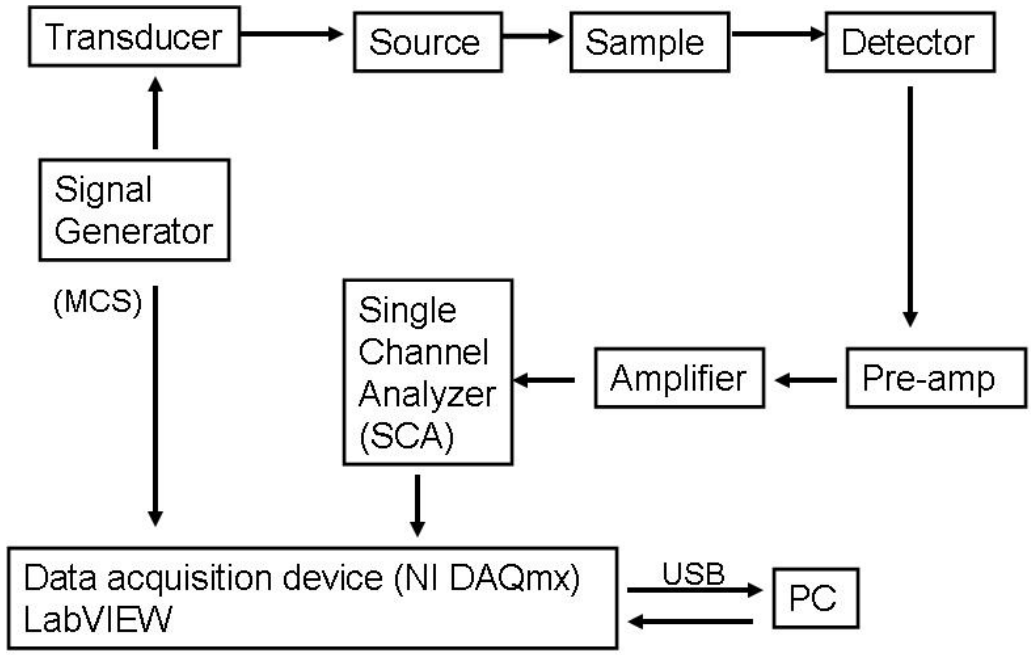

Figure A.1: The diagram of the spectrometer

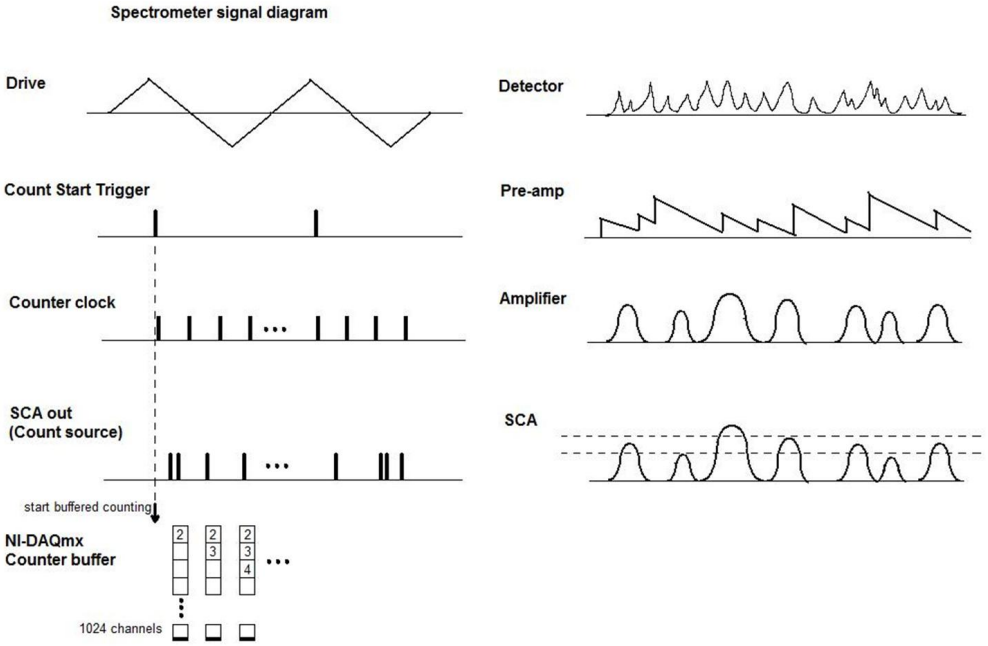

Figure A.2: The diagram of signal processing in MCA mode

Table A.1: The fitting results of Fe spectrum and nonlinearity

i	1	2	3	4	5	6
position (mm/s)	-5.315	-3.071	-0.838	0.841	3.079	5.305
nonlinearity (%)	-0.06	0.04	0.05	-0.02	0.03	-0.04
FWHM (mm/s)	0.294	0.294	0.266	0.252	0.292	0.300

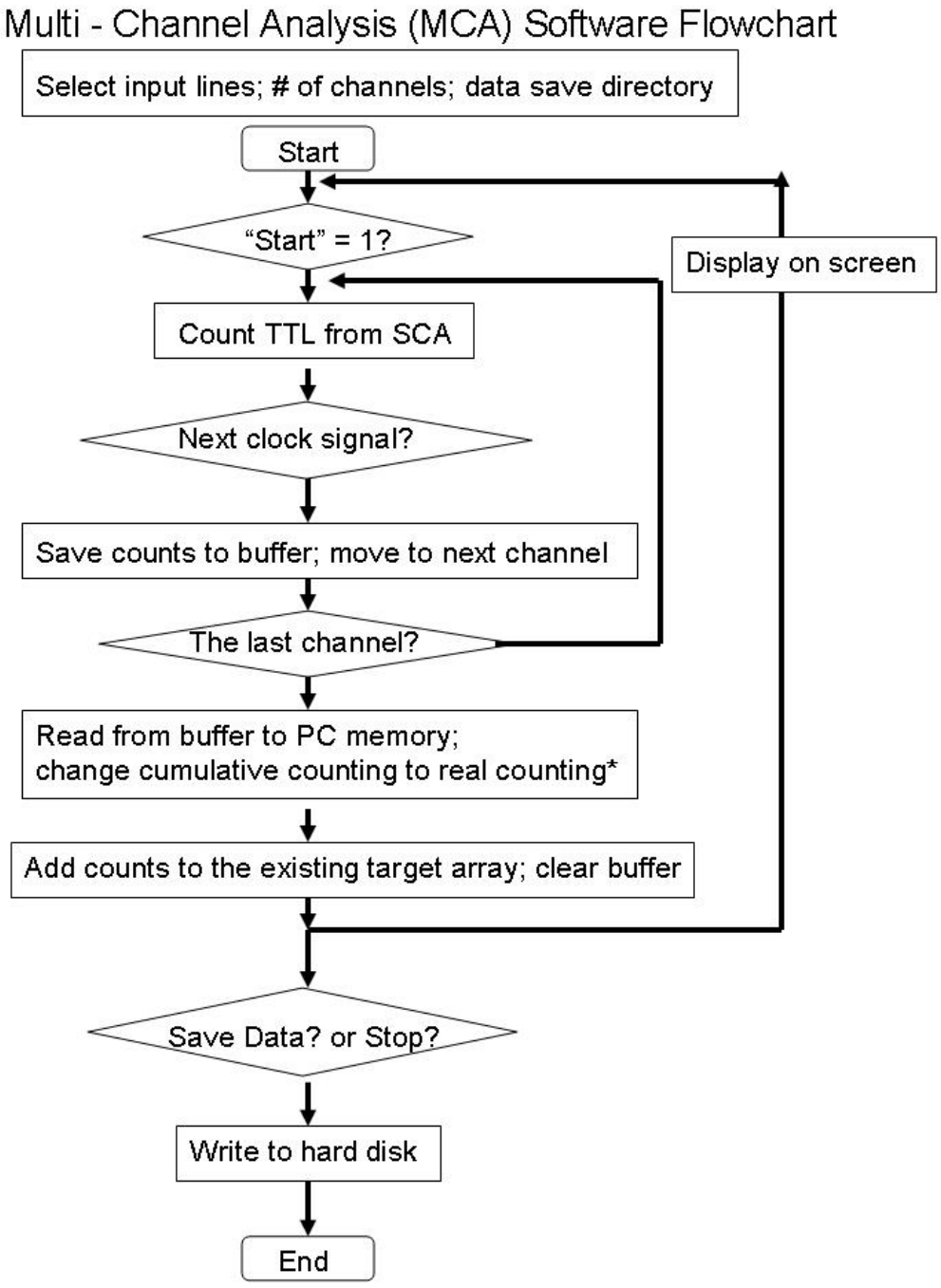

Figure A.3: The logic flowchart in MCA mode

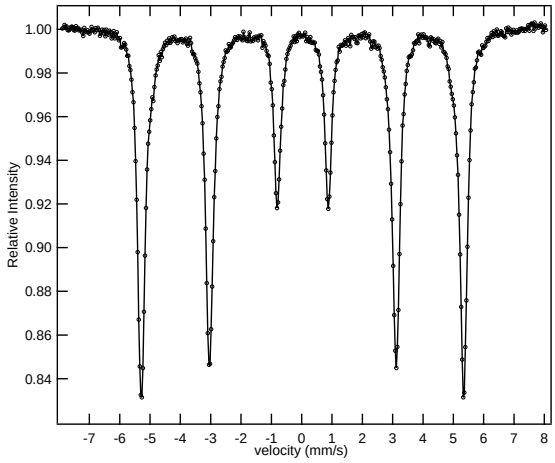

Figure A.4: A Mössbauer spectrum of natural iron acquired from our spectrometer

A.3 Testing results

Figure A.4 is a Mössbauer spectrum of a natural α-Fe sample obtained from our spectrometer after folding the two mirrored spectra. After fitting the sexet absorption lines with Lorentzian functions, the drive velocity is calibrated by assuming 0 mm/s isomer shift and 10.62 mm/s distance between the two outer-lines. The six spectral line positions and widths are thus obtained in Table A.1. The nonlinearity of the spectrometer is also evaluated from this iron spectrum as shown in Table A.1. The algorithm is described in Ref. [158], as:

$$nonlinearity = \frac{x(i) - av(i) - b}{v(6) - v(1)} \tag{A.1}$$

where i $(i = 1\ t; 6),\ x(i),\ v(i),\ a,\ b$ are spectral line number, measured line position, theoretical line position, and two parameters from the least square method, respectively. The spectrum in Figure A.4 was collected for 24 hours, with an absorption ratio of about 14%. The quality of the spectrum is comparable to that of a commercial MCA. Our source code can be provided upon request.

Bibliography

[1] K. Amine, J. Liu, and I. Belharouak. High-temperature storage and cycling of C-$LiFePO_4$/graphite Li-ion cells. *Electrochem. Commun.*, 7(7):669, 2005.

[2] H. J. Tan, J. L. Dodd, and B. Fultz. Mössbauer spectrometry study of thermally-activated electronic processes in Li_xFePO_4. *J. Phys. Chem. C*, 113(6):2526, 2009.

[3] J. L. Dodd, R. Yazami, and B. Fultz. Phase diagram of Li_xFePO_4. *Electrochem. Solid-State Lett.*, 9(3):A151, 2006.

[4] G. Lecaer and J. M. Dubois. Evaluation of hyperfine parameter distributions from overlapped Mössbauer-spectra of amorphous alloys. *J. Phys. E Sci. Instrum.*, 12(11):1083, 1979.

[5] J. L. Dodd, I. Halevy, and B. Fultz. Valence fluctuations of Fe-57 in disordered $Li_{0.6}FePO_4$. *J. Phys. Chem. C*, 111(4):1563, 2007.

[6] J. M. Tarascon and M. Armand. Issues and challenges facing rechargeable lithium batteries. *Nature*, 414:359, 2001.

[7] A. J. Bard and L. R. Faulkner. *Electrochemical methods: fundamentals and applications*, chapter 2. John Wiley & Sons, Inc., 2nd edition, 2001.

[8] A. J. Bard and L. R. Faulkner. *Electrochemical methods: fundamentals and applications*, chapter 3. John Wiley & Sons, Inc., 2nd edition, 2001.

[9] A. J. Bard and L. R. Faulkner. *Electrochemical methods: fundamentals and applications*, chapter 4. John Wiley & Sons, Inc., 2nd edition, 2001.

[10] M. S. Whittingham. Electrochemical energy storage and intercalation chemistry. *Science*, 192:1226, 1976.

[11] B. M. L. Rao, R. W. Francis, and H. A. Christopher. Lithium-aluminium electrode. *J. Electrochem. Soc.*, 124:1490, 1977.

[12] R. Yazami and P. H. Touzain. A reversible graphite-lithium negative electrode for electrochemical generators. *J. Power Sources*, 9:365, 1983.

[13] T. Nagaura and K. Tozawa. Lithium ion rechargeable battery. *Prog. Batteries Solar Cells*, 9:209, 1990.

[14] S. Yang, X. Feng, L. Zhi, Q. Cao, J. Maier, and K. Mullen. Nanographene-constructed hollow carbon spheres and their favorable electroactivity with respect to lithium storage. *Adv. Mater.*, 22:838, 2010.

[15] P. Guo, H. Song, and X. Chen. Hollow graphene oxide spheres self-assembled by W/O emulsion. *J. Mater. Chem.*, 20:4867, 2010.

[16] L. F. Cui, Y. Yang, C. M. Hsu, and Y. Cui. Carbon-silicon core-shell nanowires as high capacity electrode for lithium ion batteries. *Nano Lett.*, 9:3370, 2009.

[17] M. H. Park, M. G. Kim, J. B. Joo, K. T. Kim, J. Y. Kim, S. H. Ahn, Y. Cui, and J. P. Cho. Silicon nanotube battery anodes. *Nano Lett.*, 9(11):3844, 2009.

[18] J. Graetz, C. C. Ahn, R. Yazami, and B. Fultz. Highly reversible lithium storage in nanostructured silicon. *Electrochem. Solid-State Lett.*, 6:A194, 2003.

[19] J. Graetz, C. C. Ahn, R. Yazami, and B. Fultz. Nanocrystalline and thin film germanium electrodes with high lithium capacity and high rate capabilities. *J. Electrochem. Soc.*, 151:A698, 2004.

[20] X. W. Lou, Y. Wang, C. Yuan, J. Y. Lee, and L. A. Archer. Template-free synthesis of SnO_2 hollow nanostructures with high lithium storage capacity. *Adv. Mater.*, 18:2325, 2006.

[21] J. Y. Huang, L. Zhong, C. M. Wang, J. P. Sullivan, W. Xu, L. Q. Zhang, S. X. Mao, N. S. Hudak, X. H. Liu, A. Subramanian, H. Fan, L. Qi, A. Kushima, and J. Li. In situ observation of the electrochemical lithiation of a single SnO_2 nanowire electrode. *Science*, 330:1515, 2010.

[22] D. H. Wang, D. Choi, J. Li, Z. G. Yang, Z. M. Nie, R. Kou, D. H. Hu, C. M. Wang, L. V. Saraf, J. G. Zhang, I. A. Aksay, and J. Liu. Self-assembled TiO_2-graphene hybrid nanostructures for enhanced Li-ion insertion. *ACS NANO*, 3(4):907, 2009.

[23] M. S. Whittingham. Role of ternary phases in cathode reactions. *J. Electrochem. Soc.*, 123:315, 1976.

[24] B. Ellis, W. R. M. Makahnouk, Y. Makimura, K. Toghill, and L. F. Nazar. A multifunctional 3.5V iron-based phosphate cathode for rechargeable batteries . *Nat. Mater.*, 6:749, 2007.

[25] S. Okada, M. Ueno, Y. Uebou, and J. Yamaki. Fluoride phosphate Li_2CoPO_4F as a high-voltage cathode in Li-ion batteries. *J. Power Sources*, 146:565, 2005.

[26] J. Barker, M. Y. Saidi, R. K. B. Gover, P. Burns, and A. Bryan. The effect of Al substitution on the lithium insertion properties of lithium vanadium fluorophosphate, $LiVPO_4F$. *J. Power Sources*, 174:927, 2007.

[27] A. Nyten, A. Abouimrane, M. Armand, T. Gustafsson, and J. O. Thomas. Electrochemical performance of Li_2FeSiO_4 as a new Li-battery cathode material. *Electrochem. Commun.*, 7:156, 2005.

[28] N. Recham, J-N. Chotard, J-C. Jumas, L. Laffont, M. Armand, and J-M. Tarascon. Ionothermal synthesis of li-based fluorophosphates electrodes. *Chem. Mater.*, 22(3):1142, 2010.

[29] K. Zaghib, A. A. Salah, N. Ravet, A. Mauger, F. Gendron, and C. M. Julien. Structural, magnetic and electrochemical properties of lithium iron orthosilicate. *J. Power Sources*, 160:1381, 2006.

[30] A. Kokalj, R. Dominko, G. Mali, A. Meden, M. Gaberscek, and J. Jamnik. Beyond one-electron reaction in Li cathode materials: Designing $Li_2MnxFe_{1-x}SiO_4$. *Chem. Mater.*, 19:3633, 2007.

[31] K. Mizushima, P. C. Jones, P. J. Wiseman, and J. B. Goodenough. $LixCoO_2$ ($0< x < 1$): A new cathode material for batteries of high energy density. *Mater. Res. Bull.*, 15(6):783, 1980.

[32] T. Ohzuku and A. Ueda. Layered lithium insertion material of $LiCo_{1/3}Ni_{1/3}Mn_{1/3}O_2$ for lithium-ion batteries. *J. Electrochem. Soc.*, 141:2972, 1994.

[33] J. N. Reimers and J. R. Dahn. Electrochemical and in situ X-Ray diffraction studies of lithium intercalation in Li_xCoO_2. *J. Electrochem. Soc.*, 139:2091, 1992.

[34] X. Q. Yang, X. Sun, and J. McBreen. New phases and phase transitions observed in $Li_{1-x}CoO_2$ during charge: in situ synchrotron X-ray diffraction studies. *Electrochem. Commun.*, 2:100, 2000.

[35] A. Rougier, P. Gravereau, and C. Delmas. Optimization of the composition of the $Li_{1-z}Ni_{1+z}O_2$ electrode materials: Structural, magnetic, and electrochemical studies. *J. Electrochem. Soc.*, 143:1168, 1996.

[36] S. K. Mishra and G. Ceder. Structural stability of lithium manganese oxides. *Phys. Rev. B*, 59:6120, 1999.

[37] G. Vitins and K. West. Lithium intercalation into layered $LiMnO_2$. *J. Electrochem. Soc.*, 144:2587, 1997.

[38] T. Ohzuku and Y. Makimura. Layered lithium insertion material of $LiCo_{1/3}Ni_{1/3}Mn_{1/3}O_2$ for lithium-ion batteries. *Chem. Lett.*, 30(7):642, 2001.

[39] E. Rossen, C. D. W. Jones, and J. R. Dahn. Structure and electrochemistry of $Li_xMn_yNi_{1-y}O_2$. *Solid State Ionics*, 57:311, 1992.

[40] Y. Makimura and T. Ohzuku. Lithium insertion material of $LiNi_{1/2}Mn_{1/2}O_2$ for advanced lithium-ion batteries. *J. Power Sources*, 119:156, 2003.

[41] J. Cho, J. G. Lee, B. Kim, and B. Park. Effect of P_2O_5 and $AlPO_4$ coating on $LiCoO_2$ cathode material. *Chem. Mater.*, 15:3190, 2003.

[42] J. Cho, Y. J. Kim, and B. Park. Novel $LiCoO_2$ cathode material with Al_2O_3 coating for a Li-ion cell. *Chem. Mater.*, 12(12):3788, 2000.

[43] Z. H. Chen and J. R. Dahn. Studies of $LiCoO_2$ coated with metal oxides. *Electrochem. Solid-State Lett.*, 6(11):A221, 2003.

[44] M. M. Thackeray, S.-H. Kang, C. S. Johnson, J. T. Vaughey, R. Benedek, and S. A. Hackney. Li_2MnO_3-stabilized $LiMO_2$ (M = Mn, Ni, Co) electrodes for lithium-ion batteries. *J. Mater. Chem.*, 17:3112, 2007.

[45] M. M. Thackeray, W. I. F. David, P. G. Bruce, and J. B. Goodenough. Lithium insertion into manganese spinels. *Mater. Res. Bull.*, 18:461, 1983.

[46] J. M. Tarascon, E. Wang, F. K. Shokoohi, W. R. McKinnon, and S. Colson. The spinel phase of $LiMn_2O_4$ as a cathode in secondary lithium cells. *J. Electrochem. Soc.*, 138:2859, 1991.

[47] K. Amine, J. Liu, S. Kang, I. Belharouak, Y. Hyung, D. Vissers, and G. Henriksen. Improved lithium manganese oxide spinel/graphite Li-ion cells for high-power applications. *J. Power Sources*, 129(1):14, 2004.

[48] R. D. Rauh, K. M. Abraham, G. F. Pearson, J. K. Surprenant, and S. B. Brummer. A lithium/dissolved sulfur battery with an organic electrolyte. *J. Electrochem. Soc.*, 126:523, 1979.

[49] H. Yamin and E. Peled. Electrochemistry of a nonaqueous lithium/sulfur cell. *J. Power Sources*, 9:281, 1983.

[50] W. Zheng, Y. W. Liu, X. G. Hu, and C. F. Zhang. Novel nanosized adsorbing sulfur composite cathode materials for the advanced secondary lithium batteries. *Electrochim. Acta*, 51:1330, 2006.

[51] J. Z. Wang, L. Lu, M. Choucair, J. A. Stride, X. Xu, and H. K. Liu. Sulfur-graphene composite for rechargeable lithium batteries. *J. Power Sources*, page 7030, 2011.

[52] K. M. Abraham and Z. Jiang. A polymer electrolyte-based rechargeable lithium/oxygen battery. *J. Electrochem. Soc.*, 143:1, 1996.

[53] T. Ogasawara, A. Debart, M. Holzapfel, P. Novak, and P. G. Bruce. Rechargeable Li_2O_2 electrode for lithium batteries. *J. Am. Chem. Soc.*, 128:1390, 2006.

[54] J. Cabana, L. Monconduit, D. Larcher, and M. R. Palacin. Beyond intercalation-based Li-ion batteries: The state of the art and challenges of electrode materials reacting through conversion reactions. *Adv. Mater.*, 22:E170, 2010.

[55] H. Arai, S. Okada, Y. Sakurai, and J. Yamaki. Cathode performance and voltage estimation of metal trihalides. *J. Power Sources*, 68:716, 1997.

[56] F. Badway, N. Pereira, F. Cosandey, and G. G. Amatucci. Carbon metal fluoride nanocomposites. *J. Electrochem. Soc.*, 150:A1209, 2003.

[57] F. Badway, F. Cosandey, N. Pereira, and G. G. Amatucci. Carbon metal fluoride nanocomposites. *J. Electrochem. Soc.*, 150:A1318, 2003.

[58] N. Yamakawa, M. Jiang, B. Key, and C. P. Grey. Identifying the local structures formed during lithiation of the conversion material, iron fluoride, in a li-ion battery: A solid-state NMR, X-ray diffraction, and pair distribution function analysis study. *Chem. Mater.*, 21:3162, 2009.

[59] M. Seto, Y. Yoda, S. Kikuta, X. W. Zhang, and M Ando. Observation of nuclear resonant scattering accompanied by phonon excitation using synchrotron radiation. *Phys. Rev. Lett.*, 74:3828, 1995.

[60] W. Strurhahn, T. S. Toellner, E. E. Alp, X. Zhang, M. Ando, Y. Yoda, S. Kikuta, M. Seto, C. W. Kimball, and B. Dabrowski. Phonon density-of-states measured by inelastic nuclear resonant scattering. *Phys. Rev. Lett.*, 74:3832, 1995.

[61] B. Fultz, C. C. Ahn, E. E. Alp, W. Strurhahn, and T. S. Toellner. Phonons in nanocrystalline ^{57}Fe. *Phys. Rev. Lett.*, 79:937, 1997.

[62] N. N. Greenwood and T. C. Gibb. *Mössbauer spectroscopy.* Chapman & Hall, London, 1971.

[63] P Gütlich. *Mössbauer spectroscopy in chemistry*, chapter 2. Springer-Verlag, New York, 1975.

[64] J. A. Tjon and M. Blume. Mössbauer spectra in a fluctuating environment; randomly varing electric field gradients. *Phys. Rev.*, 165(2):456, 1968.

[65] G. Amthauer and G. R. Rossman. Mixed-valence of iron in minerals with cation clusters. *Phys. Chem. Miner.*, 11(1):37, 1984.

[66] S. Margulies and J. R. Ehrman. Transmission and line broadening of resonance radiation incident on a resonance absorber. *Nucl. Instr. and Meth.*, 12:131, 1961.

[67] D. A. Shirley, M. Kaplan, and P. Axel. Recoil-free resonant absorption in Au^{197}. *Phys. Rev.*, 123(3):816, 1961.

[68] U. Shimony. Condition for maximum single-line Mössbauer absorption. *Nucl. Instr. and Meth.*, 37:348, 1965.

[69] P. R. Sarma, V. Prakash, and K. C. Tripathi. Optimization of the absorber thickness for improving the quality of a Mössbauer spectrum. *Nucl. Instr. and Meth.*, 178:167, 1980.

[70] A. K. Padhi, K. S. Nanjundaswamy, and J. B. Goodenough. Phospho-olivines as positive-electrode materials for rechargeable lithium batteries. *J. Electrochem. Soc.*, 144(4):1188, 1997.

[71] A. S. Andersson, B. Kalska, L. Haggstrom, and J. O. Thomas. Lithium extraction/insertion in $LiFePO_4$: an X-ray diffraction and Mössbauer spectroscopy study. *Solid State Ionics*, 130(1-2):41, 2000.

[72] C. Delacourt, P. Poizot, J-M. Tarascon, and C. Masquelier. The existence of a temperature-driven solid solution in Li_xFePO_4 for $0 \leq x \leq 1$. *Nat. Mater.*, 4(3):254, 2005.

[73] A. Yamada, H. Koizumi, S. I. Nishimura, N. Sonoyama, R. Kanno, M. Yonemura, T. Nakamura, and Y. Kobayashi. Room-temperature miscibility gap in Li_xFePO_4. *Nat. Mater.*, 5(5):357, 2006.

[74] F. Zhou, T. Maxisch, and G. Ceder. Configurational electronic entropy and the phase diagram of mixed-valence oxides: The case of Li_xFePO_4. *Phy. Rev. Lett.*, 97(15):155704, 2006.

[75] A. Yamada, H. Koizumi, N. Sonoyama, and R. Kanno. Phase change in Li_xFePO_4. *Electrochem. Solid-State Lett.*, 8:A409, 2005.

[76] P. Gibot, M. Casas-Cabanas, L. Laffont, S. Levasseur, P. Carlach, S. Hamelet, J-M. Tarascon, and C. Masquelier. Room-temperature single-phase Li insertion/extraction in nanoscale Li_xFePO_4. *Nat. Mater.*, 7, 2008.

[77] B. Kang and G. Ceder. Battery materials for ultrafast charging and discharging. *Nature*, 458(7235):190, 2009.

[78] N. Meethong, H. Y. S. Huang, W. C. Carter, and Y. M. Chiang. Size-dependent lithium miscibility gap in nanoscale $Li_{1-x}FePO_4$. *Electrochem. Solid-State Lett.*, 10(5):A134, 2007.

[79] N. Meethong, Y-H. Kao, M. Tang, H-Y. Huang, W. C. Carter, and Y-M. Chiang. Electrochemically induced phase transformation in nanoscale olivines Li_xMPO_4 (M = Fe, Mn). *Chem. Mater.*, 20(19):6189, 2008.

[80] G. Kobayashi, S. Nishimura, M. Park, R. Kanno, M. Yashima, T. Ida, and A. Yamada. Isolation of solid solution phases in size-controlled Li_xFePO_4 at room temperature. *Adv. Funct. Mater.*, 19:395, 2009.

[81] H. J. Tan, J. L. Dodd, and B. Fultz. Thermodynamic and kinetic stability of the solid solution phase in nanocrystalline Li_xFePO_4. *J. Phys. Chem. C*, 113(48):20527, 2009.

[82] K. Zaghib, P. Charest, M. Dontigny, A. Guerfi, M. Lagace, A. Mauger, M. Kopec, and C. M. Julien. $LiFePO_4$: From molten ingot to nanoparticles with high-rate performance in Li-ion batteries. *J. Power Sources*, 195:8280, 2010.

[83] V. Srinivasan and J. Newman. Discharge model for the lithium iron-phosphate electrode. *J. Electrochem. Soc.*, 151(10):A1517, 2004.

[84] D. Morgan, A. Van der Ven, and G. Ceder. Li conductivity in Li_xMPO_4 (M = Mn, Fe, Co, Ni) olivine materials. *Electrochem. Solid-State Lett.*, 7(2):A30, 2004.

[85] S. Nishimura, G. Kobayashi, K. Ohoyama, R. Kanno, M. Yashima, and A. Yamada. Experimental visualization of lithium diffusion in Li_xFePO_4. *Nat. Mater.*, 7:707, 2008.

[86] G. Y. Chen, X. Y. Song, and T. J. Richardson. Electron microscopy study of the $LiFePO_4$ to $FePO_4$ phase transition. *Electrochem. Solid-State Lett.*, 9(6):A295, 2006.

[87] C. Delmas, M. Maccario, L. Croguennec, F. Le Cras, and F. Weill. Lithium deintercalation in $LiFePO_4$ nanoparticles via a domino-cascade model. *Nat. Mater.*, 7(8):665, 2008.

[88] J. Y. Li, W. L. Yao, S. Martin, and D. Vaknin. Lithium ion conductivity in single crystal $LiFePO_4$. *Solid State Ionics*, 179(35–36):2016, 2008.

[89] R. Amin and J. Maier. Effect of annealing on transport properties of $LiFePO_4$: Towards a defect chemical model. *Solid State Ionics*, 178(35–36):1831, 2008.

[90] B. Ellis, L. K. Perry, D. H. Ryan, and L. F. Nazar. Small polaron hopping in Li_xFePO_4 solid solutions: Coupled lithium-ion and electron mobility. *J. Am. Chem. Soc.*, 128(35):11416, 2006.

[91] T. Maxisch, F. Zhou, and G. Ceder. Ab initio study of the migration of small polarons in olivine Li_xFePO_4 and their association with lithium ions and vacancies. *Phys. Rev. B*, 73(10):104301, 2006.

[92] R. Malik, F. Zhou, and G. Ceder. Kinetics of non-equilibrium lithium incorporation in $LiFePO_4$. *Nat. Mater.*, 10:587, 2011.

[93] A. Yamada, S. C. Chung, and K. Hinokuma. Optimized $LiFePO_4$ for lithium battery cathodes. *J. Electrochem. Soc.*, 148(3):A224, 2001.

[94] P. P. Prosini, M. Lisi, D. Zane, and M. Pasquali. Determination of the chemical diffusion coefficient of lithium in $LiFePO_4$. *Solid State Ionics*, 148:45, 2002.

[95] M. Takahashi, S. Tobishima, K. Takei, and Y. Sakurai. Characterization of $LiFePO_4$ as the cathode material for rechargeable lithium batteries. *J. Power Sources*, 97:508, 2001.

[96] H. S. Kim, B. W. Cho, and W. I. Cho. Cycling performance of $LiFePO_4$ cathode material for lithium secondary batteries. *J. Power Sources*, 132:235, 2004.

[97] C. H. Mi, X. B. Zhao, G. S. Cao, and J. P. Tu. In situ synthesis and properties of carbon-coated $LiFePO_4$ as Li-ion battery cathodes. *J. Electrochem. Soc.*, 152:A483, 2005.

[98] G. Arnold, J. Garche, R. Hemmer, S. Strobele, C. Vogler, and M. Wohlfahrt-Mehrens. Fine-particle lithium iron phosphate $LiFePO_4$ synthesized by a new low-cost aqueous precipitation technique. *J. Power Sources*, 119:247, 2003.

[99] C. Delacourt, P. Poizot, S. Levasseur, and C. Masquelier. Size effects on carbon-free $LiFePO_4$ powders. *Electrochem. and Solid-State Lett.*, 9(7):A352, 2006.

[100] H. T. Chung, S. K. Jang, H. W. Ryu, and K. B. Shim. Effects of nano-carbon webs on the electrochemical properties in $LiFePO_4$/C composite. *Solid State Commun.*, 131:549, 2004.

[101] S. Singhal, G. Skandan, G. Amatucci, F. Badway, N. Ye, A. Manthiram, H. Ye, and J. J. Xu. Nanostructured electrodes for next generation rechargeable electrochemical devices. *J. Power Sources*, 129:38, 2004.

[102] A. D. Spong, G. Vitins, and J. R. Owen. A solution-precursor synthesis of carbon-coated $LiFePO_4$ for Li-ion cells. *J. Electrochem. Soc.*, 152:A2376, 2005.

[103] M. R. Yang, W. H. Ke, and S. H. Wu. Preparation of $LiFePO_4$ powders by co-precipitation. *J. Power Sources*, 146:539, 2005.

[104] H. P. Klug and L. E. Alexander. *X-ray diffraction procedures for polycrystalline and amorphous materials.* Wiley, 1974.

[105] H. Huang, S. C. Yin, and L. F. Nazar. Approaching theoretical capacity of $LiFePO_4$ at room temperature at high rates. *Electrochem. Solid-State Lett.*, 4(10):A170, 2001.

[106] N. Ravet, Y. Chouinard, J. F. Magnan, S. Besner, M. Gauthier, and M. Armand. Electroactivity of natural and synthetic triphylite. *J. Power Sources*, 97:503, 2001.

[107] K. Zaghib, K. Striebel, A. Guerfi, J. Shim, M. Armand, and M. Gauthier. $LiFePO_4$/polymer/natural graphite: low cost Li-ion batteries. *Electrochim. Acta*, 50(2–3):263, 2004.

[108] K. F. Hsu, S. Y. Tsay, and B. J. Hwang. Synthesis and characterization of nano-sized $LiFePO_4$ cathode materials prepared by a citric acid-based sol-gel route. *J. Mater. Chem.*, 14:2690, 2004.

[109] J. Barker, M. Y. Saidi, and J. L. Swoyer. Lithium iron(II) phospho-olivines prepared by a novel carbothermal reduction method. *Electrochem. Solid-State Lett.*, 6:A53, 2003.

[110] R. Dominko, M. Gaberscek, J. Drofenik, M. Bele, S. Pejovnik, and J. Jamnik. The role of carbon black distribution in cathodes for Li ion batteries. *J. Power Sources*, 119:770, 2003.

[111] H. Gabrisch, J. D. Wilcox, and M. M. Doeff. Carbon surface layers on a high-rate $LiFePO_4$. *Electrochem. Solid-State Lett.*, 9:A360, 2006.

[112] J.D. Wilcox, M.M. Doeff, M. Marcinek, and R. Kostecki. Factors influencing the quality of carbon coatings on $LiFePO_4$. *J. Electrochem. Soc.*, 154:A389, 2007.

[113] P. S. Herle, B. Ellis, N. Coombs, and L. F. Nazar. Nano-network electronic conduction in iron and nickel olivine phosphates. *Nat. Mater.*, 3(3):147, 2004.

[114] L. Kavan, I. Exnar, J. Cech, and M. Graetzel. Enhancement of electrochemical activity of $LiFePO_4$ (olivine) by amphiphilic Ru-Bipyridine complex anchored to a carbon nanotube. *Chem. Mater.*, 19:4716, 2007.

[115] S. Y. Chung, J. T. Bloking, and Y. M. Chiang. Electronically conductive phospho-olivines as lithium storage electrodes. *Nat. Mater.*, 1:123, 2002.

[116] C. Delacourt, L. Laffont, L. Bouchet, C. Wurm, J. B. Leriche, J. M. Tarascon, and C. Masquelier. Toward understanding of electrical limitations (electronic, ionic) in $LiMPO_4$ (M=Fe, Mn) electrode material. *J. Electrochem. Soc.*, 152:A913, 2005.

[117] M. Takahashi, S. Tobishima, K. Takei, and Y. Sakurai. Reaction behavior of $LiFePO_4$ as a cathode material for rechargeable lithium batteries. *Solid State Ionics*, 148:283, 2002.

[118] S. Q. Shi, L. J. Liu, C. Y. Ouyang, D. S. Wang, Z. X. Wang, L. Q. Chen, and X. J. Huang. Enhancement of electronic conductivity of $LiFePO_4$ by Cr doping and its identification by first-principles calculations. *Phys. Rev. B*, 68:195108, 2003.

[119] Y. N. Xu, S. Y. Chung, J. T. Bloking, Y. M. Chiang, and W. Y. Ching. Electronic structure and electrical conductivity of undoped $LiFePO_4$. *Electrochem. Solid-State Lett.*, 7(6):A131, 2004.

[120] K. T. Fehr, R. Hochleitner, E. Schmidbauer, and J. Schneider. Mineralogy, Mössbauer spectra and electrical conductivity of triphylite $Li(Fe^{2+}, Mn^{2+})PO_4$. *Phys. Chem. Miner.*, 34(7):485, 2007.

[121] K. Zaghib, A. Mauger, J. B. Goodenough, F. Gendron, and C. M. Julien. Electronic, optical, and magnetic properties of $LiFePO_4$: Small magnetic polaron effects. *Chem. Mater.*, 19:3740, 2007.

[122] R. Stevens, J. L. Dodd, M. G. Kresch, R. Yazami, B. Fultz, B. Ellis, and L. F. Nazar. Phonons and thermodynamics of unmixed and disordered $Li_{0.6}FePO_4$. *J. Phys. Chem. B*, 110(45):22732, 2006.

[123] Y. H. Rho, L. F. Nazar, L. Perry, and D. Ryan. Surface chemistry of $LiFePO_4$ studied by Mössbauer and X-ray photoelectron spectroscopy and its effect on electrochemical properties. *J. Electrochem. Soc.*, 154(4):A283, 2007.

[124] L. Wang, F. Zhou, Y. S. Meng, and G. Ceder. First-principles study of surface properties of $LiFePO_4$: Surface energy, structure, Wulff shape, and surface redox potential. *Phys. Rev. B*, 76:165435, 2007.

[125] C. A. J. Fisher and M. S. Islam. Surface structures and crystal morphologies of $LiFePO_4$: Relevace to electrochemical behaviour. *J. Mater. Chem.*, 18:1209, 2008.

[126] A. Ait-Salah, J. Dodd, A. Mauger, R. Yazami, F. Gendron, and C. M. Julien. Structual and magnetic properties of $LiFePO_4$ and lithium extraction effects. *Z. Anorg. Allg. Chem.*, 632:1598, 2006.

[127] G. Rousse, S. Rodriguez-Carvajal, C. Patoux, and C. Masquelier. Structural and magnetic properties of $LiFePO_4$ and lithium extraction effects. *Chem. Mater.*, 15:4082, 2003.

[128] C. Achim, E. L. Bominaar, J. Meyer, J. Peterson, and E. Munck. Observation and interpretation of temperature-dependent valence delocalization in the [2Fe-2S](+) cluster of a ferredoxin from clostridium pasteurianum. *J. Am. Chem. Soc.*, 121(15):3704, 1999.

[129] C. Achim, E. L. Bominaar, R. J. Staples, E. Munck, and R. H. Holm. Influence of extrinsic factors on electron transfer in a mixed-valence Fe^{2+}/Fe^{3+} complex: Experimental results and theoretical considerations. *Inorg. Chem.*, 40(17):4389, 2001.

[130] H. Hannoyer, A. A. M. Prince, M. Jean, R. S. Liu, and G. X. Wang. Mössbauer study on $LiFePO_4$ cathode material for lithium ion batteries. *Hyperfine Interact.*, 167:767, 2006.

[131] C. M. Burba and R. Frech. Raman and FTIR spectroscopic study of Li_xFePO_4 ($0< x <1$). *J. Electrochem. Soc.*, 151(7):A1032, 2004.

[132] M. M. Doeff, Y. Q. Hu, F. Mclarnon, and R. Kostecki. Effect of surface carbon structure on the electrochemical performance of $LiFePO_4$. *Electrochem. Solid-State Lett.*, 6:A207, 2003.

[133] R. Dominko, M. Bele, M. Gaberscek, M. Remskar, D. Hanzel, S. Pejovnik, and J. Jamnik. Impact of the carbon coating thickness on the electrochemical performance of $LiFePO_4$/C composites. *J. Electrochem. Soc.*, 152(3):A607, 2005.

[134] K. Zaghib, A. Mauger, M. Kopec, F. Gendron, and C. M. Julien. Intrinsic properties of 40 nm-sized $LiFePO_4$ particles. *ECS Transactions*, 16(42):31, 2009.

[135] J. L. Jones, J. T. Hung, and Y. S. Meng. Intermittent X-ray diffraction study of kinetics of delithiation in nano-scale $LiFePO_4$. *J. Power Sources*, 189(1):702, 2009.

[136] M. Konarova and I. Taniguchi. Synthesis of carbon-coated $LiFePO_4$ nanoparticles with high rate performance in lithium secondary batteries. *J. Power Sources*, 195(11):3661, 2010.

[137] R. Malik, D. Burch, M. Bazant, and G. Ceder. Particle size dependence of the ionic diffusivity. *Nano Lett.*, 10:4123, 2010.

[138] B. Ellis, P. S. Herle, Y. H. Rho, L. F. Nazar, R. Dunlap, L. K. Perry, and D. H. Ryan. Nanostructured materials for lithium-ion batteries: Surface conductivity vs. bulk ion/electron transport. *Faraday Discuss.*, 134:119, 2007.

[139] M. Tang, H. Y. Huang, N. Meethong, Y. H. Kao, W. C. Carter, and Y-M. Chiang. Model for the particle size, overpotential, and strain dependence of phase transition pathways in storage electrodes: Application to nanoscale olivines. *Chem. Mater.*, 21(8):1557, 2009.

[140] D. Burch and M. Z. Bazant. Size-dependent spinodal and miscibility gaps for intercalation in nanoparticles. *Nano Lett.*, 9(11):3795, 2009.

[141] N. F. Mott. Conduction in glasses containing transition metal ions. *J. Non-Cryst. Solids*, 1:1, 1968.

[142] Y. Xu, T. J. Shankland, and A. G. Duba. *Phys. Earth Planetary Interiors*, 118:149, 2000.

[143] R. Ingalls. Electric-field gradient tensor in ferrous compounds. *Phys. Rev.*, 133(3A):A787, 1964.

[144] M. Danot, M. I. Afanasov, P. B. Fabritchnyi, A. S. Golub, N. D. Lenenko, Y. N. Novikov, K. V. Pokholok, and I. A. Presniakov. Mössbauer evidence for fast electron hopping between Fe(II) and Fe(III) in iron hydroxide/molybdenum disulfide lamellar nanocomposite. *Solid State Ionics*, 128:211, 2000.

[145] M. Wagemaker, F. M. Mulder, and A. Van der Ven. The role of surface and interface energy on phase stability of nanosized insertion compounds. *Adv. Mater.*, 21:2703, 2009.

[146] K. Zaghib, A. Mauger, F. Gendron, and C. M. Julien. Surface effects on the physical and electrochemical properties of thin $LiFePO_4$ particles. *Chem. Mater.*, 20:462, 2008.

[147] K. T. Lee, W. H. Kan, and L. F. Nazar. Proof of intercrystallite ionic transport in $LiMPO_4$ electrodes (M = Fe, Mn). *J. Am. Chem. Soc.*, 131(17):6044, 2009.

[148] A. Van der Ven, K. Garikipati, S. Kim, and M. Wagemaker. The role of coherency strains on phase stability in Li_xFePO_4: Needle crystallites minimize coherency strain and overpotential. *J. Electrochem. Soc.*, 156(11):A949, 2009.

[149] Y. Reynier, J. Graetz, T. Swan-Wood, P. Rez, R. Yazami, and B. Fultz. Entropy of Li intercalation in Li_xCoO_2. *Phys. Rev. B*, 70(17):174304, 2004.

[150] Y. Reynier, R. Yazami, B. Fultz, and I. Barsukov. Evolution of lithiation thermodynamics with the graphitization of carbons. *J. Power Sources*, 165(2):552, 2007. [Joint Meeting of the International-Battery-Association/Hawaii Battery Conference (IBA-HBC 2006), Hilo, HI, Jan, 2006].

[151] H. Matsui, T. Nakamura, Y. Kobayashi, M. Tabuchi, and Y. Yamada. Open-circuit voltage study on $LiFePO_4$ olivine cathode. *J. Power Sources*, 195:6879, 2010.

[152] R. H. Goodman and J. E. Richardson. Use of "on line" computer for Mössbauer experiments. *Rev. Sci. Instrum.*, 37(3):283, 1966.

[153] B. Fultz and J. W. Morris. Multichannel scaling with an eight bit microcomputer. *Rev. Sci. Instrum.*, 49(8):1216, 1978.

[154] M. Benedetti and D. R. Fernandez. Fully programmable microprocessor-controlled Mössbauer spectrometer. *Rev. Sci. Instrum.*, 52(9):1406, 1981.

[155] A.J. Sánchez Asseff, A. Bohórquez, G.A. Pérez Alcázar, and H.-D. Pfannes. An autonomous programmable system for Mössbauer spectroscopy, accessed by a PC program. *Hyperfine Interact.*, 110:135, 1997.

[156] A. L. Morales, J. Zuluaga, A. Cely, and J. Tobón. Autonomous system design for Mössbauer spectra acquisition. *Hyperfine Interact.*, 134:167, 2001.

[157] M. Mashlan, D. Jancik, D. Zak, F. Dufka, V. Snasel, and A. L. Kholmetskii. The Mössbauer spectrometer as a virtual instrument. In *Mössbauer spectrscopy in materials science*, pages 399–406. Kluwer Academic Publishers, 1999.

[158] J. Pechousek and M. Mashlan. Mössbauer spectrometer as a virtual instrument in the PXI/Compact PCI modular system. *Czech. J. of Phys.*, 55:853, 2005.

[159] J. R. Gancedo, M. Gracia, and J. F. Marco. Practical aspects of Mössauer spectroscopy instrumentation. *Hyperfine Interact.*, 83:71, 1994.